A SPATIO-TEMPORAL MODEL FOR CANCELLOUS BONE AT THE TISSUE SCALE

by

Brianna Martin

Thesis
Submitted to Flinders University
for the degree of

Doctor of Philosophy

College of Science and Engineering

1st October 2019

All models are wrong. Some are useful.

George Box.

Abstract

A spatio-temporal partial differentiation model is presented for the change in cancellous bone volume in growing animals, in terms of key bone remodelling processes. The model parameters were found by optimising the analytic solution of the model over experimental bone volume data. Experimental data comprises microcomputed CT scans of juvenile rat tibia from three groups, including normal rats, oestrogen-deplete rats, and oestrogen-deplete rats treated with bisphosphonates. The model demonstrates that cancellous bone volume in normal growing rats does not change over time. The model also explains the changes in cancellous bone volume due to oestrogen depletion and bisphosphonate treatment. However, for bisphosphonate treated rats, the model cannot explain all of the changes in cancellous bone volume mechanistically, for bone adjacent to the growth plate. Good fits between the model and data were obtained by making simple assumptions regarding the effect of treatment, leading to conjecture regarding the role of bisphosphonates in growing animals.

Contents

List of Figures

List of Tables

Declaration

I certify that this thesis does not incorporate without acknowledgement, any material previously submitted for a degree or diploma in any university, and that to the best of my knowledge and belief it does not contain any material previously published or written by another person, except where due reference is made in the text.

Brianna Martin

Acknowledgements

This work was supported in part by the Australian Postgraduate Award.

A heartfelt thank you to my supervisors Karen and Murk for enduring support and guidance. Thank you to Tara B, for unwavering generosity, patience, and awe-inspiring tenacity and gusto. Thank you to the bone/modelling community for assisting with domain knowledge and idea-sharing, especially Richard W, Peter P, David F, Egon P, and Pascal B. Thank you to friends and family for providing perspective and unconditional love - Dad, Mike, Alanna, Sue, Andrew, Patrick, Grandpa, Deb, Serena, Phil, Hannah, Denise, Carl, Rui Rui, Joy, Mel and Simon. Most importantly, thank you to the special four-leggeds for laughter and joy - Dippy Tutu, Spencer, Marshall, Sooty, Flossy, Mojo, Jaffar, Tigga, Arthur, and I suppose, even Pantaloon.

Dedication

This thesis is dedicated to Nobel Paws Prize laureate Desmond (my dog). Also to my dad for the provision of dad meals, dad advice, dad hugs, and for donations from Bank of Dad.

Nomenclature

growth plate	physis or ephiphyseal plate
(IL-1)	interleukin 1
AAP	Antiarrhythmic peptides
anabolic	bone building
apoptosis	programmed cell death
BMPs	bone morphogenetic proteins
BMU	bone multicellular units
chondro-osseous junction	region of growth plate where cartilage material is adjacent to bone material at the vascular front
chondroclast	osteoclast that sits on the surface of cartilage and sometimes lacks a sealing zone and/or a ruffled border
chondrocyte	cartilage cell
CNP	C-type natriuretic peptide, a molecule that acts as a chondrocyte growth factor in growth plate cartilage
diaphysis	long shaft of long bones
distal	far away from the growth plate
EGF	epidermal growth factor

endocrine factors	factors in blood
epiphyseal plate	growth plate or physis
epiphysis	end of long bone
FGF	fibroblast growth factor, a molecule involved in chondrocyte proliferation
GH	growth hormone
hypertrophic	enlarged
IGF	insulin-like growth factor, a molecule involved in solid matrix synthesis in cartilage
IGF-1	type 1 insulin growth factor
Ihh	Indian hedgehog, a protein involved in chondrocyte differentiation, proliferation and maturity
matrix	cartilage or bone scaffold
medullary cavity	bone marrow cavity
metaphysis	region of bone between epiphysis and diaphysis
mitosis	acellular reproduction
NPPC	C-type natriuretic peptide, a molecule that acts as a chondrocyte growth factor in growth plate cartilage
OI	osteogenesis imperfecta
OPG	osteoprotegerin
osseous material	bone material
osteoblast	bone forming cell
osteoclast	cell that degrades cartilage and bone

osteoclastogenic cells	osteoclast precursor cells
osteocyte	mechanosensory/regulatory bone cell
osteogenic cells	osteoblast precursor cells
physis	growth plate
primary ossification	prenatal ossification
primary spongiosa	region of metaphysis proximal to growth plate
proteoglycan	connective tissue protein
proximal	closer to the torso
PTH	parathyroid hormone, a hormone secreted by the parathyroid gland in response to low blood serum calcium levels and binds to parathyroid hormone 1 receptor (PTH1R)
PTH1R	Type 1 parathyroid hormone receptor, a receptor that binds to both parathyroid hormone (PTH) and parathyroid hormone like protein (PTHrP)
PTHrP	parathyroid hormone like protein
RANK	receptor for RANKL
RANKL	receptor activator for nuclear factor ligand
secondary ossification	postnatal lengthening of long bones
secondary spongiosa	region of metaphysis distal to growth plate
SOCS	suppressor of cytokine signalling 2, a family of proteins that down regulate growth hormone (GH) and insulin-like growth factor-1 (IFG-1)

Subchondral bone	bone in early stages of ossification that still contains more cartilage and mineralised cartilage material than bone material
TGF-β	transforming growth factor
transdifferentiate	change from one cell type to another
VEGF	vascular endothelial growth factor, a molecule involved in chondrocyte proliferation
Wnt	wingless/integrated proteins, a family of singalling proteins involved in endochondral ossification and bone remodelling

Chapter 1

Introduction

To date, little is known about how bone remodelling is affected in growing animals. Of particular interest is the modification of remodelling processes under osteoporotic conditions and after treatments have been administered. The general aim of this project is to develop and explore mathematical models that describe bone remodelling processes in cancellous bone in growing animals. Mathematical strategies are combined with the use of longitudinal experimental data. The experimental data includes microcomputed CT (μCT) scans of cancellous bone in the tibia of juvenile rats from three groups, including normal bone, oestrogen-deplete bone and oestrogen-deplete bone treated with bisphosphonates. The outcome is a model that explains the observed changes to bone volume fraction (BV/TV) over time for the experimental data. First a biological background is given to describe: long bone structure, bone growth, bone remodelling, and current treatment strategies for osteoporotic bone. This chapter concludes with an overview of the work carried out in this study.

1.1 Bone biology

Mammalian bone is a dynamic tissue that continues to change over time both in terms of volume and structure during growth, adulthood and old age (Seeman, 2008). Bone consists of cells embedded in a solid scaffolding, called a matrix that is made up of both

organic materials and inorganic material. The inorganic matrix scaffold components make up the majority of the solid matrix, and are largely composed of the mineral calcium phosphate in the form of hydroxyl apatite crystals (calcium hydroxyapatite), and also contains a small amount of other salts that include potassium, magnesium, and sodium carbonate. The organic matrix scaffold components include mostly collagen but also proteoglycans and non-collagen proteins. The overall quality of bone is associated with bone mass, structure and internal architecture, and the ability to provide both structural strength for loading in addition to lightness for mobility (Seeman & Delmas, 2006; Seeman, 2008; Szule & Seeman, 2009).

1.1.1 Long bone structure

Long bones including the tibia and femur have a compact cortical bone outer layer, and have an internal medullary cavity (marrow cavity) that contains bone marrow which produces blood cells. A long bones consists of a main shaft called the diaphysis with an epiphysis at both ends, and metaphyseal bone between the epiphysis and diaphysis (Figure 1.1). The epiphysis is the region of bone that forms a joint which contains red bone marrow and produces red blood cells, and is covered in rubbery wear-resistant articular (hyleine) cartilage. Between the epiphysis and the metaphysis is the physis. The physis is also referred to as the ephiphyseal plate or the growth plate.The metaphysis consists of porous, spongy, cancellous bone that has trabecular architecture (Komarova, 2006). The region of the metaphysis closest to the torso of the body is termed proximal and the region furthest away is termed distal. Trabecular bone provides lightness and flexibility without greatly compromising structural strength (Fyhrie *et al.* , 1993, 1995). The density of the metaphyseal trabeculae is higher close to the growth plate and lessens further away from the growth plate.

Prenatally, long bone growth begins in the primary ossification centre located in the diaphysis. Postnatally and during adolescence, long bones elongate via endochondral ossification at the growth plate in the secondary ossification centre, at the epiphyseal ends. Endochondral ossification is the process whereby the synthesised mineralised hy-

aline cartilage at the growth plate acts as a scaffold and is replaced by osseous (bone) material. The growth plate is avascular cartilaginous material that is synthesised by chondrocytes. Chondrocytes are the only living cells in cartilage. The cartilage is made up of a synthesised solid matrix scaffold that surrounds the chondrocyte cells, which is predominantly made up of of collagen, proteoglycans and other proteins (Hunziker *et al.* , 2007). The rest of the space in the growth plate surrounding the solid matrix scaffold is occupied by interstitial fluid made up of water and soluble nutrients like glucose. The chondro-osseous junction is where the growth plate meets the metaphysis . A vascular front on the metaphyseal side brings bone cells to the growth plate to break down the calcified matrix scaffolding for bone replacement (Figure 1.2). The growth plate also has blood supply on the epiphyseal end. Within the growth plate, nutrient and endocrine molecules that play a role in endochondral ossification travel by diffusion. Additional molecules are produced locally by chondrocytes.

Next to the chondro-osseous junction is a layer of subchondral (beneath cartilage) bone in the metaphysis called the primary spongiosa. Subchondral bone is in the early stages of ossification and consists mostly of a calcified cartilaginous matrix scaffold with some deposited bone (Erben *et al.* , 1990). The subchondral bone next to the growth plate is sometimes referred to as the ossification zone. Further away from the growth plate in the methaphysis is the secondary spongiosa, where the calcified/mineralised cartilage matrix scaffold has been almost completely degraded and remodelled into cancellous bone (Kimmel & Jee, 1980). The density of trabecular bone in the metaphysis decreases as a function of distance from the growth plate (Gabet *et al.* , 2008). After cessation of growth in most mature mammals, the growth plate disappears. In rats however, the presence of the growth plate persists long after growth attenuates and possibly for the lifespan of the rat (Roach *et al.* , 2003).

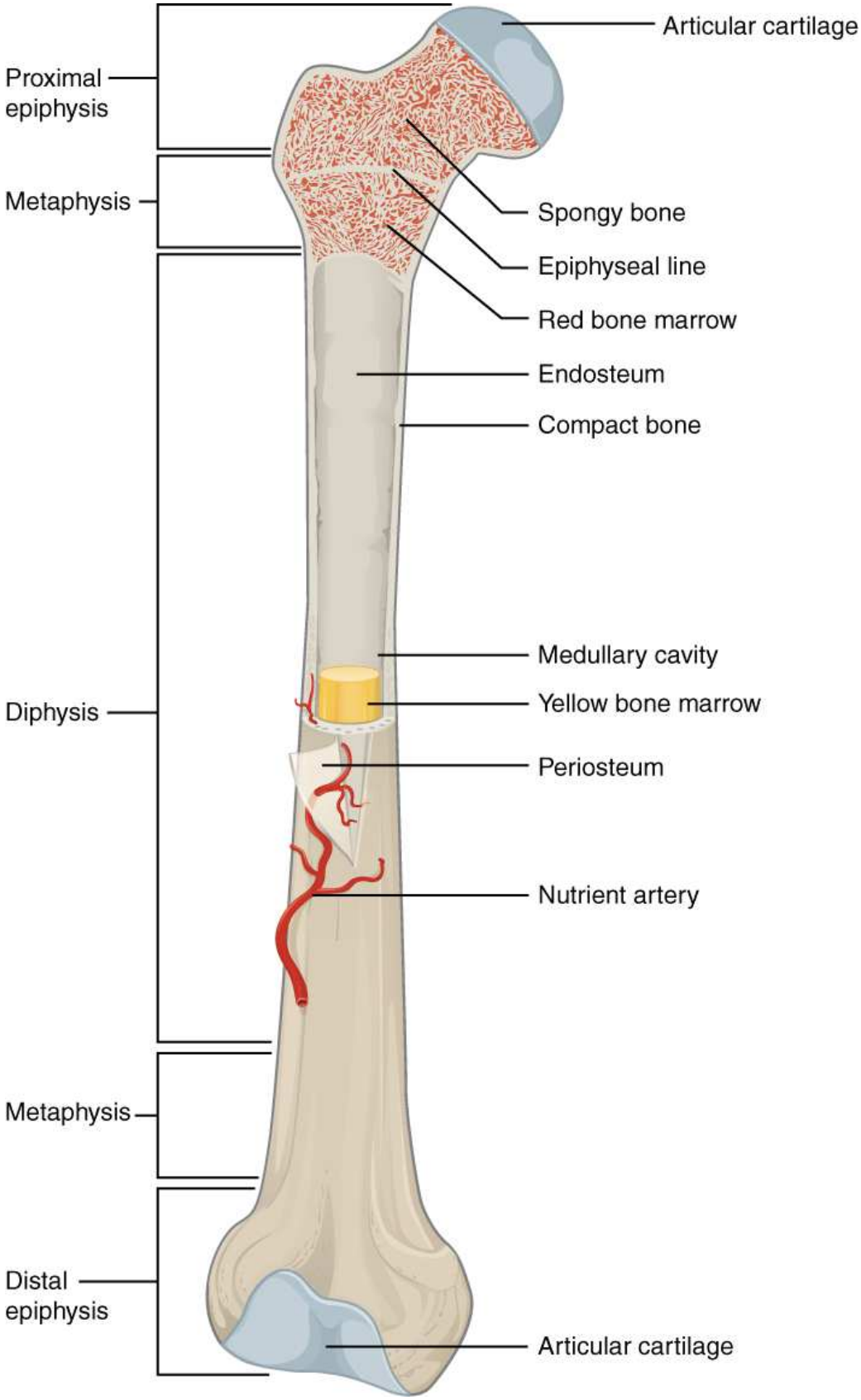

Figure 1.1: Long bone structure (with permission from Open Stax College)

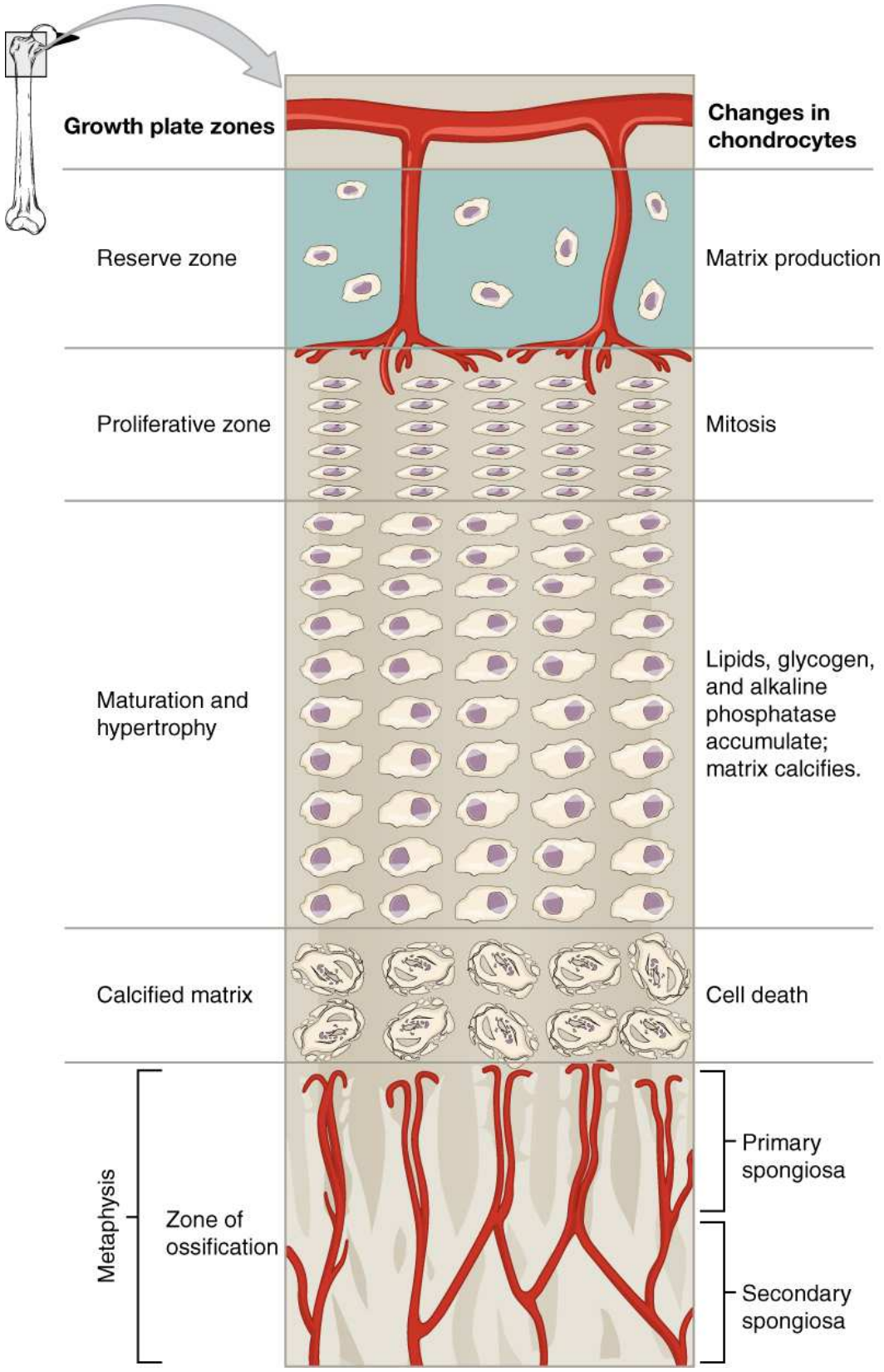

Figure 1.2: Chondro-osseous junction: the location where the growth plate meets the metaphyseal vascular front (with permission from Anatomy & Physiology, Open Oregon State)

1.1.2 Endochondral ossification

Growth of long bones via endochondral ossification occurs at different rates in different bones, at different epiphyseal ends of bones and even within the same epiphyseal plate over time (Wilsman *et al.* , 1996). Growth usually occurs in spurts. The peak skeletal dimensions in humans are reached around age thirty. This system is still not fully understood and much work has been done towards understanding the endochondral ossification processes in healthy, diseased, malnourished and injured organisms.

Chondrocytes in the growth plate cartilage are structured in zones (Lui *et al.* , 2014). Processes that occur within this system are influenced by factors that are produced in the growth plate locally and factors that are delivered by way of the endocrine (blood) system, all of which are affected by both mechanical strain/stress and biochemical agents. Mechanical influences have been tested experimentally using mechanical forces (Stokes *et al.* , 2006), and mathematically with models that include strain/stress parameters (Stokes *et al.* , 2006; Stevens & Beaupré, 1999; Henderson & Carter, 2002; Stevens *et al.* , 1999; Narváez-Tovar & garzon Alvarado, 2012). Various undesirable growth outcomes may eventuate, resulting from not enough mechanical strain or too much mechanical strain, or cyclical combinations thereof. The extensive experimental work carried out in vitro and in vivo to elucidate aspects of the system influenced by biochemical factors has been greatly aided by mathematical modelling (Garzón-Alvarado *et al.* , 2009; Brouwers *et al.* , n.d.). Some mathematical models include both mechanical and biochemical factors (Garzón-Alvarado *et al.* , 2011).

1.1.2.1 Growth plate dynamics

As long bones elongate during endochondral ossification at both epiphyseal ends, the new bone formed at the growth plate travels in a diaphyseal direction 'away' from the growth plate. The rates at which the newly formed bone travels, corresponds to the growth rate of the bone and to the overall growth rate of the organism's skeleton (Kimmel & Jee, 1980).

The growth plate is organised in three regions termed 'zones' (Figure 1.2) according to the three types of chondrocyte cells that are embedded in the solid cartilage matrix scaffold (Lui *et al.* , 2014; Xian, 2014). Though the width of the growth plate and the time scale of growth plate evolution vary, the sequence of the chondrocyte life cycle is the same across all long bone growth plates (Wilsman *et al.* , 1996).

The *resting zone* is the layer of chondrocytes at the epiphyseal end, and is connected to the epiphyseal blood supply. The chondrocytes located here serve as inactive progenitor cells and have daughter cell cloning potential to proliferate via mitosis. The major component of the extracellular cartilage matrix scaffold at this layer is Collagen II.

The *proliferative zone* is characterised by rapid proliferation of the resting zone daughter chondrocyte cells. Growth factors are delivered by the ephiphyseal red blood supply to stimulate proliferation of the resting zone germinal chondrocyte cells that are furthest away from the ephiphysis, along a column in the orientation of the medial axis, as required by the system. The rate of proliferation is thought to play a major role in the rate of overall bone output and thus growth. Collagen II remains the major constituent of the solid cartilage matrix scaffold in this zone where solid matrix scaffold surrounds individual chondrocyte cells and also forms betweens columns of proliferative chondrocyte cells.

As the chondrocyte clones continue to proliferate along the column, the chondrocytes furthest from the epiphysis cease proliferation, undergo termination differentiation and become hypertrophic (enlarged) to form a layer known as the *hypertrophic zone*. This is the final layer of the growth plate, which is adjacent to the vascular front in the metaphysis, and represents the 'chondro' in chondro-osseous junction. The solid matrix cartilage scaffold that the hypertrophic chondrocytes are embedded in is mostly made up of Collagen X rather than Collagen II. Hypertrophic chondrocytes release matrix scaffold vesicles that facilitate calcification and some of the chondrocytes die during calcification (Wilsman *et al.* , 1996). The cartilage material that emerges from the hypertrophic zone includes unmineralised cartilage and mineralised matrix scaffold. At the vascular front on the metaphyseal side of the chondro-osseous junction, endocrinal molecules and clastic bone cells (osteoclasts and chondroclasts) are delivered for degradation of all of the unmineralised cartilage in addition to degradation of more than half of the mineralised

matrix scaffold. The remaining mineralised cartilage matrix scaffold provides a template for formation of trabeculae performed by bone-forming (osteoblast) cells in the primary spongiosa at the chondro-osseous edge of the metaphysis.

There is still ongoing debate regarding the fate of the hypertrophic chondrocytes beyond the hypertrophic zone. Previously these cells were thought to all undergo apoptosis. Evidence continues to emerge that indicates a range of post-hypertrophic chondrocyte life cycle stages. Seemingly, some hypertrophic chondrocytes undergo apoptosis, some survive to transdifferentiate into osteoblast cells (Roach *et al.* , 2003), and some of the transdifferentiated osteoblast cells may either undergo apoptosis or become embedded in the primary spongiosal trabecular bone matrix scaffold and become (mechanosensing) osteocyte bone cells (Tsang *et al.* , 2015; Buenzli, 2015). Chondrocytes do not become hypertrophic in any other cartilaginous region of the body, except in osteoarthritic articular cartilage.

1.1.2.2 Local growth plate regulation

Many molecules are involved in the regulation of the evolution of the growth plate dynamics for the movement of chondrocytes through the resting, proliferative and hypertrophic zones, and solid matrix scaffold synthesis. The local regulatory system that has been most studied and which is considered to be the most important system for both prenatal and postnatal growth plate stability, is the feedback loop generated by a pair of substances called parathyroid hormone like protein (PTHrP) and Indian hedgehog (Ihh). Together, these substances control chondrocyte proliferation and hypertrophy (Lui *et al.* , 2014; Mizuhashi *et al.* , 2018). The PTHrP-Ihh dynamics prove extremely difficult to analyse experimentally, thus much of the work that has contributed to our understanding of how these molecules interact with each other has been provided by way of mathematical model testing (Browers *et al.* , 2006; Garzón-Alvarado *et al.* , 2009, 2011; Narváez-Tovar & garzon Alvarado, 2012; Stevens *et al.* , 1999; Stevens & Beaupré, 1999). PTHrP is a molecule that is similar to parathyroid hormone (PTH) in that they both bind to the same receptor (PTH1R) and they both share some functional characteristics. PTHrP has been observed in cartilage, mammary gland, bone and cancerous tissues. Ihh is a

molecule that is synthesised by (pre-hypertrophic) chondrocytes in the proliferative zone and has only ever been observed in cartilage and bone tissues.

PTHrP diffuses through the growth plate from the ephiphyseal end, and is also synthesised by chondrocytes in the presence of Ihh expression. One of the effects of PTHrP is to promote proliferation of resting chondrocytes which causes them to enter the proliferative zone and PTHrP also promotes continued proliferation of chondrocytes that are already in the proliferative zone. PTHrP down regulates hypertrophic chondrocytes via inhibition of differentiation of proliferative chondrocytes into hypertrophic chondrocytes (Nishimori *et al.* , 2019). PTHrP can inhibit Ihh expression. Ihh also up regulates resting chondrocytes to enter the proliferative zone. Expression of Ihh is inhibited in the presence of expressed PTHrP. Ihh stimulates chondrocyte proliferation directly, and also indirectly by synthesising PTHrP. Increase in Ihh concentrations leads to increased PTHrP synthesis and thus PTHrP concentration.

The other chondrocyte-expressed molecule thought to play an important role in endochondral ossification are bone morphogenic proteins (BMPs). BMPs have a signalling gradient across the growth plate with a high concentration observed in the hypertrophic than in the resting zone (Lui *et al.* , 2014; Perry *et al.* , 2008). Chondrocyte-expressed BMPs are thought to have effect on the cell proliferation, differentiation and apoptosis of bone cells that are delivered at the metaphyseal vascular front (Garimella *et al.* , 2008).

Some of the other known paracrine and autocrine signalling factors within the growth plate include insulin-like growth factors (IGFs), fibroblast growth factors (FGFs), wingless/integrated proteins (Wnt), vascular endothelial growth factors (VEGFs), transforming growth factor (TGF-β), epidermal growth factor (EGF), C-type natriutic peptides (CNPs or NPPCs), and suppressor of cytokine signalling 2 (SOCS)(Xian, 2014; Lui *et al.* , 2014; Perry *et al.* , 2008; Modi *et al.* , 2011).

1.1.2.3 Vascular front

Further biochemical molecules with regulatory roles in growth plate evolution are delivered to the growth plate via the vascular front. Some of these endocrinal signals

include thyroid hormone, androgens, glucocorticoids, type I insulin growth factor (IGF-1), oestrogens and growth hormone (GH). How all of these additional endocrine signalling molecules interact with the local autocrine/paracrine signalling system within the growth plate is not fully understood (Lui *et al.* , 2014).

At the metaphyseal vascular front, bone cells are delivered to degrade and shape the emerging cartilage scaffold and to deposit bone (Walzer *et al.* , 2014). In addition to the above endocrine factors, bone cells produce further local regulatory cytokines into the system as they carry out remodelling of the emerging growth plate material. There are also endocrine factors that specifically influence the ensuing bone cell activity during the remodelling process. Bone remodelling is a process that occurs throughout the skeleton, throughout the organism's life, and will be explained in further detail for non-growth-plate-bone in Section 1.1.3. Whilst a comprehensive explanation of each cytokine factor affecting the bone cells is beyond the scope of this work, the number of factors alone give indication of the additional level of complexity that is integrated into this system for replacement of cartilage with bone. Some important factors include: hormonal parathyroid hormone (PTH), cytokines receptor activator for nuclear factor ligand (RANKL) and its receptor RANK, osteoprotegerin (OPG), Wnt signalling pathways, and both growth factors transforming growth factorS (TGF-β), and insulin-like growth factor-1 (IGF-1).

1.1.2.4 Bone cells

There are two types of bone cells involved in replacing the mineralised cartilage with bone. The first type of bone cell is a 'clastic' cell, which have a macrophage lineage and are responsible for resorbing cartilage and bone material. The two most well studied clastic cells are osteoclasts and chondroclasts. Chondroclasts are thought to be osteoclasts that sit on the surface of cartilage (Odgren *et al.* , 2016). The second type of cell is the osteoblast cell, having mesenchymal stem cell lineage, and being responsible for formation of bone (Matsuo & Irie, 2008). These two types of cells are tightly co-regulated and exactly how all of the cellular processes are involved in remodelling remains unclear. Co-regulation of osteoclasts and osteoblasts is sometimes referred to as the 'coupling phenomenon', and is influenced by the surrounding environment, systemic factors, and

by paracrine signalling communication between these cells (Garimella *et al.* , 2008; Erben, 1995).

Osteoclastogenesis involves the fusion of mononucleated osteoclast precursor cells (sometimes referred to as osteoclastogenic cells) that are derived from macrophage haemopoeitic tissue, to form large multinucleated osteoclast cells. There are several stages of osteoclastogenesis including recruitment, differentiation and precursor fusion, and finally functional activation (Cappariello *et al.* , 2014; Väänänen *et al.* , 2000). Osteoclasts have two roles. The first role of osteoclasts is to degrade hypertrophic cartilage. The second role of osteoclasts is to degrade bone, which requires dissolution of hydroxapatite. Hypertrophic cartilage is only located within the growth plate in healthy bone, however hypertrophic chondrocytes are also located in osteoarthritic articular cartilage. Once osteoclasts are activated at the metaphyseal vascular front, they resorb the emerging hypertrophic cartilage to create a trabecular cartilage scaffold in the primary spongiosa. Precursor osteoclasts can also interact with osteoblast precursors (osteogenic cells). As the calcified matrix scaffold is resorbed and reshaped by the activated osteoclasts, osteoblasts subsequently deposit bone and mineralise the trabecular bone scaffold. In this region the cancellous bone is composed predominantly of collagen I and hydroxyappatite (Rezende *et al.* , 2017). As the cancellous bone continues to travel away from the growth plate, the osteoclasts and osteoblasts carry out bone remodelling in the secondary spongiosa for optimised structure according to mechanical, biochemical and pharmacological conditions.

The active resorbing osteoclast has a ruffled border for secretion of acid, which is formed within a sealing zone. The sealing zone acts to confine the acidification molecules that are released through the ruffled border for demineralisation of collagen/bone materials (Touaitahuata *et al.* , 2014). Some studies have shown that osteoclasts without the ruffled border and/or sealing zone are still able to resorb the unmineralised component of bone (known as osteoid, the organic element of the bone), and thus are able to degrade the hypertrophic cartilage that emerges from the growth plate (Ralte *et al.* , 2011). Further work has shown that in some circumstances, osteoclasts can still remove calcified cartilage without the sealing zone function and the demineralisation function. Where mineral

dissolution is usually carried out by acid secretion at the ruffled border of osteoclasts, release of active proteases appear to suffice for osteoclasts to be able to degrade calcified cartilage. This may be attributed to the calcified cartilage structure being less stiff than bone, having a higher level of hydration than bone, and having a structure with a more 'loose' interaction between cartilage and minerals (Touaitahuata *et al.* , 2014).

In one study, where osteoclasts have had their ability to form a sealing zone 'knocked out', the hypertrophic cartilage scaffold has still been sufficiently degraded (Touaitahuata *et al.* , 2014). However, the trabecular bone scaffold that had been laid down by osteoblasts has not been sufficiently degraded in the primary and secondary spongiosa. In this scenario, the resulting cancellous bone structure that emerges in the secondary spongiosa has been reported as being far more dense than that seen in cancellous bone that is undergoing endochondral ossification under normal conditions.

1.1.2.5 RANK-RANKL-OPG

OPG-RANK-RANKL together form a fundamental cytokine system that is widely considered to be essential for regulation of the coupling between osteoblasts and osteoclasts for carrying out remodelling in the primary and secondary spongiosa, and in fact, for all bone remodelling that occurs throughout the skeleton. This local signalling system is influenced by PTH, calcitonin, TGF-β, interleukin 1 (IL-1), and oestrogens. The RANKL/OPG ratio is commonly used in mathematical modelling as the central determinant of bone remodelling outcome (Komarova *et al.* , 2003; Ryser *et al.* , 2010; Turner, 1999; Lotinum *et al.* , 2003; Komarova, 2006, 2004).

RANKL (ligand) is expressed by osteoblasts and binds to the RANK receptor on osteoclast precursors to simulate maturation of osteoclast precursors (Alliston & Derynck, 2002). This is a necessary process for osteoclastogenesis. In the absence of RANKL, bone resorption cannot occur normally. RANKL also binds to RANK receptors on mature osteoclasts to stimulate resorption (Teitelbaum, 2000). OPG is expressed by osteoblasts and osteoblast stromal cells, and acts as a RANKL decoy to prevent RANK-RANKL binding. The OPG decoy binding serves to inhibit osteoclast maturation and osteoclast

resorption. OPG-RANK activity causes osteoclast resorption at a remodelling site to pause so that osteoblasts can deposit bone.

PTH also stimulates osteoclastogenesis and osteoclast resorption activity by binding to cell-surface receptors on osteoblasts to stimulate osteoblast-expressed RANK. There are also reports that PTH has caused a reduction in osteoblast apoptosis (Jilka *et al.* , 2007). The overall effects of PTH can vary. Intermittent PTH concentration can have an anabolic outcome (bone building), and continuous concentration can have a pro-resorptive outcome (Trichilo *et al.* , 2019; Komarova, 2004).

TGF-β increases formation by directly affecting osteoblast differentiation and can also increase OPG expression. There are special calcium sensing receptors that also signal to increase PTH concentration, for increased resorption when calcium levels are low. PTH is known to activate osteoclastogenesis in absence of osteoblasts, and has been shown to inhibit osteoclastogenesis in cultures that contain both osteoblasts and osteoclasts by decreasing expression of osteoblast-expressed RANKL. TFGβ is another important factor in maintaining balance between resorption and formation due to having an influence on lineages of both osteoclasts and osteoblasts (Yau *et al.* , 2006).

1.1.2.6 Oestrogen

Oestrogen predominantly acts on osteoblast cells, and alters expression of osteoblast expressed RANK and OPG to suppress bone resorption and to stimulate bone formation. Oestrogen both increases OPG concentration and decreases RANKL concentration. Oestrogen can also stimulate osteogenesis in osteoblasts precursor cells, and can prevent osteoblasts from undergoing apoptosis (Börjesson *et al.* , 2013). Oestrogen has been demonstrated to cause different effects on growth rates, depending on the age that oestrogen levels change, and there is evidence that oestrogen can both slow or increase the rate of growth, and reduce overall growth (Börjesson *et al.* , 2013; Boyce *et al.* , 2014). In early puberty, applied oestrogen caused an increase in growth spurts and growth was overall enhanced, yet oestrogen applied in late puberty had the opposite effect, causing early fusion of the growth plate. Growth plate growth factors PTHrP and IL-1 may also

affect osteoblast expressed RANKL to increase osteoclast activity.

There are a few other less critical molecules that have been shown to influence remodelling processes. Osteoclasts may be able stimulate bone formation directly through expression of BMPs (Garimella *et al.* , 2008). BMPs are potentially important for the recruitment, proliferation and differentiation of osteoblasts at remodelling sites. Improvement of gap junction intercellular communication may also affect the regulation of coupling between osteoblasts and osteoclasts (Jorgensen *et al.* , 2004). Gap junction channels are pores through which cells can communicate by coordinating signals and responses to hormones. Anti-arrhythmic peptides (AAP) enhance conductivity between gap junctions, and they have been found to demonstrate specific binding to osteoblasts. Leptin-regulated neural pathways also promise an important role in the regulation of bone cell coupling by altering RANKL expression to increase or dampen resorption (Elefteriou *et al.* , 2004).

1.1.3 Bone remodelling

Bone remodelling occurs throughout the skeleton during growth in both cortical and trabecular bone, and continues after growth ceases for the lifespan of the organism. There are two types of remodelling, *targeted* remodelling and *random* remodelling. Targeted remodelling provides a mechanism for repair to micro-damage, and adaptation to external loading conditions (Martin, 2008; Ruimerman *et al.* , 2005; Chow *et al.* , 1998; Parfitt, 2002). This type of remodelling is both temporally and spatially specific such that particular sites are targeted for bone restoration or load-dependent change. In contrast, random remodelling occurs at supposedly random sites to ensure that every part of the 'old' skeleton gets replaced with 'new' bone periodically. Random remodelling helps to maintain the integrity of the skeleton (Komarova *et al.* , 2003). In the human skeleton, roughly ten percent of bone mass is replaced every year by random remodelling (Allister & Derynck, 2002). Possibly, random remodelling may not be strictly random. The probability of random remodelling events could be related to the age of the bone (Parfit, 2002). Also, as old bone is resorbed for new bone replacement, minerals are released and random remodelling is important for calcium homeostasis. Calcium is an important

signalling molecule throughout the body.

Targeted and random remodelling are carried out by the same two bone cells that remodel the collagen and bone material in the primary spongiosa next to the growth plate, namely osteoclasts and osteoblasts. These cells are also coupled and use the same autocrine and paracrine RANK-RANKL-OPG system to conduct remodelling, and form what is known as 'basic multicellular units' (BMUs). For these processes, a third bone cell is involved, the osteocyte, which is said to have a mechanosensory role towards signalling for the initiation and possibly also the cessation of a remodelling event. Osteocytes may also have an important role in endochondral ossification, though this is not well understood. For a remodelling event, once the signal for repair takes effect, osteoclasts are recruited to excavate a resorption cavity and then osteoblasts subsequently fill in the cavity with new bone to create a new osteon, the basic structural unit of cortical bone or a new hemi-osteon, the basic structural unit of cancellous bone (Figure 1.3).

After a remodelling event, some osteoblasts undergo apoptosis, and some osteoblasts become embedded in small lacunae (cavities), within the newly formed cellular matrix (ichi Nakahama, 2010). After undergoing morphological modification, the embedded osteoblasts become osteocytes. Osteocytes are capable of intercellular cytoplasmic communication via extensive canaliculi (canal networks) which connect radiating lacunae within the bone matrix (Burger & Klein-Nulend, 1999; Buenzli & Sims, 2015). Communication between osteocytes is most likely to be predominantly via gap junctions between adjacent osteocytes (Matsuo & Irie, 2008).

Osteocyte cells are thought to detect both micro-damage and deformation (Lanyon, 1993). Under the conditions of micro-damage, apoptosis of osteocytes at the damage site could signal the need for repair (Fyhrie & Schaffler, 1995). Under external changes to loading condition, osteocytes act as mechanosensors via their sensitivity to small fluid shear stresses caused by deformation (Weinbaum *et al.* , 1994; Lanyon, 1993; Huiskes *et al.* , 2000). One of the mechanisms reported for detection of fluid flow is via primary cilia projected from the osteocyte cell surface (Malone *et al.* , 2007). Osteocytes are said to signal for adaptation to external loading in response to both increased and decreased impact-loading, and to immobilisation (Young *et al.* , 1986; Courteix *et al.* , 1998; Muller,

2005).

With age, disruption to bone remodelling can occur over time and skeletal disorders such as osteoporosis and osteoarthritis are commonly seen in the elderly population (Bilezikian *et al.* , 2009). Bone density and structural quality deteriorate due to loss of trabecular mass, leading to risk of fragility fractures (Tsangari *et al.* , 2006; Lane *et al.* , 2003). In particular, women in the early years following menopause suffer from bone loss due to oestrogen deficiency. Oestrogen deficiency predominantly causes elevated rates of remodelling, and also causes a negative imbalance between resorption and formation during individual remodelling events. (Tsangari *et al.* , 2006).

1.1.3.1 In vitro, in vivo and in silico testing

As with the remodelling system situated in the primary spongiosa, the remodelling of bone is very difficult to analyse experimentally. In vitro observations do not always translate to observed in vivo dynamics. Though bone is dynamic, the time scale makes resolution of the dynamics very challenging. Often, morphometric and histomorphometric methods for analysing remodelling parameters in vivo have been carried out and reported, based on the tacit assumption that the modelling parameters are uniform throughout the metaphysis.

Historically, the vast majority of studies investigating architectural changes over time in animal models have been cross-sectional by design. Animals are sacrificed at strategic time points, and analysis is performed in vitro via histology. This approach is limiting due to variation between animal cohorts and cohorts under different experimental treatments. Thus large numbers of animals are required. Most histologically derived remodelling parameters that are reported assume that the parameters are uniformly distributed throughout the trabecular structure by definition (Parfitt *et al.* , 1983, 1987). Such an assumption is particularly problematic for parameters that are dynamic and derived from static indices. Consequently, studies that use formula-derived indices to characterise trabecular structure have to rely on the assumption remodelling processes

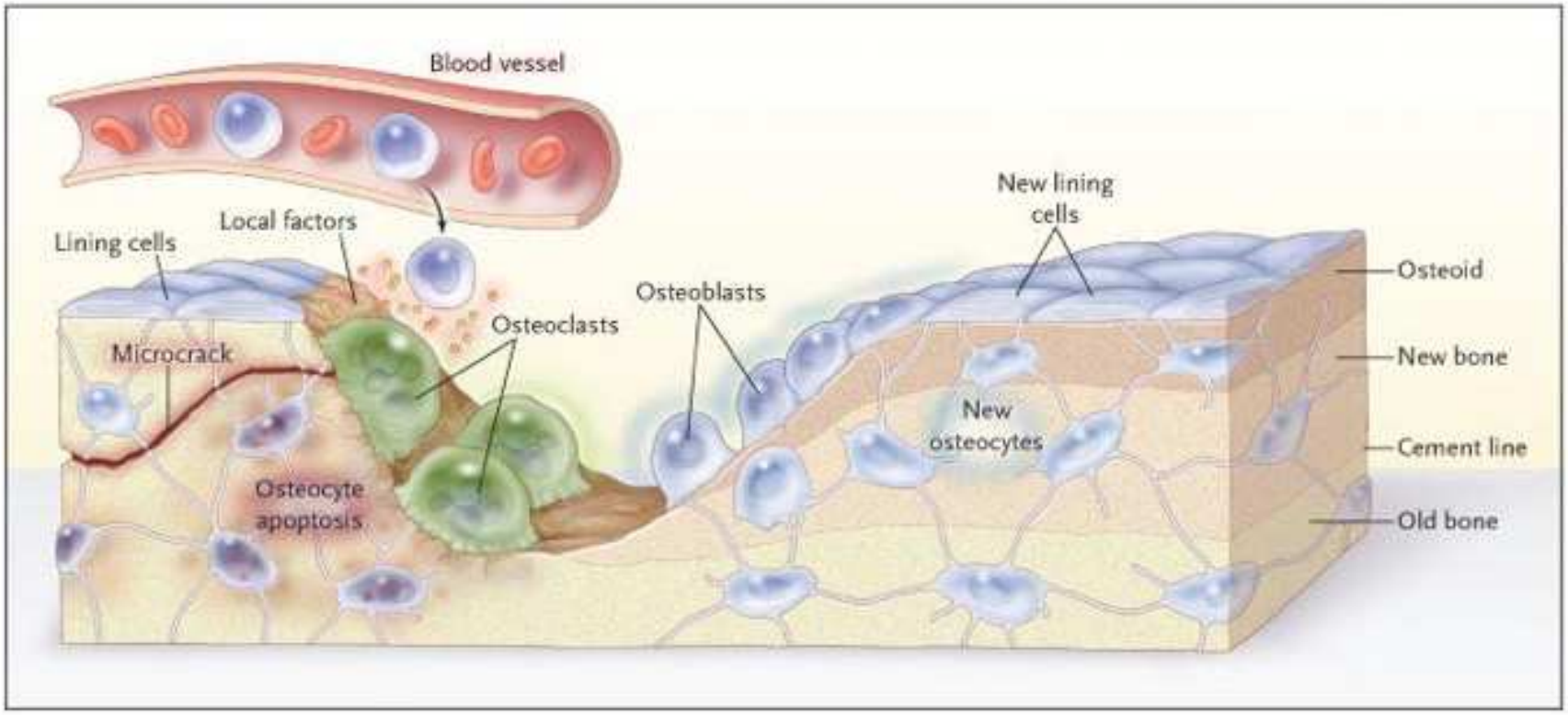

Figure 1.3: Remodelling event carried out by a BMU (Reproduced with permission from Massachusetts Medical Society). First the osteoclast cells (green) break down and remove bone material during bone resorption, and then osteoblast cells (blue) subsequently deposit new bone. After cessation of a remodelling event, some osteoblast cells will undergo apoptosis, and some will become embedded in the bone matrix to become osteocyte cells.

are uniform throughout the trabecular structure (Wronski *et al.* , 1989; Brouwers *et al.* , 2008; Li & Wronski, 1995). With the advent of μ-CT technology, new non-destructive longitudinal methods are made possible for assessing three-dimensional structures (Boyd *et al.* , 2006). However, for time-course studies, structural attributes are still usually averaged over a single large region of bone to study remodelling processes rather than reporting the attributes for several sub-sections of bone for viewing attributes as functions of distance relative to growth plate (Perilli *et al.* , 2009; Boyd *et al.* , 2006; Browers *et al.* , 2006).

Another approach to characterising metabolic activity is the use of biochemical bone turnover markers (Štěpán *et al.* , 1987; Clowes *et al.* , 2002; Reginster *et al.* , 2007; Cremers & Garnero, 2006; Russell *et al.* , 2008; Seeman, 2009; Brown *et al.* , 2009; Fleisch, 1998; Nyman *et al.* , 2004; Riggs & Parfitt, 2005; Brouwers *et al.* , 2008; Evans *et al.* , 2003). Bone turnover markers are proteins found in blood or urine which are released during metabolic activity. These proteins act as quantitative non-invasive measures of changes to either resorption or formation rates. Biochemical markers are therefore unable to give any information about local changes. Further, turnover markers are considered to be proven useful only on account that their presence in blood or urine always correlates well with what is described as the 'actual rate' of turnover an histologically-derived dynamic parameter that is also based on the assumption of parameter uniformity (Cremers & Garnero, 2006).

Mathematical modelling Much of the current understanding of remodelling and BMU dynamics has come from extensive mathematical modelling contributions. Bone remodelling is multifaceted and multiscale, and a full survey of mathematical modelling studies is beyond the scope of the thesis, though a few of the important works deserve mention. There have been several reviews of mathematical modelling in this area, extending to studies that test outcomes at the biochemical or tissue scale, and at the mechanical and larger tissue scale (Pivonka & Komarova, 2010; Martin, 1985; Komarova, 2006).

Local cellular processes have been modelled to investigate remodelling at the level of the BMU (Buenzli *et al.* , 2013, 2011; Ryser *et al.* , 2010; Komarova *et al.* , 2003; Lemaire

et al. , 2004; Turner, 1999; Martin & Buckland-Wright, 2004; Alias & Buenzli, 2018; Tkachenko *et al.* , 2009; Piekarski & Munro, 1977; loana Pastrama *et al.* , 2018; Schulte *et al.* , 2013; Komarova, 2004). These modelling studies describe BMU dynamics with explicit representation of important bone cells like osteoclasts, osteoblasts and ostocytes. Typically, models developed at the cellular scale include Michaelis-Menten mass action kinetics for concentrations of bone cells and are often presented in systems of ordinary differential equations (ODEs). Models that describe cell population dynamics have been able to investigate some of the signalling pathways in this system, including interactions between signalling molecules RANK, RANKL, and OPG. Another key feature for modelling these processes at the cellular scale, is the ability to describe spatial arrangement of the BMU over time.

Many efforts have been made towards modelling the larger scale mechanics that plays a role in bone remodelling (Weinbaum *et al.* , 1994; Cowin *et al.* , 1991; Cowin & Wienbaum, 1998; Cowin, 2007; Mi *et al.* , 2005; Weinan & GRootenboer, 1992; Mullender & Huiskes, 1997; Huiskes *et al.* , 1997, 2000; Mullender *et al.* , 1994; Prendergast *et al.* , 1997; Ruimerman *et al.* , 2005; Turner, 1999; Geris *et al.* , 2009; van der Meulen *et al.* , 2006; Guo & Kim, 2002; Liu *et al.* , 2009; Fyhrie & Schaffler, 1995; Levenston, 1997; Stulpner *et al.* , 1997; Coelho *et al.* , 2009; Burr *et al.* , 1985; Cowin, 2005; SIFFERT *et al.* , 1996). Large scale mechanics have been included in models to investigate the role of local stresses on bone remodelling. These models help to identify the effects of mechanical forces on the adaptation and maintenance of the skeleton, and allow for testing of mechanosensory mechanisms that induce changes to the remodelling machinery. Finite element models have been instrumental towards testing the relationship between applied loading and structural changes to trabecular architecture.

Some mathematical models combine local cellular processes with mechanosensory parameters or lager scale dynamics (Wimpenney & Moroz, 2006; Buenzli *et al.* , 2011; Pivonka *et al.* , 2013; Scheiner *et al.* , 2013; Weinbaum *et al.* , 1994; Tayyar *et al.* , 1999; Ruimerman *et al.* , 2005; Wang *et al.* , 2011; Scheiner *et al.* , 2010; van Oers *et al.* , 2007). These multiscale approaches have helped to provide a link between the effects of mechanical forces and the resulting complex remodelling processes that allow the trabecular

architecture to adapt to loading conditions and to repair microdamage.

A few other areas of bone remodelling that have been aided by the development of mathematical models include the role of nutrient transport (Piekarski & Munro, 1977; Scheiner *et al.* , 2010); bone regeneration and fracture healing (Adam, 1999, 2002; Geris *et al.* , 2008, 2009; Ambard & Swider, 2006; Chow *et al.* , 1998; Reed *et al.* , 2002; Perren, 1979; Carter, 1987; Carter *et al.* , 1998; Henderson & Carter, 2002; Stevens *et al.* , 1999; Ament & Hofer, 2000; Bailon-Plaza & Meulen, 2003; Liu *et al.* , 2009; Muller, 2005; Shefelbine *et al.* , 2005; Claes & Heigele, 1999; Prendergast *et al.* , 1997; Dickson *et al.* , 2007; Mastrogiacombo *et al.* , 2007; Cornea *et al.* , 2005); and the relationship between cancer and remodelling in the bone microenvironment (Wang *et al.* , 2011).

1.1.4 Bone loss and treatments

Treatments for bone loss and osteoporosis fall into two categories, *anabolic* and *anti-resorptive* (sometimes referred to as *anti-catabolic*). So far PTH is the most successful anabolic treatment, due to a bone-building effect on osteoblast cells via the OPG-RANK-RANKL system (Girotra *et al.* , 2006). Oestrogen has also been investigated for use as an anabolic agent, due to having a similar effect to PTH via the OPG-RANK-RANKL system. However the systemic effects of oestrogen throughout the body result in too many negative side effects that offset the desirable anabolic effects in the bone microenvironment. Work is currently being done to investigate a locally administered oestrogen dosing regiment. In addition to PTH and oestrogen, other agents under study for potential anabolic treatments include strontium ranelate GH, IGF-1 and bFGF.

1.1.4.1 Bisphosphonates

Bisphosphonates are currently the leading class of anti-resorptive drugs for the treatment of bone loss and osteoporosis, and are widely used for diseases that are associated with elevated resorption or malignancy in both growing and mature patients (Nancollas *et al.* , 2005). Bisphosphonates are used to treat patients for paediatric osteoporosis and

juvenile osteoporosis, and secondary osteoporosis that is associated with bone disorders such as junior Paget's disease, osteogenesis imperfecta (OI), malabsorption syndromes, corticosteroid-dependent asthma and neuromuscular disorders, or from steroid medication (Russell *et al.* , 2008; Muderis *et al.* , 2007; Boyce *et al.* , 2014; Silverman, 2011; Kumar *et al.* , 2016). Bisphosphonates are also used to treat mature patients with osteoporosis caused by oestrogen deficiency, implant integration, age related bone loss, and also to treat metastatic and osteolytic bone disease, and hyperglycaemia of malignancy (Tenta *et al.* , 2006; Silverman, 2011; Coleman, 2010; Carvas *et al.* , 2010; Khosla & Hopbauer, 2017; Lupion *et al.* , 2018). The pharmacological mechanism of action of bisphosphonates is still not completely understood (Cremers *et al.* , 2019; Holstein, 2019).

Effects on bone remodelling Bisphosphonates are known to reduce the number of BMUs activated for remodelling, thus reducing the overall rate of remodelling (Riggs & Parfitt, 2005; Allen, 2018). In situations where bisphosphonate suppression of BMU activation frequency is too great or prolonged, accumulated damage may increase (Seeman, 2009, 2003; Seeman & Martin, 2019; Visekruna *et al.* , 2008). Bisphosphonates also decrease the resorption volume to create a positive bone balance for a given remodelling event (Seeman & Delmas, 2006). In addition to inhibiting resorption, some studies indicate a pro-formation effect for bisphosphonates, by way of osteoblastogenesis and increasing the proliferation of osteoblast cells (Fleisch, 1998; Bukowski *et al.* , 2005). Bisphosphonates are internalised by osteoclast cells. As new evidence continues to merge, there are a growing number of proposals for the cellular mechanisms that cause suppression of osteoclastic function and bone resorption. Some of the mechanisms responsible include: direct inhibition of osteoclast differentiation; indirect effect on osteoclast by enhancing inhibitory signals in osteoblasts; induced apoptosis in osteoclasts; inhibition of calcification; inhibition of osteoclast precursors; disruption to trafficking of proteins/membranes; inhibition of the ability for osteoclasts to attach to bone; disruption to the formation of the osteoclasts's ruffled border; and disruption to the osteoclast cytoskeleton to inhibit activation (Nyman *et al.* , 2004; Ralte *et al.* , 2011; Tenta *et al.* , 2006; D'Amelio *et al.* , 2010; Xu *et al.* , 2013; Russell *et al.* , 2008).

Effects on endochondral ossification There are two types of bisphosphonates, nitrogen-containing bisphosphonates and non-nitrogen-containing bisphosphonates, and these two types are known to reduce resorption via different enzyme pathways. The effects of bisphosphonates on resorption during growth are still incompletely understood (Rezende *et al.* , 2017). Both nitrogenated and non-nitrogenated have been shown to disrupt endochondral ossification (Evans *et al.* , 2003; Rezende *et al.* , 2017), and both are known to negatively affect osteoblast and osteoclast processes in the primary spongiosa, though with slightly different outcome. Zoledronic acid is the most commonly used bisphosphonate for treatment of bone loss, which is a third generation nitrogen-containing bisphosphonate with high potency. Some studies have shown that zoledronic acid may slow growth or stop growth altogether (Schenk *et al.* , 1986; Reitsma *et al.* , 1980; Pataki *et al.* , 1997; Hornby *et al.* , 2003; Erdogan *et al.* , 2019).

Hypertrophic cartilage Several studies have reported that in nitrogenated bisphosphonate treated animals, the resorption of calcified hypetrophic cartilage had been significantly inhibited during endochondral ossification, and that the calcified cartilage was found to persist in the secondary spongiosa (Rezende *et al.* , 2017; Rao *et al.* , 2008). Similarly, non-nitrogenated bisphosphonates have been described as 'chondoprotective' in osteoarthritic hyaline articular cartilage (She *et al.* , 2017; Shirai *et al.* , 2011). Non-nitrogenated bisphosphonates may prevent the degradation of articular joint cartilage by inhibition of osteoclast resorption activity and of osteoclasts that are located in the subchondral bone adjacent to the cartilaginous material (Shirai *et al.* , 2011).

Osteoclast number and activity Rezende *et al.* (2017) reported that the expression of both RANK and OPG decreased in nitrogenated bisphosphonate treated bone compared to normal bone. Surprisingly, Rezende *et al.* (2017) also found that number of osteoclasts in the primary spongiosa and secondary spongiosa was still high, thus concluding that nitrogenated bisphosphonates do not necessarily down-regulate the recruitment or differentiation of osteoclasts. However, the osteoclasts that were present in this region were identified as latent, due to inhibited osteoclast activation and osteoclast function. Ralte *et al.* (2011) reported similar findings. Both the number and the size

of osteoclasts actually increased in zoledronic treated secondary spongiosal bone. The osteoclasts were similarly unable to resorb bone due to a smaller (defective) ruffled border. Here, the smaller ruffled border was reported as being absent in osteoclasts that were sitting on cartilaginous surfaces which either means that the osteoclasts were either not able to resorb hypertrophic cartilage, or that the osteoclasts were able to resorb the hypertrophic cartilage without the border by way of proteases.

PTHrP Tenta *et al.* (2006) reported that one of the observed effects of zoledronic acid in vitro was the suppression of PTHrP. If zoledronic has the ability to suppress PTHrP at the growth plate, the consequence could be down regulation of chondrocyte proliferation, or up regulation of chondrocyte hypertrophy. If zoledronic acid has the ability to suppress PTHrP at the growth plate via the vascular front, this could possibly also result in an alteration to the expression of RANK towards decreasing osteoclast function.

Cancellous bone Significantly dense trabecular bone has been observed in the secondary spongiosa, in most bisphosphonate treated animals during endochondral ossification (Hornby *et al.* , 2003; Rezende *et al.* , 2017; Ralte *et al.* , 2011). Drastic changes to bone density as new bone material is ossified at the growth plate under bisphosphonate treatment potentially creates fracture risk at the point where very dense bone sharply meets the less dense bone that had emerged earlier, prior to treatment. Several studies have seen the emergence of what are termed 'zebra lines' (Muderis *et al.* , 2007) during endochondral ossification in bisphosphonate treated children and animals (Schenk *et al.* , 1973; Muderis *et al.* , 2007; Biggin *et al.* , 2014; Ishizuka *et al.* , 2017; Corsi *et al.* , 2017). Zebra lines describe the elevated bone density of the emerging bone according to bisphosphonate dosing regimens, where there are sharp increases in density of tibial bone closest to the growth plate soon after the time of treatments. In between bisphosphonate treatments, the bone emerges from the primary spongiosa with normal (lower) density. One of the considerations for treating children with bisphosphonates, is to reduce injection-trauma by adopting less frequent, high-dose injection schemes. The slerotic zebra lines could pose a risk for fractures at the locations where there are sharp density gradients and may be eradicated with more frequent, low dose injections. Some

studies have reported the detection of zoledronic acid in children as long as eight years after discontinuation of treatment (Boyce *et al.* , 2014).

1.2 Thesis overview

The mathematical modelling carried out for this work is described at the tissue scale and is thus nested in between mechanical and cellular scales. Historically, mathematical models have been developed for several of the aspects considered in this study independently, including models for endochondral ossification (Section 1.1.2) and remodelling (Section 1.1.3.1), however most of what is known about the effects of bisphosphonates on cancellous bone in growing cohorts is by way of in vitro and in vivo experimental work. Conclusive evidence is lacking, and most work in this area is based on histological analysis of bone tissue. There is a sense of urgency for a better understanding of bisphosphonate treated growing bone, as bisphosphonates are currently the mainstay for treating osteoporosis in children and juveniles.

1.2.1 Thesis objectives

The work conducted in this study aims to construct a simplified partial differential equation (PDE) model for BV/TV in terms of bone remodelling parameters, and to optimise model parameters over longitudinal experimental data. The experimental data includes μCT scans of cancellous bone in the secondary spongiosa for juvenile rats from three groups including sham-operated rats (sham), ovariectomised rats (ovx) and ovariectomised rats treated with zoledronic acid (ovx+zol). This combined approach will be implemented to investigate the effects of ovx and ovx+zol on bone remodelling processes in growing bone.

More specifically, the research focus for this study includes the following objectives:

- to briefly describe BV/TV observations in the experimental data qualitatively, as a function of distance relative to the growth plate;

- to briefly investigate changes to experimental BV/TV over time within each group and to compare BV/TV over time between groups;
- to develop a mechanistic PDE model for BV/TV in growing rats, in terms of coupled BMU remodelling events at the tissue scale;
- to optimise model parameters by fitting the analytic solution of the PDE model for BV/TV to the experimental BV/TV data; and
- to identify the dominant effects of ovx and ovx+zol on bone remodelling parameters in growing rats.

1.2.2 Structure of the thesis

An overview of the experimental rat data used for this study is given in Chapter 2. The structure of material in the primary spongiosa which is adjacent to the growth plate is predominantly composed of hypertrophic cartilage, and this material cannot be resolved with current μCT scanning technology. Consequently, for this study, the volume of interest begins farther away from the growth plate where the bone transitions from primary spongiosa to secondary spongiosa. The secondary spongiosa of the tibial metaphysis in rats is widely used to study changes to remodelling processes over time and the rat is considered an appropriate animal model for human bone (Wronski & Liang, 1999; Li & Wronski, 1995). Also included in Chapter 2, is a brief summary of preliminary observations that were made for BV/TV in the experimental data. Supplementary material for early BV/TV observations is provided in Appendix A. In Chapter 3, a novel approach is presented for investigating the basic relationship between BV/TV of growing bone and bone remodelling at the level of the BMU, in terms of fundamental remodelling parameters. Here, a PDE model is derived to describe the change in BV/TV throughout the secondary spongiosa over time, according to the rate of bone remodelling, and coupled bone resorption and bone formation. The model is developed at the tissue scale only. No effort was made to describe the cellular dynamics that lead to individual remodelling events, nor the mechanical strains that influence these processes. The model for

BV/TV is a spatial extension to ordinary differential equation (ODE) models that were developed prior to this study. These models are summarised in Appendix B. The full analytic solution that was derived for the construction of the final model for BV/TV is given in Appendix B. Chapter 4 details the methods of optimisation that were implemented for identifying values of the model parameters which best describe BV/TV observations in the experimental data. The model parameters were found by applying optimisation methods for comparison of BV/TV model predictions against BV/TV in the experimental data. The model results are presented in Chapter 5. Supplementary figures and tables for results presented in Chapter 5 are provided in Appendix C. In Chapter 6, a review of the results is presented including the dominant effects of ovx and ovx+zol on bone remodelling, clinical implications, model limitations, directions for future research, and a discussion of open questions which require additional in vivo and in silico testing. A final summary is presented in Chapter 7.

Chapter 2

Data

Experimental data for this project consisted of μCT data collected as part of a larger longitudinal study on cortical and cancellous bone structure (Perilli *et al.* , 2009; Fazzalari *et al.* , 2012; Gontar *et al.* , 2018; Martin & Bottema, 2015). A group of thirty juvenile Sprague-Dawley rats aged roughly 8 weeks, were randomly assigned to three experimental groups of ten rats each.

1. Ten rats were given a bilateral ovariectomy causing an oestrogen deficiency (ovx group);

2. Ten rats were given a bilateral ovariectomy, then given weekly treatments of bisphosphonate Zoledronic acid beginning fourteen days after surgery (ovx+zol group);

3. Ten rats were used as a control and underwent a sham surgery to simulate exposure to surgical conditions. They were opened up but not ovariectomised (sham group).

Throughout, time will be measured in days from the time of the event of the surgery, $t = 0$. μCT scans of the proximal tibia were performed at $t = 0$, immediately after surgery, and at $t = 14, 28, 56$, and 84. One ovx rat and two ovx+zol rats died prior to μCT scanning at $t = 84$ (Appendix A.1). Handling of the animals and the associated

μ-CT procedures were carried out prior to this study and the details can be found in Appendix A.2.1.

2.1 Post-processing of μCT data

For this study, the inherited raw reconstructed data were extracted from a larger data set and prepared as binarised volumes. From here on out all further methods are presented as original work, as conducted for the purpose of this study. All computations were carried out using the scientific computing package in MATLAB©.

2.1.1 Bone block extraction

For each of the rats and each time point, a block of 121 × 121 × 400 voxels (1.0529mm ×1.0529mm × 3.4808mm) comprising proximal cancellous bone was selected manually from the reconstructed data, at resolution of $0.0087 \times 0.0087 \times 0.0087 mm^3$ per voxel. This was the largest volume that could be extracted consistently over all samples without including cortical bone. These 121 × 121 × 400 voxel arrays (1.0529mm ×1.0529mm × 3.4808mm) will be referred to as *bone blocks*. The bone block was extracted from from roughly the same location for each rat, nominally along the medial axis, positioned 138 μCT slices (1.2mm) from the edge of the growth plate. While this protocol sufficed to identify the same general location within the tibia, voxel by voxel alignment could not be reproduced consistently. In rats, the bone transitions from primary spongiosa to secondary spongiosa 0.756mm-1.188mm from the growth plate (Kimmel & Jee, 1980), placing the extracted bone blocks in the secondary spongiosa. Secondary spongiosal bone in rats has an average age of at least 7 days.

For convenience, from here on out, the orientation of the medial axis will be considered as horizontal, where 'left' refers to the end of the metaphysis that is close to the growth plate and 'right' refers to the end of the metaphysis further away from the growth plate.

The bone blocks were selected manually to find an axis of length 400 slices so that the square of size 121×121 pixels situated on the axis fit within the cancellous bone for each slice, starting at slice 138 slices to the right of the growth plate (Figure 2.1). The edge of each bone block that is closest to the growth plate is approximately 1.2mm from the growth plate, and the length of each bone block extends to approximately 4.7mm from the growth plate.

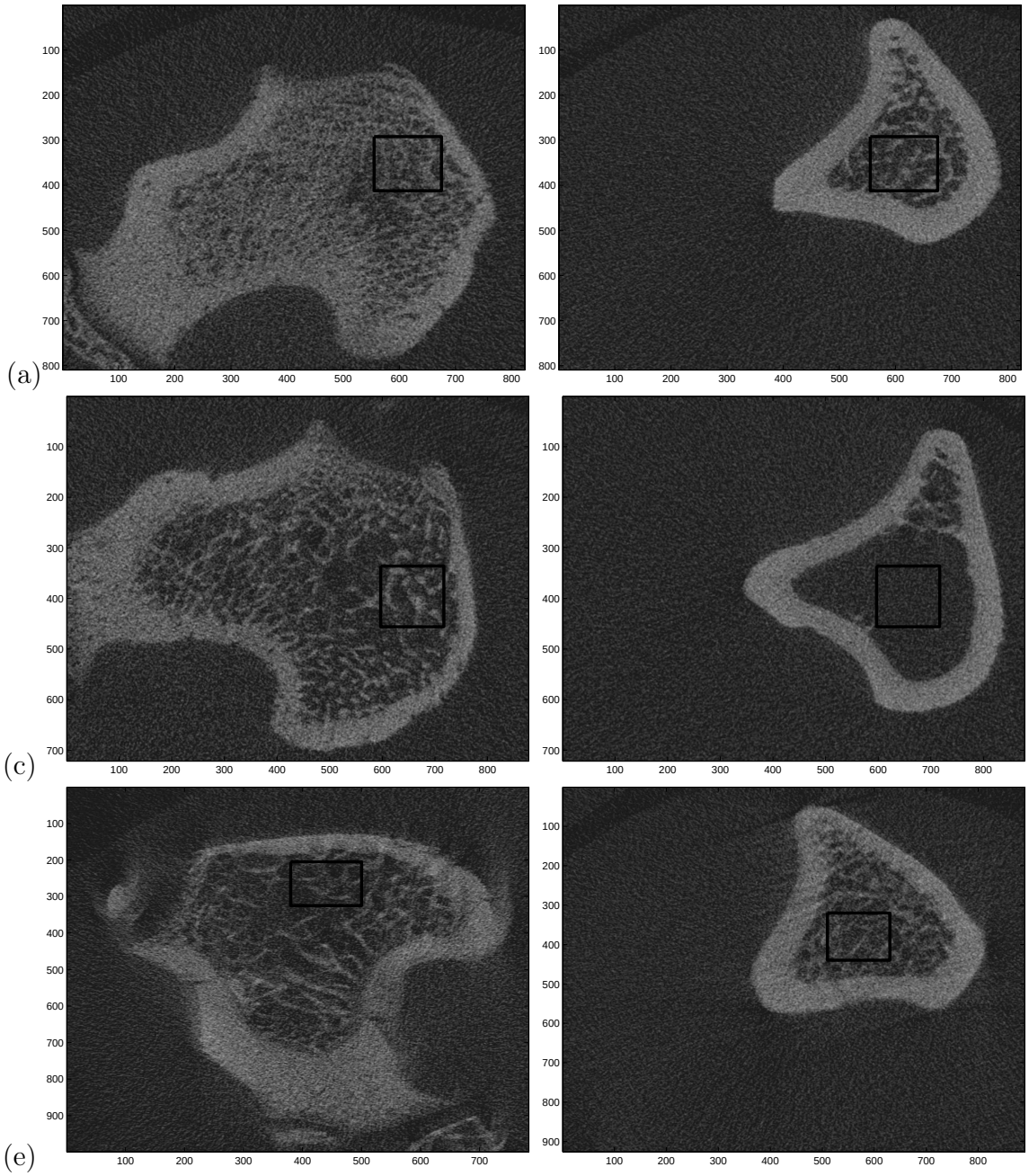

Figure 2.1: Examples of the selection of cancellous region for extraction of bone blocks along the medial axis including the leftmost image in the data window 1.2mm from the growth plate (left slice) and the far end of the bone block 4.7mm from the growth plate (right slice) at $t = 56$ for (a) a sham rat, (b) an ovx rat, and (c) an ovx+zol rat. Dimensions of the square on images are 120 ×120 pixels (1.0529mm ×1.0529mm), though they appear to be rectangles due to the aspect ratio of the axes.

2.1.2 Binarisation

A single global threshold was determined using Otsu's method (Otsu, 1978), which is a standard process for identifying an optimal threshold to separate bimodal two-class data, usually for binarisation of greyscale images or for image segmentation. Otsu's method was used to binarise three cross-sections of the extracted bone blocks along the vertical/horizontal axes for 3 rats from each group at $t = 0$ and at a later time point after which all of the experimental treatments took effect at $t = 56$. Preliminary results showed this sampling method to be robust. The mean binarisation threshold value was found to be 0.233 ± 0.0463 thus the global threshold value was taken to be 0.233 (23%).

2.1.3 Morphological filtering

Experiments were conducted to investigate the use of morphological filtering for the removal of isolated artefacts that appeared in the bone blocks after the binarisation step, and to eliminate any other imperfections or distortion due to noise (Serra, 1982). BV/TV of the largest connected component was compared to the sum of the BV/TV of all the components for the following:

- binarised bone blocks;
- binarised bone blocks after performing morphological closing and opening with a structuring element, comprising a cube with all values equal to one, of size $3 \times 3 \times 3$ voxels; and
- binarised bone blocks after performing morphological closing and opening with a structuring element, comprising a cube with all values equal to one, of size $5 \times 5 \times 5$ voxels.

The use of a structuring element comprising a cube of size $5 \times 5 \times 5$ voxels returned overall BV/TV values that were much greater than the original BV/TV the original binarised bone blocks. Further, the use of a structuring element cube of size $5 \times 5 \times 5$ voxels resulted in a lessened volume of the components that were not connected to the largest

component. Thus a structuring element comprising a cube of size $3 \times 3 \times 3$ voxels was considered best, and was used for morphological closing then opening of the binarised bone blocks. Components with volume less than 1000 voxels were also removed from the bone blocks to reduce noise.

The final bone blocks were binarised using a single threshold 0.233 (23%) with morphological closing then opening applied using the $3 \times 3 \times 3$ structuring element, to arrive at the binary three-dimensional bone blocks of size $121 \times 121 \times 400$ voxels. Example bone blocks are displayed for $t = 0, 28, 84$ in Figure 2.2, and bone blocks for all time points are displayed in Appendix A (Figure A.1).

2.2 Experimental data analysis

In rats, tibial metaphyseal cancellous bone displays decreasing BV/TV with distance from the growth plate (Gabet *et al.* , 2008; Weber *et al.* , 2002). The trabecular structure is more dense closer to the growth plate compared to cancellous bone further away from the growth plate. Exactly how the BV/TV gradient changes over time has not been reported in detail. Longitudinal (temporal) changes to BV/TV are generally measured and reported with the assumption that changes to BV/TV are the same throughout the volume of interest. Usually only a single BV/TV value is reported for any given time-point.

Prior to developing models to describe the mechanistic changes that drive the BV/TV changes seen in the data, some preliminary observations were made by inspection of the relationship between BV/TV and the distance from the growth plate over time in the juvenile growing rats. An effort was made to understand BV/TV as a function of distance from the growth plate, rather than reporting an exhaustive list of BV/TV values that extend throughout the volume of interest.

The objectives for these early observations are as follows:

Figure 2.2: Extracted bone blocks at $t = 0, 28, 84$ for sham (row 1); ovx (row 2); and ovx+zol (row 3).

- to qualitatively describe BV/TV as a function of distance from the growth plate
- to describe changes to BV/TV over time for each experimental group, and to compare BV/TV over time between groups
- to use results from observations towards informing the development of a mechanistic model for BV/TV

2.2.1 BV/TV

BV/TV was calculated for each cross-sectional slice of the bone blocks by simply dividing the amount of bone present by the area of the bone block slice (121×121 pixels).

The mean∓standard deviation for BV/TV values are displayed for each group, at three equidistant points along the metaphysis in Table 2.1. BV/TV values asymptotically approach zero for all rats. In particular, the ovx group has very low BV/TV for later time points in metaphyseal bone furthest from the growth plate. By $t = 28$, at 4.42mm from the growth plate, some of the ovx rats have metaphyseal BV/TV values less than 1%; by $t = 56$ some of the ovx rats have BV/TV values less than 3% for metaphyseal bone beginning around 2.95mm from the growth plate; and by $t = 56$ some of the ovx rats have BV/TV values less than 1% for metaphyseal bone beginning 2.95mm from the growth plate (Table 2.1). In regions where BV/TV values fall below 5%, the BV/TV values become highly varying due to the sparseness of the bone. Accordingly, only BV/TV values above 5% were included for this preliminary work.

One of the features of BV/TV values seen in ovx+zol rats, is that by $t = 84$, some of the values at a distance 2.95mm from the growth plate are higher than the BV/TV values in the metaphyseal bone observed in the sham rats at a distance 4.42mm from the growth plate (Table 2.1). Also by $t = 84$, for the ovx+zol rats, BV/TV values at the midpoint of the data, 2.95mm from the growth plate, are generally higher than the sham rat BV/TV values, 4.42mm from the growth plate (Table 2.1).

BV/TV values $\geq 5\%$ are displayed against distance from the growth plate for all time points, for a single rat from each group in Figure 2.3 and for all rats in Figure 2.4.

2.2.2 Methods for BV/TV curve fitting

For all rats at $t = 0$, casual inspection revealed that the BV/TV as function of distance from the growth plate is nominally linear (Figure 2.4). Further inspection showed that BV/TV as a function of distance from the growth plate is nominally linear for sham and ovx rats at all time points, and for ovx+zol at $t = 0$ and $t = 14$, but that ovx+zol BV/TV curves appear to deviate significantly from linear for $t = 28, 56, 84$.

To quantify these observations, simultaneous linear regression was performed on BV/TV as a function of distance from the growth plate for all rats at all time points. Regression analysis was performed to fit polynomials of degree 1 for BV/TV as a function of distance from the growth plate for each rat r at each time point t, of the form

$$B_{r,t}(x) = mx + b. \tag{2.1}$$

To test the null hypothesis that the group slope correlation coefficients are same for first order polynomial fits for all groups at $t = 0, 14, 28, 56, 84$, t-tests were performed for correlation coefficient values between a) sham and ovx values; b) between sham and ovx+zol values; c) between ovx and ovx+zol values; and c) between the pooled sham/ovx values and ovx+zol values.

Residual analysis demonstrated that zol rat BV/TV values could not be modelled well by polynomials of degree 1 at times $t > 14$ but could be modelled well by polynomials of degree 1 for sham and ovx at all time points and for ovx+zol for $t = 0, 14$.

Further inspection indicated that the slope m in Equation 2.1 remains the same for the first degree polynomial models for sham and ovx rats at all time points, and for

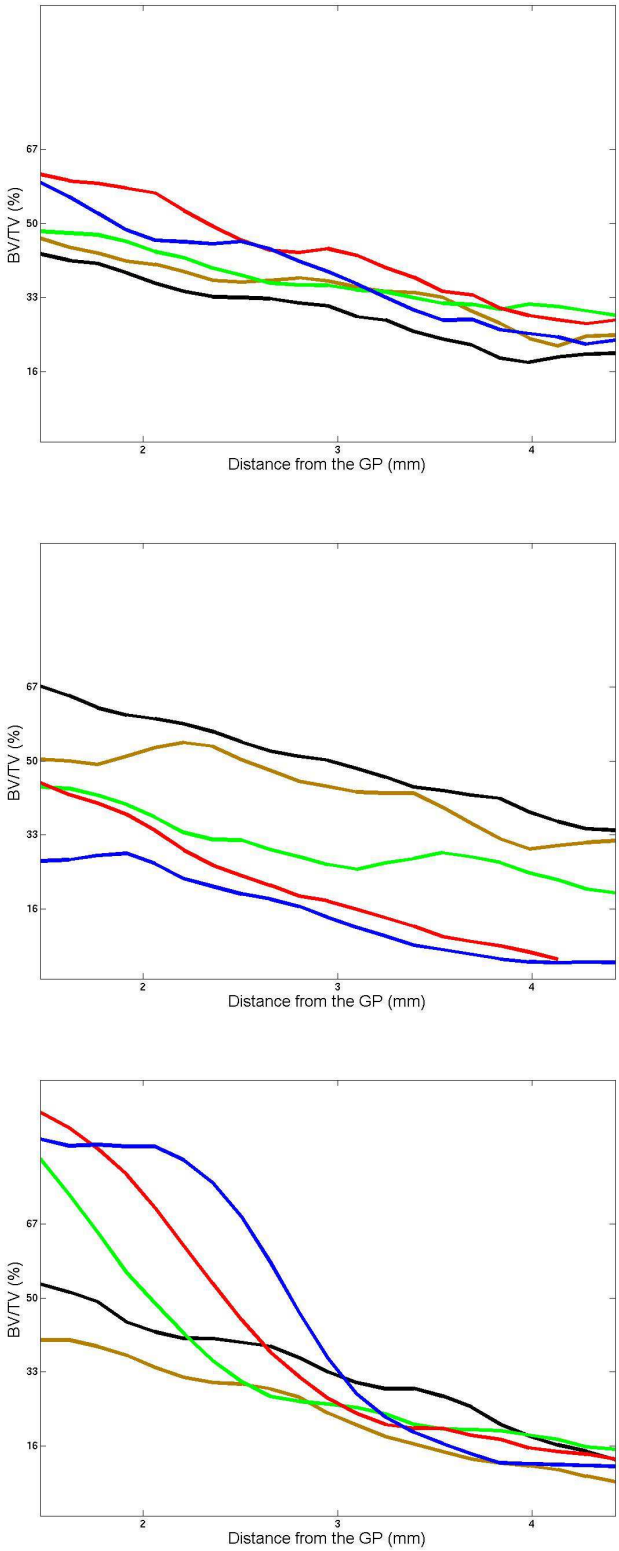

Figure 2.3: BV/TV values against distance from the growth plate (GP) in mm, for a single sham rat (left); a single ovx rat (middle); and a single ovx+zol rat (right) at times $t = 0$ (black); t= 14 (brown); $t = 28$ (green); $t = 56$ (red); and $t = 84$ (blue).

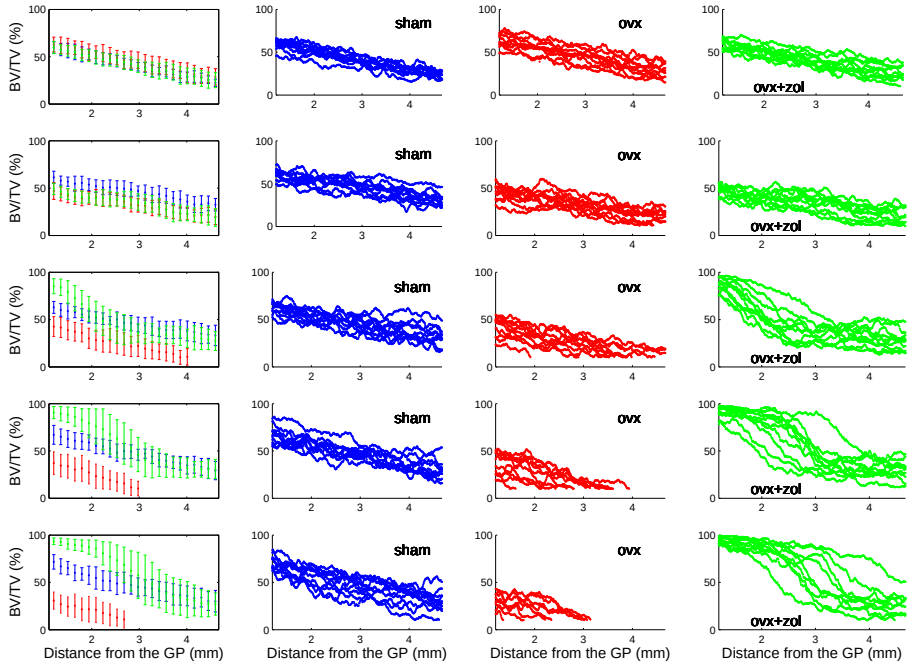

Figure 2.4: BV/TV values against distance from the growth plate (GP) in mm for all rats. Rows are according to time for $t = 0, 14, 28, 56, 84$. Columns are according to group. Column 1 includes mean $\pm$ standard deviation BV/TV values for sham (blue), ovx (red) and ovx+zol (green); column 2 includes all sham rat BV/TV values; column 3 includes all ovx rat BV/TV values; and column 4 includes all ovx+zol rat BV/TV values.

ovx+zol rats at $t = 0$ and $t = 14$. Table A.1 displays the p-values for testing the null hypothesis that the values of m remain the same between these groups and time points. A common m for all time points indicates that the gradient of the BV/TV curves remains constant over time and that the only change to the curves over time, if any, are shifts upwards/downwards by an additive constant. The common common rate of decrease, m_c, was taken to be the average rate of decrease for the above linear regression values found for Equation 2.1 over all thirty rats at $t = 0$.

2.2.2.1 sham and ovx

After finding the common rate of decrease, m_c regression was again carried out for all sham and ovx rats for a polynomial model of degree 1, with fixed m_c, and varying only b (additive constant) for each rat r at each time point t. The model for $B_{r,t}(x)$ for all sham and ovx data, is of the form

$$B_{r.t}(x) = m_c x + b_{r,t}, \tag{2.2}$$

where $b_{r,t}$ is the additive constant found for each rat r at each time point t.

Several experiments were conducted to investigate trends for $b_{r,t}$ over time for both the sham rats and the ovx groups. T-tests were performed to test the following null hypotheses:

1. For sham rats, $b_{r,t}$ values remain constant over time;
2. For ovx rats, $b_{r,t}$ values remain constant over time; and
3. There is no difference over time between sham rat $b_{r,t}$ values and ovx rat $b_{r,t}$ values.

2.2.2.2 ovx+zol

Results from the initial stage of regression analysis indicated that for the ovx+zol group, the curves that describe BV/TV as functions of distance from the growth plate are not

well modelled as polynomials of degree 1. In light of the local increase observed near the growth plate, an effort was made to quantify the non-linear ovx+zol rat BV/TV curves. Beginning at $t = 28$, the plots of BV/TV values for ovx+zol rats appear to be nonlinear close to the growth plate, but remain linear further away from the growth plate. Thus an additional model was applied to the ovx+zol BV/TV curves composing of the sum of a sigmoid and a polynomial degree 1 curve as follows,

$$B_{r,t}(x) = \frac{c}{1 + e^{\alpha(x-\beta)}} + m_c x + b_{r,t}, \tag{2.3}$$

for $t = 28, 56, 84$ where m_c is the same common slope found for all rats at $t = 0$ and $b_{r,t}$ is the additive constant associated with the linear region for each rat r at time t.

To investigate trends seen for $b_{r,t}$ t-tests were performed to test the following null hypotheses:

1. For ovx+zol rats, $b_{r,t}$ values remain constant over time;

2. There are no differences over time between $b_{r,t}$ values for ovx+zol rats and sham rats; and

3. There are no differences over time between $b_{r,t}$ values for ovx+zol rats and ovx rats.

The location of the inflection points for Equation 2.3 were identified for $t = 28, 56, 84$ in each of the ovx+zol rats. Here, the inflection point is defined as the location where the second derivative of the model for $B_{r,t}(x)$ changes sign. Linear regression was applied to the three inflection points as functions of time for each ovx+zol rat to find the average rate of change for the distance travelled by the inflection points over time for each ovx+zol rat. These results yielded an average speed for the local increase in BV/TV values that advances away from the growth plate in each of the ovx+zol rats, thus giving an indication of the rate that new bone emerges due to endochondral ossification in each rat.

2.2.3 Results

Results for testing that the correlation coefficients for the slope in Model 2.2 are the same for the sham and ovx rats and the ovx+zol rats can be found in Table 2.2. All of the slope correlation coefficients for sham and ovx rats over all time points in addition to the slope correlation coefficients for ovx+zol at $t = 0, 14$ were pooled and tested against the pooled slope correlation coefficients for a) ovx+zol rats at $t = 28, 56, 84$; b) and ovx+zol rats at $t = 56, 84$; and also tested against slope correlation coefficients for ovx+zol rats at $t = 84$. The p-values for all of these t-tests were returned as $p < 0.001$.

The common rate of decrease that was taken to be the average rate of decrease for the above regression values found for Equation 2.1 over all rats at $t = 0$, was found to be $m_c = -0.109 \pm 0.023$. Model 2.1 curves are displayed for $t = 0$ over the raw BV/TV data for all rats in Figure 2.5.

2.2.3.1 sham and ovx rats

Model 2.2 curves for a single sham rat and a single ovx rat are displayed in Figure 2.6.

The average group $b_{r,t}$ values for the sham and ovx $b_{r,t}$ values from Model 2.2 are displayed in Table 2.3. Also provided in Table 2.3 are the p-values for testing that $b_{r,t}$ values do not change over time within an experimental group, for both sham rats and ovx rats. P-values are given for testing the $b_{r,t}$ values within each group for each time-point $t \geq 14$ against the group baseline ($t = 0$) $b_{r,t}$ values. Additional p-values are displayed for testing the $b_{r,t}$ values within a group for each time-point $t \geq 28$ against the previous time point. A full list of p-values for testing $b_{r,t}$ values between all time-points within the group, for both the sham and ovx rats can be found in Table A.2 in Appendix A. In Table 2.6, p-values are also provided for testing that $b_{r,t}$ values are the same between the sham and ovx rats for each time point $t \geq 0$.

		BV/TV (%)				
	Dist (mm)	$t = 0$	$t = 14$	$t = 28$	$t = 56$	$t = 84$
sham	1.45	57.0±6.6	57.3±5.6	63.3±6.5	63.3±9.1	64.9±7.4
	2.95	40.2±4.9	47.0±6.7	47.5±7.3	47.5±5.7	45.8±9.0
	4.42	25.7±3.6	32.8±7.5	32.0±9.9	32.0±9.0	31.5±10.2
ovx	1.45	61.3±7.9	42.6±7.0	39.2±9.8	33.4±11.9	26.4±9.9
	2.95	45.3±8.8	32.1±6.8	21.3±10.6	10.5±7.8	6.8±6.3
	4.42	29.8±8.0	20.6±7.1	8.1±7.8	0.9±0.8	1.2±1.1
ovx+zol	1.45	56.6±5.8	44.5±5.4	79.8±10.4	88.6±8.0	91.5±4.7
	2.95	40.6±6.5	35.8±8.5	36.7±11.4	47.9±18.5	58.9±22.9
	4.42	26.2±8.2	20.7±8.5	29.0±10.9	30.5±9.1	27.8±13.6

Table 2.1: Mean± standard deviation BV/TV values reported in units (%) for all three groups at three equidistant points along the metaphysis, at distances 1.47mm from the growth plate (left), 2.95mm from the growth plate (middle), and 4.42mm from the growth plate (right), at $t = 0, 14, 28, 56, 84$.

Group A:	Group B		p–value
-0.101± 0.029	(a) ovx+zol $t = 28, 56, 84$	-0.201± 0.058	< 0.0001
	(b) ovx+zol $t = 56, 84$	-0.224 ± 0.052	< 0.0001
	(c) ovx+zol $t = 84$	-0.236 ± 0.055	< 0.0001

Table 2.2: Mean ± standard deviation slope correlation coefficient values for Group A: pooled ovx, sham, ovx $t \geq 0$ + pooled ovx+zol $t = 0, 14$; and Group B: pooled ovx+zol rat values for a) $t = 28, 56, 84$; b) pooled ovx+zol rat values for $t = 56, 84$; and c) ovx+zol rat values at $t = 84$. P–values are given for testing that average correlation coefficient values are the same for Group A and Group B, using student's independent t-test.

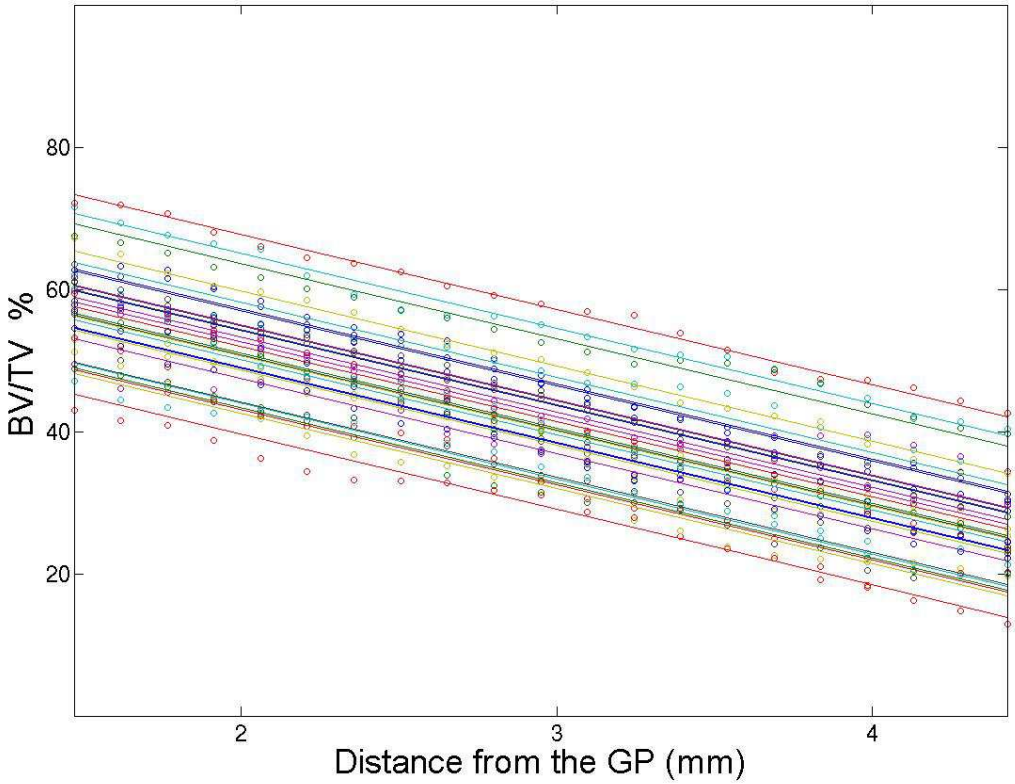

Figure 2.5: Model 2.1 curves superimposed over raw BV/TV values against distance from the growth plate, at $t = 0$, for all rats.

sham **For the sham rats, $b_{r,t}$ values generally did not change over time, however there was a slight increase in $b_{r,t}$ values at $t = 56$ ($\mathbf{p = 0.024}$) (Table 2.3).**

ovx T-test results indicate that over time, the BV/TV values for the ovx rats decrease throughout the metaphysis by an additive constant compared to the ovx rat baseline $b_{r,t}$ values. However results are less conclusive for testing the ovx $b_{r,t}$ values for any given time step $t \geq 28$ against the previous time step (Table 2.3). These results could be influenced by the fact that there was significant loss of ovx cancellous bone beginning $t = 28$ for values of x further away from the growth plate and the resulting spatial resolution was thus much lower for modelling ovx BV/TV values with Equation 2.2. There were also fewer ovx rat $b_{r,t}$ values for $t = 84$, as one of the ovx rats died before the final μCT scan.

T-test results indicate that the ovx $b_{r,t}$ values are less than the sham $b_{r,t}$ values for all $t > 0$.

2.2.3.2 ovx+zol

Model 2.2 curves for ovx+zol BV/TV values for $t = 0, 14$, and Model 2.3 curves for ovx+zol BV/TV values for $t \geq 28$ are both displayed in Figure 2.7.

Results for t-tests for ovx+zol $b_{r,t}$ values were inconclusive for both $b_{r,t}$ values over time within the ovx+zol group, and for comparison to $b_{r,t}$ values of other experimental groups. There are a few factors that may have influenced these results, including the aforementioned poor spatial and temporal resolution for ovx BV/TV data. Two ovx+zol rats also died prior to μCT scanning at $t = 84$. The advancing BV/TV increase travels so far away from the growth plate, that by $t = 84$, the spatial resolution of the ovx+zol rat BV/TV

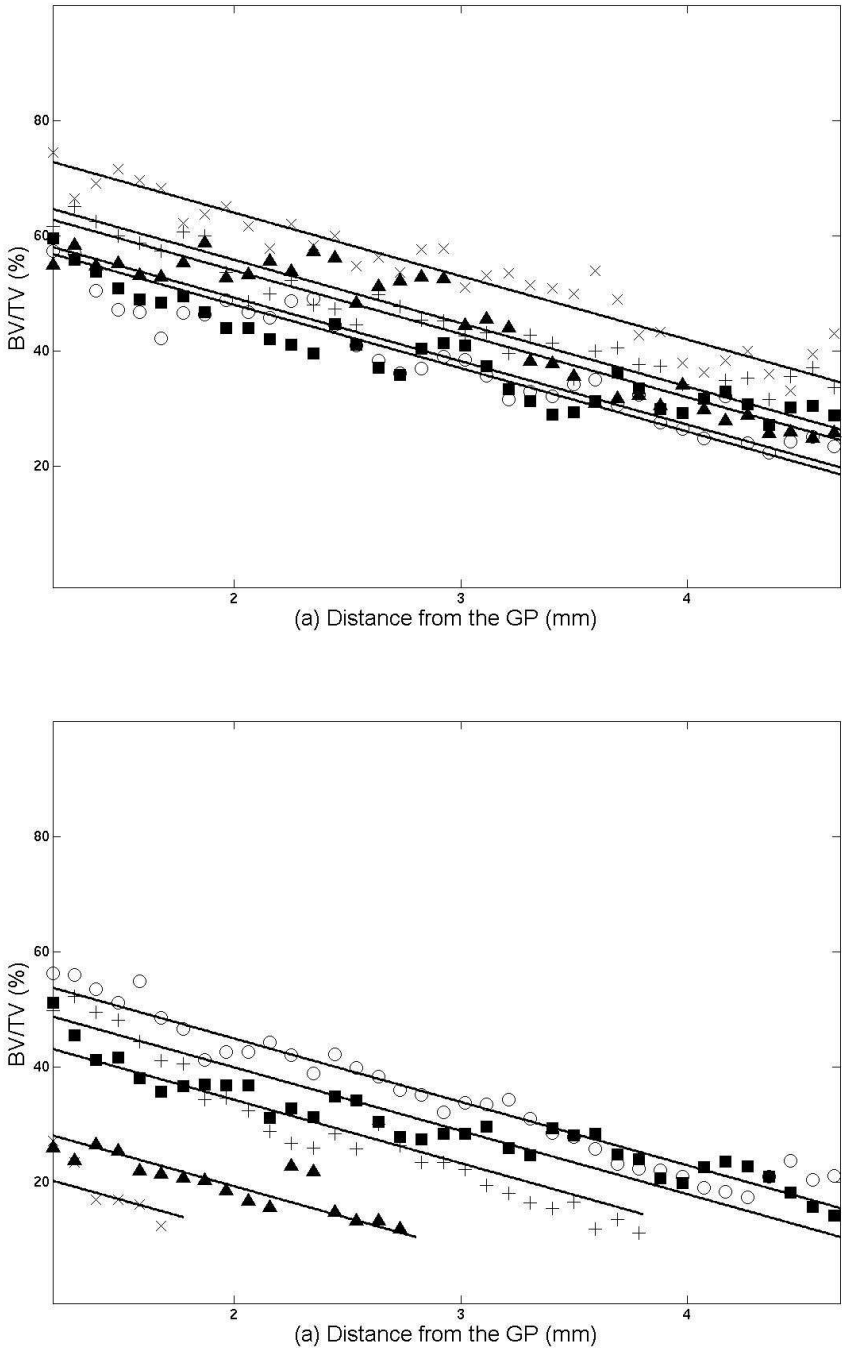

Figure 2.6: BV/TV values against distance from the growth plate for a single rat over time from the sham group (top) and from the ovx group (bottom). The raw data is shown by the markers, where $t = 0$ is represented by circles, $t = 14$ by squares, $t = 28$ by diamonds, $t = 56$ by hexagram, and $t = 84$ by upward-pointing triangles. Superimposed over the raw data are the curves modelled by Equation 2.2

	Group average additive constants $b_{r,t}$ for all time points				
	$t = 0$	$t = 14$	$t = 28$	$t = 56$	$t = 84$
	(N = 10)	(N = 10)	(N = 10)	(N = 10)	(N = 10)
sham	73.0 ± 4.8	78.1 ± 6.1	78.2 ± 7.0	79.5 ± 6.8	79.1 ± 8.6
*		*p = 0.048		*p = 0.024	
	(N = 9)	(N = 10)	(N = 10)	(N = 10)	(N = 8)
ovx	77.6 ± 8.1	64.5 ± 6.1	54.4 ±9.2	47.0 ±9.7	42.9 ± 8.6
	(N = 9)	(N = 10)	(N = 10)	(N = 10)	(N = 8)
*		*p = 0.0001	*p < 0.0001	*p < 0.0001	*p < 0.0001
**			**p = 0.016		
sham, ovx	p > 0.05	<0.001	<0.001	<0.001	<0.001

Table 2.3: Group mean ± standard deviation additive constant values $b_{r,t}$ in units (%) for Equation 2.2, for sham rats and ovx rats, for each time point, $t = 0, 14, 28, 56$; and p-values for testing the null hypothesis that group average additive constants for sham and ovx groups are the same at each time point t. Only p-values < 0.05 are reported. Longitudinal study: * indicates p-values for testing the null hypothesis that group $b_{r,t}$ values for the given time point are the same as the the group baseline ($t = 0$) $b_{r,t}$ values within the same experimental group; and ** indicates for testing the null hypothesis that $b_{r,t}$ values for a given time point within a group are the same as the group $b_{r,t}$ values found for the previous time point within the same experimental group.

data available is also significantly reduced for the polynomial degree 1 component of the Model 2.3.

The results for tracking the inflection point over time in the ovx+zol data for the Model 2.3, yielded an average speed 0.023±0.018mm/day.

2.2.4 Conclusion

The conclusion of the preliminary study is that changes to BV/TV act consistently over the region studied, in that decreases could be modelled well as being constant as functions of distance from the growth plate for sham rats and ovx rats for $t \geq 0$ and for ovx+zol rats for $t \leq 14$. For $t > 14$, the ovx+zol rats display changes in BV/TV values that are not constant as functions from the growth plate. Thus the effect of treatment by zoledronic acid is not consistent as a function of distance from the growth plate. This observation motivated the modelling in Chapter 3.

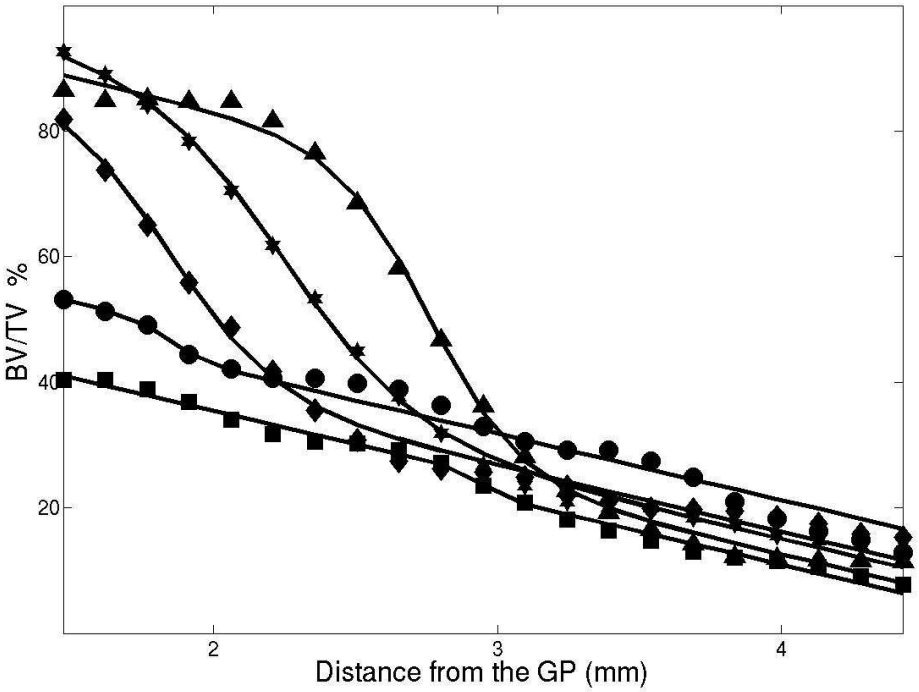

Figure 2.7: Model 2.3 curves superimposed over raw BV/TV values against distance from the growth plate over time, for a single ovx +zol rat. The raw data is shown by the markers, where $t = 0$ is represented by circles, $t = 14$ by squares, $t = 28$ by diamonds, $t = 56$ by hexagram, and $t = 84$ by upward-pointing triangles. Superimposed over the raw data are the curves modelled by Equation 2.2 for $t = 0, 14$ and by Equation 2.3 for $t \geq 28$.

Chapter 3

Mathematical model for BV/TV

A mathematical model is presented to describe the changes to BV/TV over distance relative to the growth plate that occur over 84 days in juvenile rats from the sham, ovx and ovx+zol groups. In this study a PDE spatial extension is applied to the temporal ODE model developed by Fazzalari *et al.* (2012).

3.1 Prior work

The model developed by Fazzalari *et al.* (2012) characterises the effects of remodelling processes on the local volume and structure of cancellous bone.

The model comprises a temporal ordinary differential equation for BV/TV over time coupled with simulations of individual remodelling events. The model was validated on a smaller volume of interest, taken from the experimental data described in Chapter 2. The region of experimental data chosen for this work extends from 1.2mm below the growth plate to 2mm below the growth plate. The simplest form of the model is

$$\frac{dB}{dt} = c(B)\left(f(B) - R\right) \tag{3.1}$$

where $c(B)$ is the number of remodelling events per unit time, $f(B)$ is the formation volume per remodelling event and R is the resorption volume per remodelling event. For

the region of experimental data selected in this study the surface area is proportional to $B^{2/3}$, allowing surface area to be modelled as a function of BV/TV, thus 18 models were considered for $c(B)$ and $f(B)$ each being linearly dependent on BV/TV, surface area or being independent of the amount of bone present. Only models that predict convergence of $B(t)$ to finite positive values were considered, reducing the 18 models to 3 which are described in Appendix 3.1.

The results for sham and ovx were in agreement with the current understanding of bone remodelling in adult rats. However, results for ovx+zol indicated that the changes seen in the cancellous bone could not be described by remodelling alone in bisphosphonate treated juvenile rats. This observation motivated the development of the spatio-temporal PDE model that was constructed for this study. BV/TV will now be viewed as dependent on both time and the location relative to the growth plate.

3.2 Spatial extension

For simplicity, and for the purpose of modelling, let the growing bone be viewed as 'emerging during growth' and then continuing to 'travel away from the growth plate'. Also, suppose that the only changes to BV/TV over time, are due to remodelling events with coupled bone resorption and formation at the BMU level. Now, let $B(x,t)$ represent the amount of bone, BV/TV, at some position x relative to the growth plate, at time t. As in Equation 3.1, let R represent average resorption volume per remodelling event with units ($\text{mm}^3\text{day}^{-1}$); $f(B(x,t))$ represent average formation volume per remodelling event, viewed as an unknown function of $B(x,t)$, with units ($\text{mm}^3\text{event}^{-1}$); let $c(B(x,t))$ represent the number of remodelling events per unit BV/TV per unit time, also viewed as an unknown function of $B(x,t)$ with units (events $\text{mm}^{-3}\text{day}^{-1}$); and let v be a constant velocity with which bone 'emerges' during growth.

Over time increment Δt, bone moves away from the growth plate with velocity v, at a distance $x = v\Delta t$. Bone previously at position x moves away from this location and so represents a loss of bone with BV/TV $B(x,t)$. Bone previously at position $x - \Delta x$

moves to position x during time increment Δt, and also undergoes remodelling according to Equation 3.1 during time increment Δt. Thus the new bone at position (x, t) has BV/TV given by

$$B(x - \Delta x, t) + c(B(x - \Delta x, t)\,[f(B(x - \Delta x, t) - R]\,\Delta t.$$

Hence the net change in BV/TV at x is given by

$$\Delta B = -B(x, t) + B(x - \Delta x, t) + c(B(x - \Delta x, t)\,[f(B(x - \Delta x, t) - R]\,\Delta t$$

The time difference quotient is

$$\frac{\Delta B}{\Delta t} = \frac{B(x - \Delta x, t) - B(x, t)}{\Delta t} + c(B(x - \Delta x, t)\,[f(B(x - \Delta x, t) - R]\,.$$

Since $\Delta x = v\Delta t$,

$$\frac{\Delta B}{\Delta t} = -v\frac{B(x - \Delta x, t) - B(x, t)}{\Delta x} + c(B(x - \Delta x, t)\,[f(B(x - \Delta x, t) - R]$$

Taking $\lim_{\Delta t \to 0}$, and thus $\lim_{\Delta x \to 0}$, yields

$$\frac{\partial B(x, t)}{\partial t} = -v\frac{\partial B(x, t)}{\partial x} + c(B(x, t)\,[f(B(x, t) - R]\,.$$

In reduced notation, the simplest form of the model becomes

$$B_t + vB_x = c(B)\,(f(B) - R)\,, \tag{3.2}$$

where the change in BV/TV per unit time at a distance x relative to the growth plate is given by the difference between the average formation volume and the average resorption volume during a single remodelling event, multiplied by the number of active remodelling sites per unit time per unit bone volume.

With the same criterion as in section 3.1, only three models that predict $B(x,t)$ to converge to a finite positive value for fixed t were considered further, again reducing the number of possible models to three, presented in section B. Here, bone remodelling is considered to be *random remodelling*, as experimental conditions did not change over time (Appendix A).

3.3 Model for BV/TV

Since the three models investigated by Fazzalari *et al.* (2012) yielded results with the same trends in effects of ovx and ovx+zol on modelling parameters $f(B)$, R, and $c(B)$, Model B.4 (Appendix 3.1) was chosen on the basis of being the simplest both mathematically and in terms of physical interpretation, where $f(B) = \dfrac{F}{c(B)}$, $c(B) = C(t)B(t)$.

There are two main goals considered in the development of a simple, mechanistic model for BV/TV. The first goal is to test the hypothesis that the effect on coupled bone remodelling due to both ovx and ovx+zol is to alter the cycle rate. The second goal is to test the hypothesis that there is an additional effect of ovx+zol, to alter processes that occur outside the domain of the experimental data.

The model for BV/TV, B.4 is

$$\frac{1}{v}B_t + B_x = \frac{1}{v}(F - C(t)RB(t)) \tag{3.3}$$

$$B(0,t) = D(t). \tag{3.4}$$

3.3.1 Initial conditions, s

The model allows $x = 0$ to be viewed as the 'effective point of formation', modelled as an unknown location between the chondro-osseous junction at the growth plate and the metaphyseal bone to the left of the window of experimental data. The initial condition

for $x = 0$ is considered to be the location where coupled bone resorption and formation remodelling processes begin in emerging bone. Thus coupled remodelling occurs in bone $x \geq 0$ and continues as the bone travels away from the growth plate. The effective point of formation is included in the numerical implementation of the model as parameter s. The parameter s for the effective point of formation is difficult to define and may span over a small region, where this region may change slightly over time and may be different for any given rat. To address this uncertainty, an additional parameter is introduced during the optimisation process (Section 4.1.4.2).

3.3.2 Cycle rate, $c(B)$

A well known effect of oestrogen deficiency on bone remodelling in adult rats, is an increase in the rate of remodelling (Section 1.1.3). This effect was observed in prior work. Results from Fazzalari *et al.* (2012) suggest that one of the effects of ovx is an increase in $c(B)$ compared to the sham group. Also well known, is that the dominant effect of bisphosphonates on bone remodelling is a reduction in the rate of remodelling due to inhibition of osteoclast resorption (Section 1.1.4.1).

To test that the effect of the ovx and ovx+zol in growing rats is to alter the cycle rate, a sigmoidal function is introduced in Equation 3.5) to model the change in proportionality term $C(t)$ as a function of time according to effects of ovx, and ovx+zol. $C(t)$ models C_1 for for all rats prior to the $t = 0$ ovariectomy and for sham rats for all time; C_2 for the effect of the $t = 0$ ovariectomy in ovx and zol rats; and C_3 for the effect of bisphosphonate treatments in zol rats for $t \geq 14$.

$$C(t) = \frac{C_1 + C_3}{2} + \frac{C_2 - C_1}{2} \tanh\left(\lambda_1(t - J_1)\right) + \frac{C_3 - C_2}{2} \tanh\left(\lambda_2(t - J_2)\right), \tag{3.5}$$

where λ_1 adjusts the rate at which the effect of the ovariectomy on cycle rate manifests, and J_1 is the time lag of this effect. λ_2 adjusts the rate at which the effect of the bisphosphonate on cycle rate manifests, and J_2 is the time lag of this effect.

3.3.3 Boundary conditions, $D(t)$

Results from Fazzalari *et al.* (2012) showed that the changes to cancellous bone in the metaphysis in growing juvenile rats could not be modelled by remodelling processes alone. Preliminary observations made in this study (Section 2.2.3.2), also indicated that BV/TV increases significantly locally near the growth plate, compared to BV/TV observations throughout the metaphysis further away from the growth plate.

To allow for the possibility of an additional effect of ovx+zol on BV/TV local to the growth plate that cannot be explained by coupled remodelling, boundary conditions, $D(t)$, are introduced in Equation 3.6.

$$D(t) \quad = \quad \frac{D_2 + D_1}{2} + \frac{D_2 - D_1}{2} \tanh\left(\eta(t - K)\right). \tag{3.6}$$

Equation 3.6 describes the observed change in BV/TV at the left edge of the experimental data window, in bone emerging from the growth plate. For sham and ovx rats, BV/TV at the boundary is modelled as constant, with parameter D_1. For the ovx+zol rats, a sigmoidal function is presented to model the change in the BV/TV as a function of time, allowing for BV/TV to shift from D_1, and asymptotically approach a second constant, D_2. Parameter η adjusts the rate at which the effect of ovx+zol on emerging BV/TV manifests, and K is the time lag of this effect.

3.4 Bone blocks

Figure 3.1 gives a rough indication of the location where the bone blocks were extracted from in the proximal tibial cancellous bone, with initial conditions, s. The medial axis of the tibia is represented along the horizontal axis of the figure. For display purposes, the figure is shown in two dimensions, however the bone blocks have volume $1 \times 1 \times 3.5\text{mm}^3$,

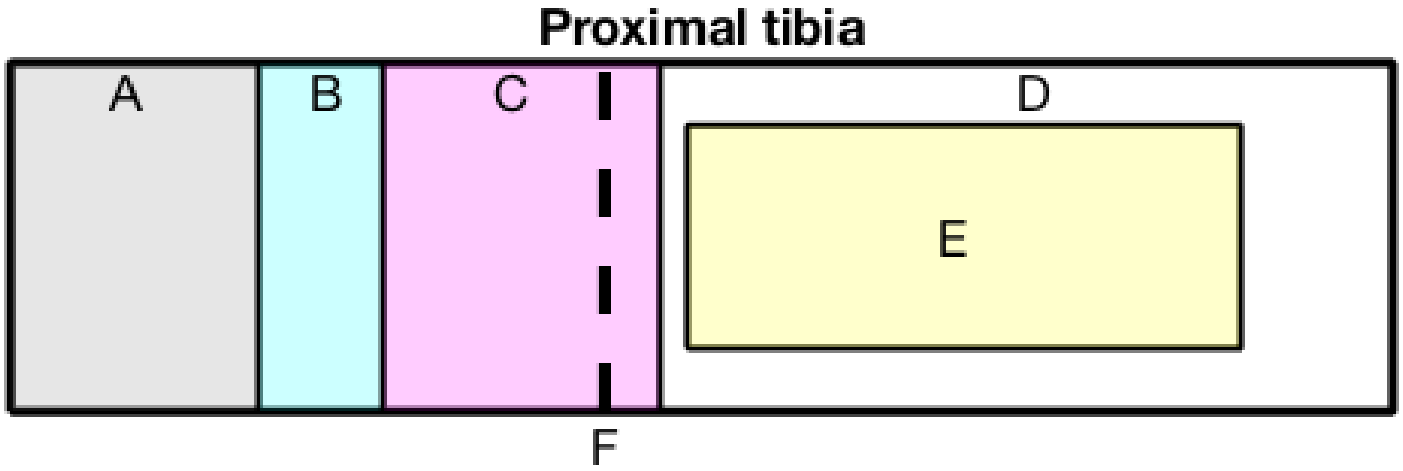

Figure 3.1: Location of experimental μCT bone block (yellow) in the proximal end of the tibia. A (grey): epiphysis, B (cyan): growth plate, C (magenta): primary spongiosa, D (white): secondary spongiosa, E (yellow): bone block extending 1.2mm-4.7mm from the edge of the growth plate, shown in two dimensions, $1 \times 3.5\text{mm}^2$, F: initial conditions, s ($x = 0$) viewed as being at an unknown location prior to parameter optimisation. Figure is not shown to scale.

3.5 Analytic solution for $B(x,t)$

The following constants are introduced to reduce the notation

$$A = \frac{F}{v},\ \ P = \frac{R(C_1+C_3)}{2v},\ \ Q_1 = \frac{R(C_2-C_1)}{2v},\ \ Q_2 = \frac{R(C_3-C_2)}{2v}.$$

The PDE becomes

$$\begin{aligned} \frac{1}{v}B_t + B_x &= A - PB - Q_1 \tanh\left(\lambda_1(t-J_1)\right)B \\ &\quad -Q\tanh\left(\lambda_2(t-J_2)\right)B, \end{aligned} \tag{3.7}$$

$$B(0,t) = D(t) \tag{3.8}$$

The full derivation and notation can be found in section B.2.

A full analytic solution to Equation 3.7 is given by

$$\begin{aligned} B(x,t) = D(t-{}^{x}\!/_{v})e^{-Px}&\left(\frac{e^{\lambda_1(t-{}^{x}\!/_{v}-J_1)}+e^{-\lambda_1(t-{}^{x}\!/_{v}-J_1)}}{e^{\lambda_1(t-J_1)}+e^{-\lambda_1(t-J_1)}}\right)^{Q_1 v/\lambda_1} \\ &\times\left(\frac{e^{\lambda_2(t-{}^{x}\!/_{v}-J_2)}+e^{-\lambda_2(t-{}^{x}\!/_{v}-J_2)}}{e^{\lambda_2(t-J_2)}+e^{-\lambda_2(t-J_2)}}\right)^{Q_2 v/\lambda_2} + \\ &+\frac{Ave^{-Pvt}\int_r^{s/v+r}e^{Pvy}\left(e^{\lambda_1(y-J_1)}+e^{-\lambda_1(y-J_1)}\right)^{Q_1 v/\lambda_1}\left(e^{\lambda_2(y-J_2)}+e^{-\lambda_2(y-J_2)}\right)^{Q_2 v/\lambda_2}dy}{\left(e^{\lambda_1(t-J_1)}+e^{-\lambda_1(t-J_1)}\right)^{Q_1 v/\lambda_1}\left(e^{\lambda_2(t-J_2)}+e^{-\lambda_2(t-J_2)}\right)^{Q_2 v/\lambda_2}}. \end{aligned} \tag{3.9}$$

For ovx rats

$Q_2 = \dfrac{R(C_3-C_2)}{2v} = 0$ since $C_2 = C_3$; and

$D(t) = \dfrac{D_2+D_1}{2} + \dfrac{D_2-D_1}{2}\tanh\left(\eta(t-K)\right) = D_1$ since $D_1 = D_2$ thus

$$B(x,t) = D_1 e^{-Px}\left(\frac{e^{\lambda_1(t-x/v-J_1)}+e^{-\lambda_1(t-x/v-J_1)}}{e^{\lambda_1(t-J_1)}+e^{-\lambda_1(t-J_1)}}\right)^{Q_1 v/\lambda_1} + \frac{Ave^{-Pvt}\int_r^{s/v+r} e^{Pvy}\left(e^{\lambda_1(y-J_1)}+e^{-\lambda_1(y-J_1)}\right)^{Q_1 v/\lambda_1} dy}{\left(e^{\lambda_1(t-J_1)}+e^{-\lambda_1(t-J_1)}\right)^{Q_1 v/\lambda_1}}. \tag{3.10}$$

For sham rats

$Q_1 = \dfrac{R(C_2 - C_1)}{2v} = 0$ since $C_1 = C_2$;

As above, $Q_2 = \dfrac{R(C_3 - C_2)}{2v} = 0$ since $C_2 = C_3$; and

$D(t) = \dfrac{D_2 + D_1}{2} + \dfrac{D_2 - D_1}{2}\tanh\left(\eta(t-K)\right) = D_1$ since $D_1 = D_2$.

$B(x,t) = D_1 e^{-Px} + \dfrac{A}{P}(1 - e^{-Px})$, hence

$$B(x,t) = (D_1 - \frac{F}{C_1 R})e^{-C_1 Rx/v} + \frac{F}{C_1 R}. \tag{3.11}$$

Chapter 4

Methods

Optimisation methods were implemented to arrive at a set of values for model parameters that best describe observed BV/TV in the experimental data. The model parameter values were identified by minimising the error between BV/TV values in the experimental data and BV/TV values predicted by the mathematical model for BV/TV.

The model in Equation 3.7 includes N = 13 parameters to be estimated from the data. Due to the great variation between rats and the noise in the measured values of the amount of bone as a function of distance from the growth plate for individual rats, the difference between the data and model as a function of the parameters is fraught with local minima. Accordingly, descent methods for minimising the fit over the parameters space was not possible. Instead, an optimal fit was sought in stages. Initial plausible ranges for the parameters were set based on inspection and physical constraints. Next, the parameters controlling the gross features of the model were fit. In subsequent stages, more parameters were added and ranges of parameters were refined. Exhaustive search over parameter sets limited to discrete values of the parameters within a fixed ranges was used at each step.

Statistical analysis was also carried out to investigate the effects of ovx and ovx+zol on the cycle rate, and to investigate the effects of ovx+zol on boundary conditions.

4.1 Optimisation methods

Optimisation of the model parameters was an iterative process and was carried out in three stages. First the search window for model parameter ranges was narrowed using exhaustive search methods with an initial estimate for initial conditions, s. Exhaustive search has the advantage over other optimisation routines that absolute minima are guaranteed to be found. However, the precision is limited by the level of discretisation of the parameter space.

Secondly, fixed resolution optimisation methods were implemented over a range of values of s, to identify a single value of s for all rats. Finally, once a value was determined for s, fixed resolution methods were again implemented over the entire model parameter space. An additional parameter was introduced to allow for small spatial shifts, ss, in an effort to treat uncertainty relating to variability in the data. Parameter ss was found for each rat and each time point, by using exhaustive search methods in a sub-routine of the fixed resolution optimisation algorithm.

4.1.1 Integral in solution for $B(x,t)$

The integral term in the solution for $B(x,t)$ for both ovx and ovx+zol rats is of the form $\frac{1}{f(t)} \int_{t-x_0/v}^{t} f(y)dy$, where f denotes the integrand. For each time point $t = 0, 14, 28, 56, 84$ that $B(x,t)$ is calculated over x during optimisation, the integral is calculated using the quad command in Matlab in the first instance for $B(0,t)$ over the interval $[t - \frac{x_0}{v}, t]$, where $x_0 = 0$ (initial conditions, s). After the integral is calculated for x_0 , the trapezoidal rule is used to approximate the integral by way of the integrand over the interval $[t - \frac{x_i}{v}, t - \frac{x_i + dx}{v}]$, for each of the remaining 399 slices, x_1,x_2, ..., x_{399}. Each slice is separated by $dx = x_{i+1} - x_i = 0.0087$mm.

4.1.2 Error function

The error function f for rat r and time-point t for the model is given by $f_{r,t}(P)$, where $P = (p_1, p_2, ..., p_N)$ is the vector of N parameters. Here,

$$f_{r,t}(P) = \sqrt{\frac{1}{m}\sum_{i=1}^{m}(B_r(x_i,t) - M(x_i,t))^2},$$

where $B(x_i, t)$ is the BV/TV value determined by the model, computed at slice i and time t; and $M(x_i, t)$ is the measured BV/TV value in the experimental bone block data at slice i and time t. This formula records the root mean squared error at x_i and time t averaged over the number of slices used in the function evaluation. The total error for rat r is $f_r = \text{mean}_t(f_{r,t})$ where mean_t depends on the number of time-points used or available for rat r. The total error reported for a group is $f = \text{mean}_t(f_r)$, where mean_r depends on the number of rats used or available for a group.

4.1.3 Initial parameter estimation

There are 13 parameters in the model for BV/TV, for which reasonable ranges had to be identified prior to optimisation.

4.1.3.1 Bone growth rate, v

The initial estimate for v was 0.023mm/day, found from preliminary work carried out in Section 2.2.3.2. This estimate was based on the distance that the inflection points in Equation 2.3 were found to travel over time for ovx+zol rats beginning $t = 28$. Efforts to quantify the sigmoidal plus linear shape were difficult given the variability between individual rats, noisy data and very small sample sizes. Subsequently, v was included in the optimisation scheme with the other parameters.

4.1.3.2 Model parameters R and $C(t)$

Average resorption volume, R, could vary between groups and change according to experimental conditions. However, R only appears in the analytic solution for $B(x,t)$ as a product with the proportionality constant terms in $C(t)$. R appears in the model as $S_1 = C_1R$, $S_2 = C_2R$, and $S_3 = C_3R$. Thus R could not be determined individually. Similarly, proportionality terms C_1, C_2, C_3 in Equation 3.5 only appear in the solution for $B(x,t)$ as products with R and could not be determined individually. Optimising these parameters requires knowledge of them separately. Parameters S_1, S_2, and S_3 were used as surrogates for studying the trends in the proportionality term $C(t)$ for cycle rate, $c(B)$, under the assumption that differences in R were small across the three cohorts.

4.1.3.3 Narrowing parameter ranges

Exhaustive search methods were used to narrow the ranges for the parameters, beginning with fitting the model to the sham rat data. The solution for sham rats (Section 3.5) has three degrees of freedom, for fixed v. At most only three parameters could be deduced from the experimental data,including $D1$, $\frac{F}{S_1}$ where $S_1 = C_1R$, and $\frac{S_1}{v}$. Preliminary experiments narrowed these parameter ranges as follows: $\frac{S_1}{v} \in [0.01, 0.50]$, $D_1 \in [0.5, 0.8]$, $\frac{F_1}{S_1} \in (0, 0.02)$, and $v \in [0.02, 0.04]$.

Further experiments were performed to find reasonable ranges for parameters for ovx and ovx+zol rats, by fixing most parameters and allowing 3-5 parameters to vary at time, over 5-10 values each. For a given parameter, the range was set over an exponential scale, and new ranges were chosen according to the location of the current optimal value that yielded the lowest error between the solution for $B(x,t)$ and the BV/TV of the data. If an optimal value fell on one of the boundaries of the parameter range, the new range was reduced with the current optimal value in the centre of the range.

At this early stage of optimisation, some of the parameters were fixed. The effective point of formation was fixed at $s = 0.5$. The time shift parameter J_1 in Equation 3.5 was set to zero, with the simplified assumption that any changes to cycle rate due to ovx occur

on the same day of the ovx surgery. Similarly, the time shift parameters J_2 in Equation 3.5 and K in Equation 3.6 were set to day 14, the same day that the zol treatments begin, implying that any effects of ovx+zol on cycle rate or change in BV/TV near the growth plate begin immediately after commencement of zoledronic acid treatment. A set of initial parameter ranges was established and can be seen in Table 4.1.

Parameter	Range	Units
v	$[0.02, 0.04]$	mm/day
D_1	$[0.5, 0.8]$	dimensionless
D_2	$[0.7, 0.95]$	dimensionless
η	0.1	dimensionless
K	14	days
S_1	$[0.007, 0.009]$	events/day
S_2	$[0.01, 0.03]$	events/day
S_3	$[0.001, 0.1] \times 10^{-7}$	events/day
λ_1	$[0.01, 3]$	dimensionless
λ_2	$[0.01, 3]$	dimensionless
J_1	0	days
J_2	14	days
F	$[0.0000001, 0.0000002]$	dimensionless

Table 4.1: Parameter ranges

4.1.4 Fixed resolution optimisation

Fixed resolution optimisation was carried out after the above parameter estimation experiments, to find parameter ranges that were reasonable, but wide. The dimension of the parameter spaces is too large for exhaustive search methods. Also, this allowed for setting windows of parameters instead of discrete values and reduces the number of function calls compared to the exhaustive search methods.

For a given rat the optimisation routine was applied to identify the optimal set of N parameters in the model for BV/TV that best match the data over all time points.The full list of $N = 13$ model parameters are v, S_1, S_2, S_3, $D_1 D_2, \lambda_1, \lambda_2, \eta, J_1, J_2$, and K.

During the fixed resolution optimisation, to minimise the error function, the error function was evaluated at $2N$ locations corresponding to one step in each of the $2N$ directions parallel to the N coordinate axes. In addition, a search is also carried out in the direction of the gradient of f to find the best neighbouring voxel (within the domain).

4.1.4.1 Inclusion of spatial shifts, ss

Additional spatial shifts, ss, are included in the model to account for the inexact knowledge of aspects of the data including the location of the growth plate, the natural variation in bone metabolism over time, the location of the effective point of formation, as well as the timing of the surgeries, injections and μCT scans. During the optimisation process the data are shifted relative to the solution in order to minimise the error function f over the existing variables for a given rat, allowing different shifts for each time point.

4.1.4.2 Fixed resolution optimisation routine

1. An initial point is set randomly from the domain of allowable values, for N parameters. Here N is the number of parameters in the model. For sham rats $N = 4$, for ovx rats $N = 7$, and for ovx+zol rats $N = 13$.

2. For a given direction of search, $p = (p_1, p_2, ..., p_N)$, the error function f is computed at the $2N$ points given by $p + e_i$ and $p - e_i$ for $i = 1, 2, ..., N$, where e_i is the same dimension as p with zeros everywhere except a 1 in position i, $e = (0, 0, ...1, ..., 0)$.

3. The error function f is evaluated at a discrete form of the gradient, with the partial derivative in direction i computed as $d_i = \dfrac{f(p + e_i) - f(p - e_i)}{2}$ and f is evaluated at $q_i = p + e_i \ \forall i$.

4. If $\min(f(q_i)) < f(p)$, then the search moves to q_i where $I = \text{argmin}(f(q_i))$. If $f(q_i)$ has not been computed previously, steps 1-3 are applied with $p = q_i$. If $f(q_i)$ has been computed previously, then there is no point in applying the algorithm again at this point and so a new point in the parameter space is chosen randomly and steps 1-3 are applied at this new point.

5. The optimisation routine stops if a functional value of zero is found, a preset number of function calls is reached, or a preset number of iterations is performed.

ss **shift optimisation** The optimisation strategy for the data shifts is different to the fixed resolution optimisation for the 13 parameters. At each step at which the error function is evaluated at the 13 parameters, an additional exhaustive search is performed over an interval of possible relative shifts between the data and the model for $B(x,t)$. Exhaustive search methods were implemented rather than fixed resolution to minimise unnecessary computation of $B(x,t)$. Instead of comparing the data to the model shifted by an amount SS by way of computing $B(x-SS,t)$, this strategy takes into account the shifts without excessive additional computations, since $B(x-SS,t)$ is the same as $B(x,t)$ shifted by SS.

4.1.4.3 Experiment for initial conditions, s

Parameter ranges in Table 4.1 were used for carrying out fixed resolution optimisation of model parameters over a range of values for s. In addition to fixed resolution optimisation of the 10 model parameters, an exhaustive search was performed over an interval of relative spatial shifts between the data and the model, for each rat and time point.

4.1.4.4 Experiment for optimal model parameters

After determining a single value for s, a final experiment was set up over the entire parameter space for all 13 model parameters, and over an interval of spatial shifts. The range of parameters are shown in Table 4.1. At this final stage of optimisation J_1, J_2 and K were allowed to vary up to 4 days from the time of surgery/injections.

4.2 Statistical testing

Statistical methods were implemented to investigate the effects of ovx and ovx+zol on BV/TV, and to examine the appropriateness of ss, the parameter included as a means of addressing noise and uncertainty in the experimental data.

1. To test the hypothesis that the distributions of the shift parameter, ss, are the same between groups, t-tests were performed between each group.

2. To test the null hypothesis that the cycle rate remains the same over time for all groups, t-tests were conducted to compare cycle rate parameters S_1, S_2, and S_3.

3. To test the hypothesis that boundary conditions for ovx+zol rats are the same compared to boundary conditions for the other groups, a t-test was performed to compare boundary condition parameters D_1 and D_2.

Chapter 5

Results

The results are presented for implementation of the methods described in Chapter 4. Optimisation was carried out for identifying values and trends of the model parameters from the model for BV/TV, $B(x,t)$, which was developed in Chapter 3. Statistical testing was conducted to investigate the dominant effects of ovariectomy surgery and zoledronic acid treatments on cancellous BV/TV in juvenile rats.

5.1 Initial conditions, s

Optimisation was carried out over ten $B(x,t)$ model parameters with three of the model parameters fixed, $J_1 = 0$, $J_2 = 14$ and $K = 14$, for a range of values of s, the effective point of formation. Parameter s is viewed as the location where coupled bone remodelling begins. Values of s that were considered, range from $s = 0$ where $x = 0$ is viewed as being at the growth plate, to $s = 1.2$ with $x = 0$ viewed as being at the left edge of the experimental data window.

Examples of model fits for s too close to the growth plate at $s = 0.1$ are provided in Appendix C. Model fits are shown for all three groups in Figures C.1-C.3. The distribution of optimised model parameters for $s = 0.1$ are displayed in Figure C.4.

The value of s that minimised the error function, and also produced the best fits visually for BV/TV across the groups was found to be $s = 0.8$, in the vicinity of bone where primary spongiosa transitions to secondary spongiosa.

5.2 Modelling results

The final window of parameter ranges used for fixed resolution optimisation are presented in Table 4.1. For every rat in every group, the optimal set of parameters that minimised the error function comparing the model for BV/TV to the experimental data were recorded and can be found in Appendix C, in Tables C.1- C.3. These values are presented in Table 5.2 as the mean± standard deviation across all rats that share common parameters in the solution for $B(x,t)$. Sham and ovx $B(x,t)$ solutions include a subset of the total $N = 13$ parameters, and ovx+zol solutions include all 13 parameters.

Model parameters for each group:

- sham: v, D_1, S_1, F $(N = 4)$
- ovx: $v, D_1, S_1, F, S_2, \lambda_1 J_1$ $(N = 7)$
- ovx+zol:$v, D_1, S_1, F, S_2, \lambda_1 J_1, S_3, \lambda_2, J_2, D_2, \eta, K$ $(N = 13)$

The fits for $B(x,t)$ to the experimental data BV/TV are displayed for each rat in Figure 5.1 (sham), Figure 5.1 (ovx) and Figure 5.3. The distribution of optimal model parameters for each of the 13 parameters are displayed in Figures 5.4 - 5.6. Figure 5.4 shows the distribution of parameter values for parameters that appear in the solution for $B(x,t)$ across all of the groups; Figure 5.5 shows the distribution of parameters relating to the effect of ovariectomy on cycle rate which appear in the solution of $B(x,t)$ for both ovx and ovx+zol rats; and Figure 5.4 shows the distribution of parameter values for paramters relating to the effect of zoledronic acid on cycle rate and boundary conditions, which appear in the solution for $B(x,t)$ for ovx+zol rats only.

Parameter	a	b
v	0.0200	0.0380
S_1	0.0065	0.0085
S_2	0.0200	0.0400
S_3	10^{-5}	10^{-2}
D_1	0.5500	0.9500
D_2	0.7500	0.9700
λ_1	0.0100	2
λ_2	0.0100	3
η	0.0200	0.2000
J_1	0	2
J_2	14	18
K	14	18
F	10^{-13}	10^{-10}

Table 5.1: Parameter ranges for final stage of optimisation, $[a, b]$.

Growth rate The average growth rate over all 26 rats was $v = 0.034 \pm 0.004$.

Spatial shift, ss The values for the spatial shift parameter, ss, were recorded for each rat, according to group (Appendix C) and the distributions are displayed in Figure 5.7.

	All rats	Effect of ovariectomy	Effect of bisphosphonates	
	sham,ovx,ovx+zol	ovx,ovx+zol	ovx+zol	
	n = 26	n = 16	n = 9	
Parameters				
v	0.0338 ± 0.0044			
S_1	0.0073 ± 0.0009			
D_1	0.6885 ± 0.0846			
F	2.7394 ± 4.4988			$\times 10^{-11}$
S_2		0.0331 ± 0.0072		
λ_1		1.0465 ± 0.8871		
J_1		0.1923 ± 0.5670		
S_3			0.0025 ± 0.009	
λ_2			0.6375 ± 0.8859	
J_2			17.3333 ± 1.4142	
D_2			0.9456 ± 0.0367	
η			0.0844 ± 0.0371	
K			16.8889 ± 1.7638	

Table 5.2: Mean±standard deviation of optimal parameter values. n is the number of animals in the indicated groups.

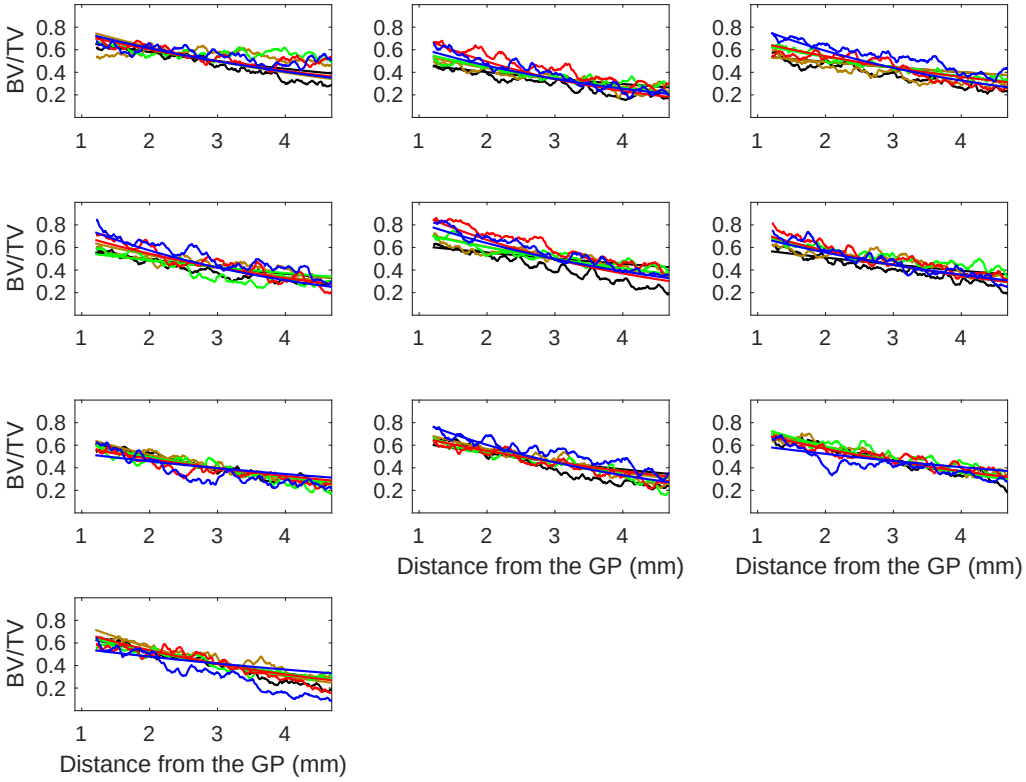

Figure 5.1: Model for $B(x,t)$ for sham rats. Each figure shows the BV/TV values against distance from the growth plate for each $t = 0$ (black), $t = 14$ (brown), $t = 28$ (green), $t = 56$ (red), and $t = 84$ (blue) for an individual rat from the sham group plus the model for $B(x,t)$ superimposed according to the same colour scheme. The model for the sham group does not change as a function of time, however the curves vary over the five time points due to slight variations in the optimised values for shift parameter, ss. Overall group error for fits is 0.0362.

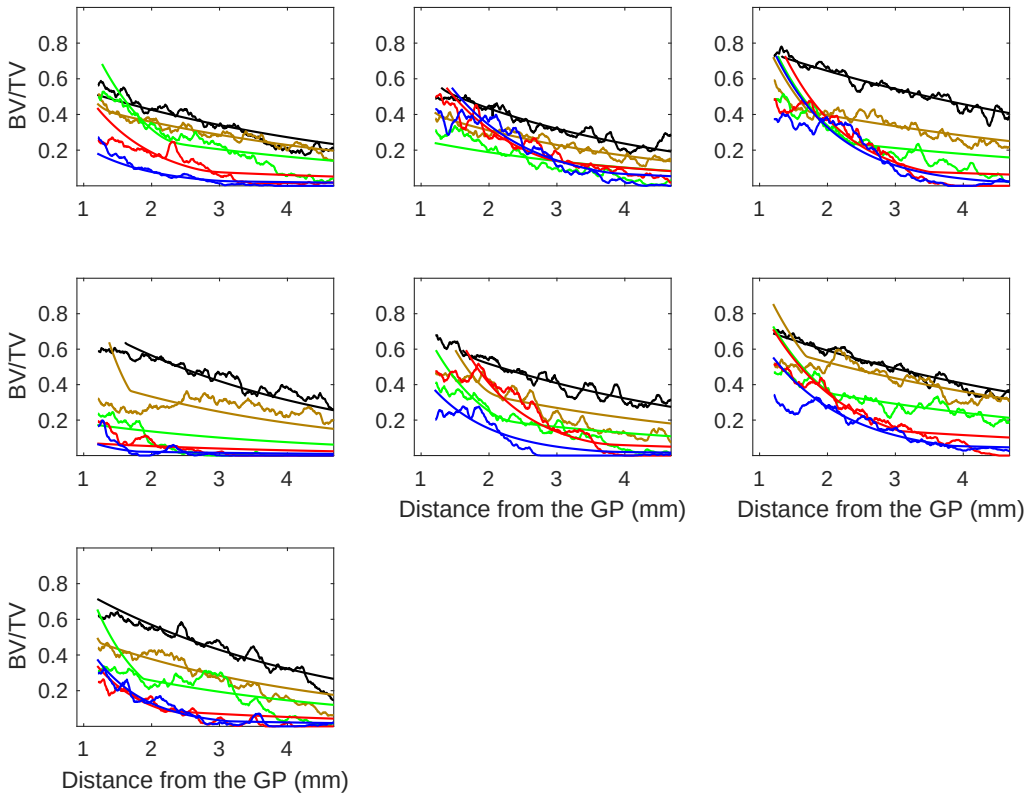

Figure 5.2: Model for $B(x,t)$ for ovx rats. Each figure shows the BV/TV values against distance from the growth plate for each $t = 0$ (black), $t = 14$ (brown), $t = 28$ (green), $t = 56$ (red), and $t = 84$ (blue) for an individual rat from the ovx group plus the model for $B(x,t)$ superimposed according to the same colour scheme. Overall group error for fits is 0.0363.

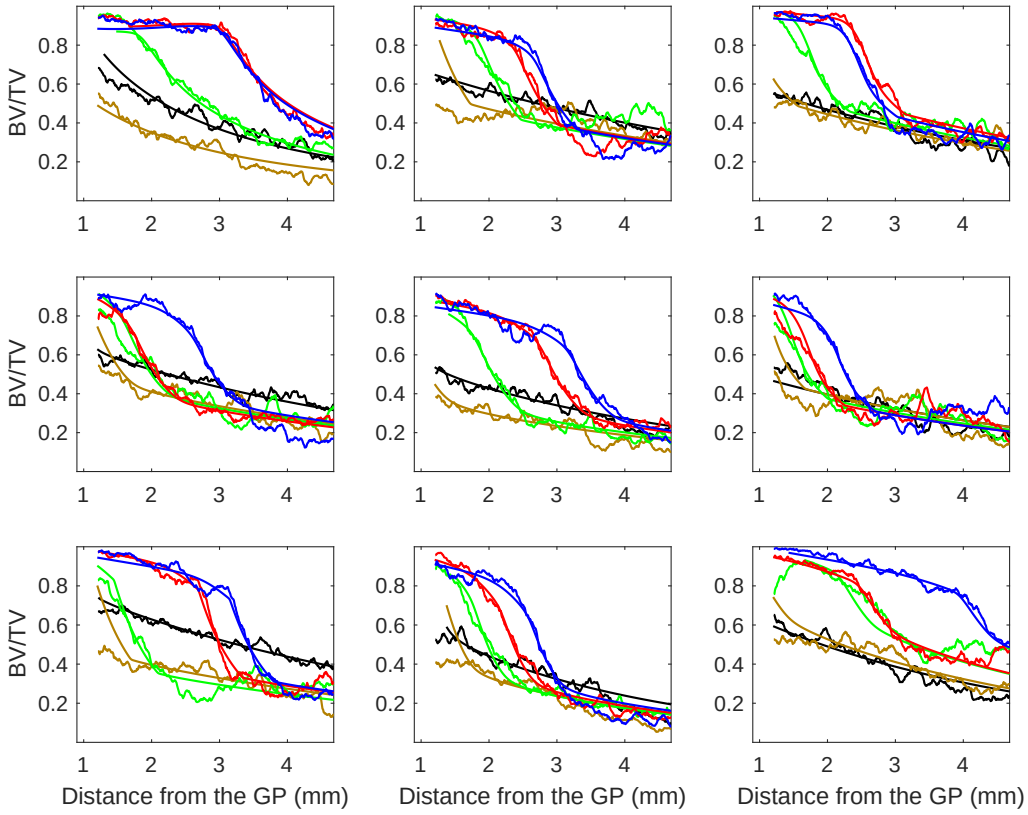

Figure 5.3: Model for $B(x,t)$ for ovx+zol rats. Each figure shows the BV/TV values against distance from the growth plate for each $t = 0$ (black), $t = 14$ (brown), $t = 28$ (green), $t = 56$ (red), and $t = 84$ (blue) for an individual rat from the ovx+zol group plus the model for $B(x,t)$ superimposed according to the same colour scheme. Overall group error for fits is 0.0363.

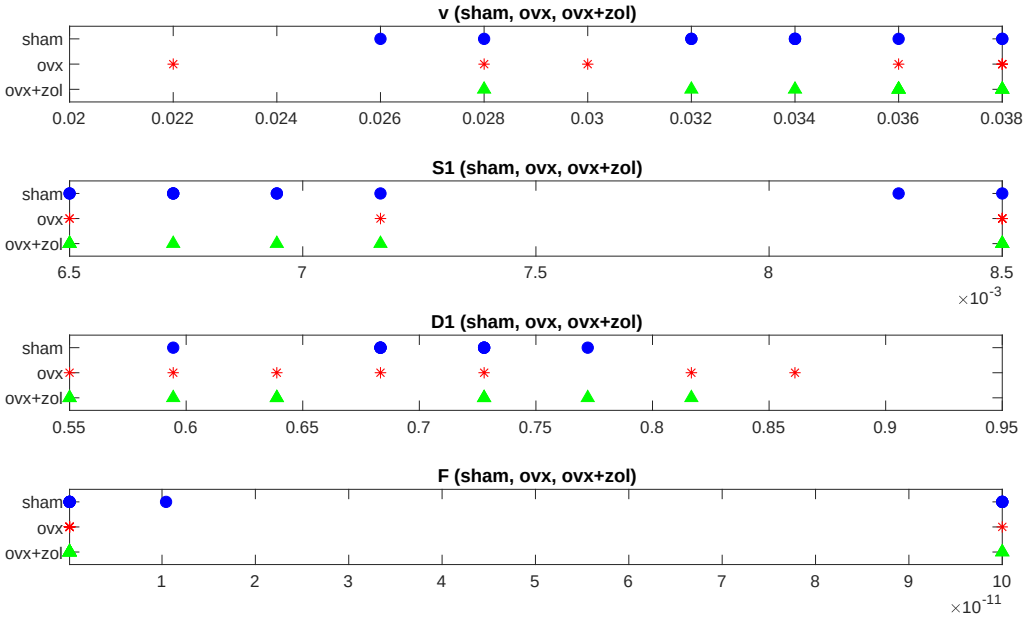

Figure 5.4: Distributions of optimal model parameter values for parameters that apear in the solution for $B(x,t)$ for all three groups. Parameters are v, S_1, D_1, F. Colours are according to group, sham: blue o, ovx: red *, zol: green triangle.

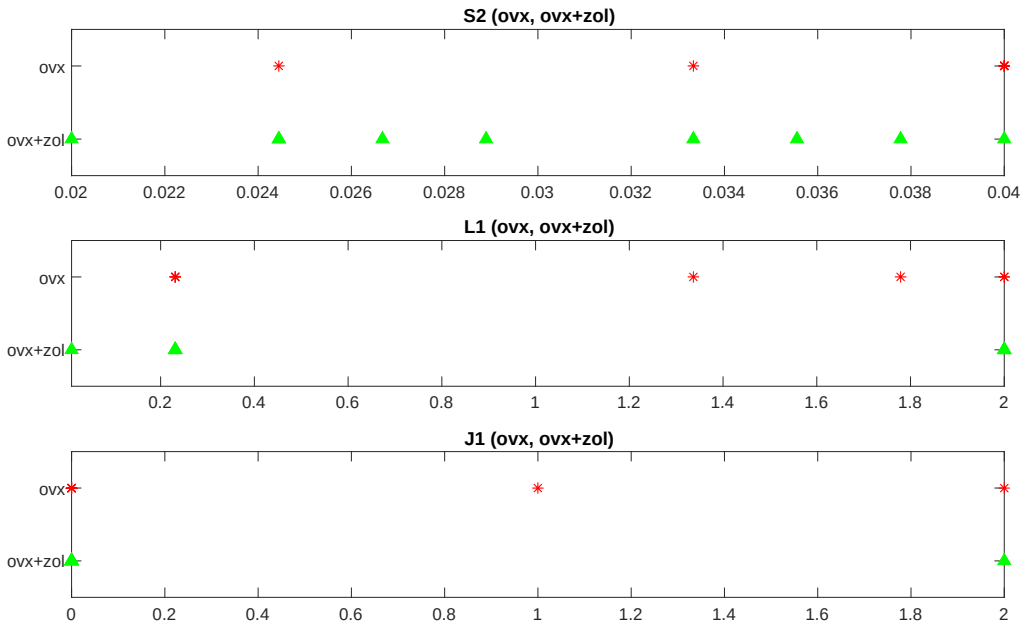

Figure 5.5: Distributions of optimal model parameter values for parameters that apear in the solution for $B(x,t)$ for ovx and ovx+zol rats only. Parameters are S_2, λ_1, J_1. Colours are according to group, ovx: red *, zol: green triangle.

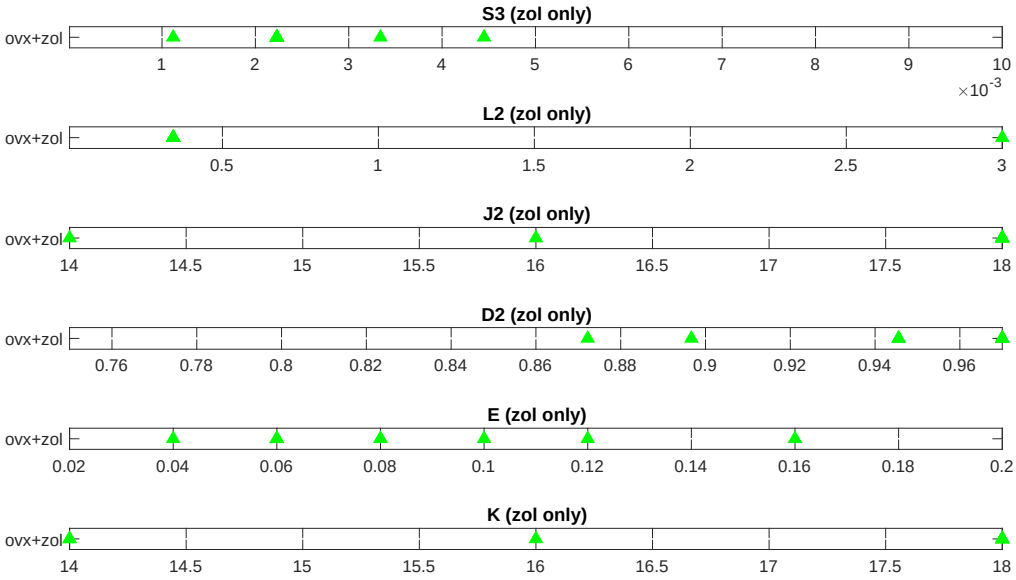

Figure 5.6: Distributions of optimal model parameter values for parameters that apear in the solution for $B(x,t)$ for ovx+zol rats only. Parameters are $S_3, \lambda_2, J_2, D_2, E, K$.

T-test results indicate that the shift distributions, ss, are the same between groups (Table 5.3).

	sham - ovx	sham - ovx+zol	ovx - ovx+zol
p	0.4139	0.1615	0.6839

Table 5.3: P-values for testing that the distributions of the spatial shift values, ss, are the same between groups

Cycle rate Without explicitly resolving the resorption volume parameter, R, the constants in the proportionality term for cycle rate, $C(t)$, also cannot be explicitly resolved. Here, $S_1 = C_1R$ is associated with the cycle rate for all rats at the baseline and for sham rats, $S_2 = C_2R$ is associated with the cycle rate affected by ovariectomy surgery in the rats, and $S_3 = C_3R$ is associated with the cycle rate affected by weekly zoledronic acid treatment in ovariectomised rats. Suppose R changes according to group, then any differences between parameters S_1, S_2, and S_3 will either be more distinct or slightly less distinct. In any event, independent of R values, clearly any trends in S_1, S_2 and S_3 will prevail, and observation of these trends are valid without information about the model parameter R. Results for testing the hypothesis that S_1, S_2 and S_3 are the same, yielded $p < 0.001$ between each pair of parameters. The initial parameter ranges for S_1, S_2 and S_3, were the same, and over time, as the optimisation methods were implemented, values narrowed for each of these parameters. The distribution of S_1, S_2 and S_3 values are shown in Figure 5.8.

Boundary conditions, $D(t)$ Results for testing the hypothesis that D_1 and D_2 are the same, yielded $p < 0.001$ (Figure 5.9). The initial range of values were the same for D_1 and D_2, and the ranges of these two parameters began to diverge early on during the

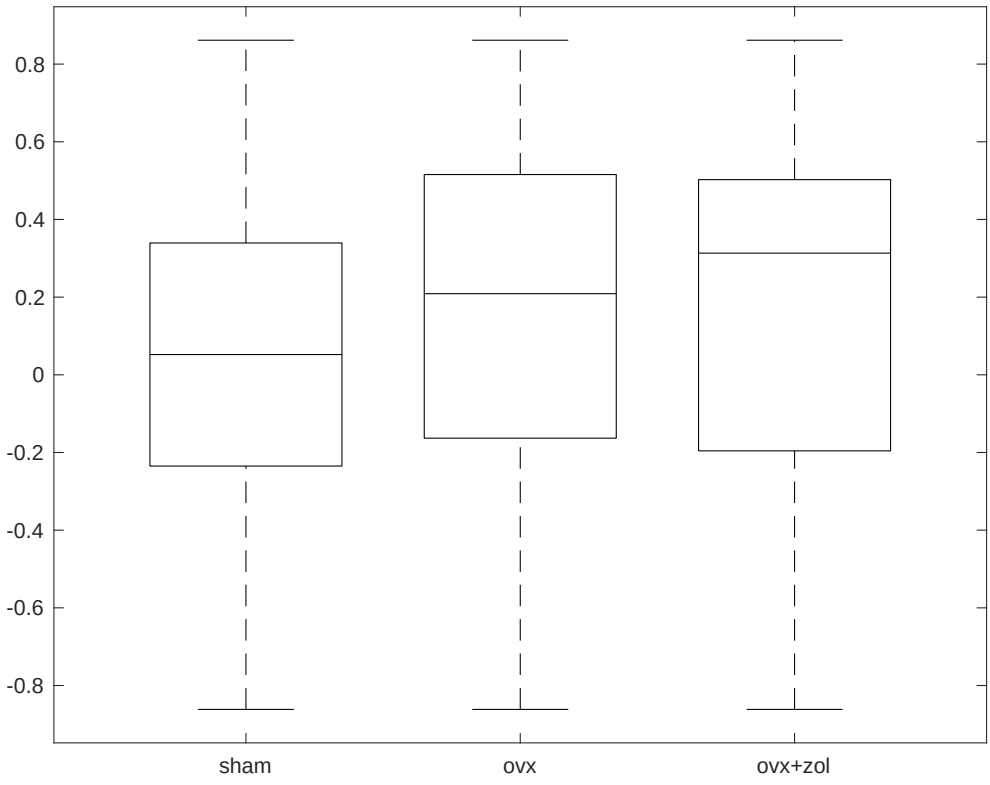

Figure 5.7: Distributions of values for spatial shifts, ss, for each group. The p-values for testing that the distributions are the same for sham, ovx, and ovx+zol are p = 0.4139 (sham-ovx), p = 0.1615 (sham-ovx+zol), and p = 0.6839 (ovx+zol).

optimisation process, as a consequence of minimising the error function between BV/TV values determined by $B(x,t)$ and measured bone block BV/TV values. The distributions of values for D_1 and D_2 are shown in Figure 5.9.

5.2.1 Effect of ovx

The model results for the parameters relating to cycle rate indicated a significant increase from $S_1 = 0.007 \pm 0.001$ (sham,ovx,ovx+zol) to $S_2 = 0.033 \pm 0.007$ (ovx, ovx+zol) ($p < 0.001$). Results also suggest that the effect of the ovariectomy surgery on cycle rate

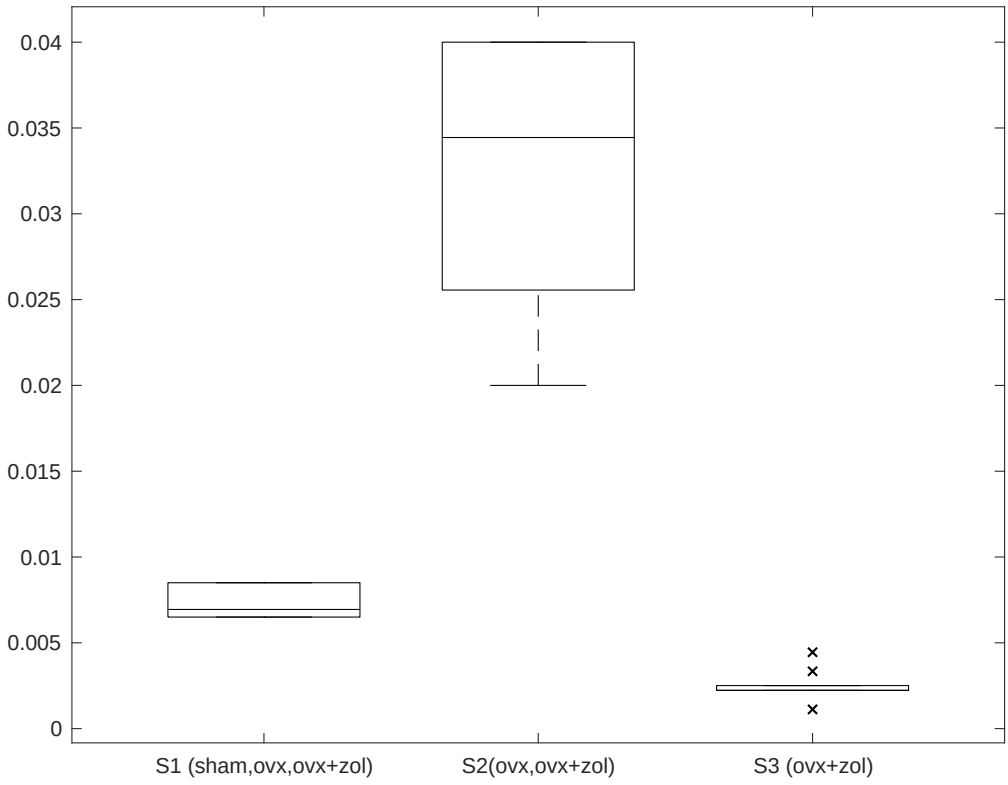

Figure 5.8: Distribution of optimal values for S_1 (sham,ovx,ovx+zol), S_2 (ovx,ovx+zol), S_3 (zol) with initial conditions $s = 0.55$. The p-values for testing that the distributions are the same for S_1, S_2 and S_3 are $p < 0.001$ between $S_1 - S_2$, $S_1 - S_3$, and $S_2 - S_3$.

begins to occur on the same day of surgery where the time shift parameter $J_1 = 0.19 \pm 0.6$ days (ovx,ovx+zol) . Parameter $\lambda_1 = 1.05 \pm 0.9$ describes the rate at which the changes to cycle rate take effect after the time lag.

5.2.2 Effect of ovx+zol

There are two effects of zoledronic acid treatment in ovariectomised rats, including changes to the cycle rate, and changes to the boundary conditions.

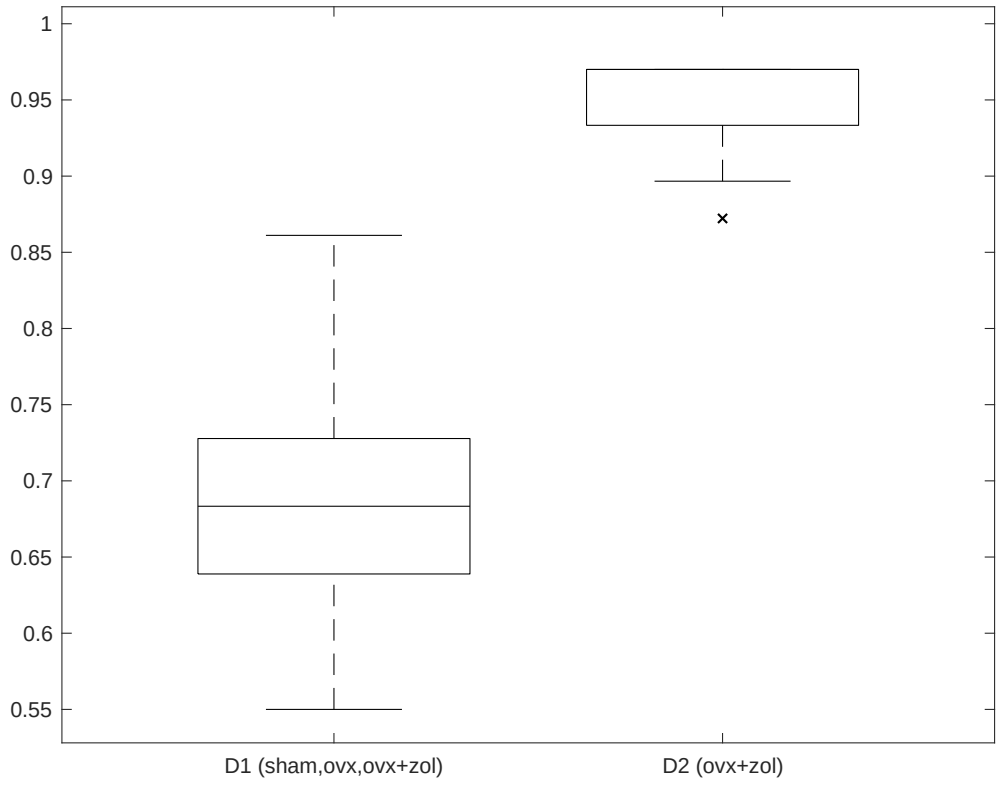

Figure 5.9: Distribution of optimal values for D_1 (sham,ovx,ovx+zol), and D_2 (ovx+zol). The p-value for testing the hypothesis that D_1 and D_2 are the same is $p < 0.001$.

5.2.2.1 Cycle rate

Model results for the parameters associated with cycle rate in ovx+zol rats indicated that there was a significant decrease in the cycle rate after commencement of zoledronic treatment. In the ovx+zol rats, the cycle rate parameter associated with ovariectomy surgery, S_2 (ovx,ovx+zol), shifted to $S_3 = 0.003 \pm 0.009$ (ovx+zol) ($p < 0.001$) . The shift from S_2 to S_3 occurs at $J_2 = 17.3 \pm 1.4$ days, just over 3 days after weekly zoledronic acid treatments begin. The rate of the shift from S_2 to S_3 is given by $\lambda_2 = 0.64 \pm 0.9$. S_3 is also significantly lower than S_1 ($p < 0.001$).

5.2.2.2 Boundary conditions

Results for optimisation of boundary condition parameters indicated a significant increase in the BV/TV of the bone that emerges at $s = 0.55$ in ovx+zol rats. The boundary condition constant changed from $D_1 = 0.69 \pm 0.08$ (sham,ovx,ovx+zol) to $D_2 = 0.95 \pm 0.04$ (ovx+zol). This shift started to occur at $K = 16.9 \pm 1.8$ days on average, almost 3 days after zoledronic bisphosphonate treatments begin.

Chapter 6

Discussion

The goal of this study was to characterise and model BV/TV as a function of distance relative to the growth plate over time, for three experimental groups, sham, ovx and ovx+zol using experimental data and mathematical modelling methods. The BV/TV for the experimental data was presented and analysed in Chapter 2, which motivated the development of the mathematical model for BV/TV that was described in Chapter 3. The optimisation of the model parameters was carried out according to the methodology presented in Chapter 4 and produced the findings that were reported in Chapter 5.

The work in this study yields a model that represents the spatio-temporal changes in BV/TV during growth in terms of simplified model parameters at the tissue scale. The model sufficiently describes the changes in BV/TV according to three key remodelling parameters, including the average formation and resorption volumes during a single remodelling event, $f(B)$ and R respectively, and the cycle rate of remodelling, per unit BV/TV per unit time, $c(B)$, with initial conditions s, and boundary conditions $D(t)$.

The full scope of possible ramifications of the model on the understanding of cancellous bone and the medical consequences are beyond the scope of this work. The modelling results raise several questions and suggest insights that will require additional experimental work to verify or refute.

6.1 Summary of results

This study was able to reduce a very complex system to key model parameters using a mathematical approach combined with inherited experimental data, and describes the basic relationship between key remodelling parameters and BV/TV during growth. The results from this work present important findings for all three groups, and also open questions about the effect of zoledronic acid on BV/TV during growth.

The model for BV/TV, $B(x,t)$, predicts that the number of remodelling events per unit tissue volume and per unit time, $c(B)$ is proportional to the BV/TV for distance x and time t. S_1,S_2,S_3 are primary model parameters associated with the cycle rate, but they do not represent values of biological interest. Average resorption volume per event, R could not be deduced without further work, and thus the exact values of the proportionality constants in $C(t)$ for the model for cycle rate $c(B)$ are not known, as $S_1 = C_1R$, $S_2 = C_2R$, and $S_3 = C_3R$. However the trends are clear.

F is the primary model parameter that is associated with average formation volume during a single remodelling event, but F does not represent a value of biological interest. However, the average formation volume $f(B)$ could not be deduced without further work, as f is dependent on cycle rate $c(B)$.

The model predicts that BV/TV remains constant in juvenile sham rats across the metaphyseal region of data over time. This implies that during endochondral ossification, BV/TV is preserved for $t \geq 0$.

6.1.1 Dominant consequence of ovx

Preliminary observations reported in Section 2.2 revealed that BV/TV decreases throughout the metaphyseal region for ovx rats, for all time $t \geq 0$. The model results suggest that the observed changes to BV/TV in ovx rats can be explained by coupled remodelling at the BMU level. The dominant effect of ovx on bone remodelling was elevation of values of model parameters that are associated with the rate of remodelling. These results confirm the known changes to BMU remodelling in oestrogen-deplete adult organisms, and thus

can be extended to juvenile rats. Results indicate that there were no disturbances local to the growth plate in ovx rats, and that the changes which take effect occur systemically throughout the entire metaphyseal region studied.

6.1.2 Dominant consequence of ovx+zol

Preliminary observations reported in Section 2.2 revealed that BV/TV was higher in ovx+zol rats than in ovx rats throughout the metaphyseal data, for all $t \geq 28$. The BV/TV increased significantly in the bone that emerged during growth after commencement of zoledronic acid treatments. Consequently, in the region of bone closest to the growth plate, BV/TV in ovx+zol rats was higher than all other rats for $t \geq 28$. As the emerging bone with increased BV/TV in ovx+zol rats advanced away from the growth plate, there were less data available in the region furthest away from the growth plate for comparing BV/TV between ovx+zol rats and the other groups. The available data in this region region decreased such that claims could not be made with confidence as to whether the effects of zoledronic acid in this region were either 1.) to restore ovx-related bone loss to baseline (sham) levels, or 2.) to prevent or attenuate ovx-related bone loss.

6.1.2.1 Remodelling parameters

The model results indicate that the changes to the BV/TV that were observed in the older bone that was formed prior to zoledronic acid treatment can be explained by changes to coupled remodelling alone at the BMU level. The effect of ovx+zol on bone remodelling was a decrease in values of the model parameters that are associated with the rate of remodelling. However the BV/TV changes observed in the bone emerging into the window of experimental data after zoledronic acid treatment begins was found to be best modelled by a combination of changes to both bone remodelling parameters, and changes to the BV/TV due to some other unknown processes which were addressed by way of boundary conditions.

6.1.2.2 Boundary conditions

For the ovx+zol rat data used in this study and for many others there is clearly a disturbance to the processes that occurs during endochondral ossification in both nitrogenated and non-nitrogenated bisphosphonates (Section 1.1.4.1). These processes are viewed as occurring either at $s = 0.55$mm from the growth plate, or closer to the growth plate. As the location of these unknown processes is outside the window of experimental data, boundary conditions for the BV/TV of the bone emerging into the data window over time were described by $D(t)$. Exactly what aspect of the endochondral ossification system could be responsible for the abnormal increase in cancellous BV/TV remains unclear. One of the interesting features of this modelling study is that the model is unable to describe the mechanistic processes that lead to the observed changes to BV/TV. This limitation opens many questions about the location of the processes involved, the cells that are involved, and how zoledronic acid causes disruption to the system overall. Several possibilities for the effects of zoledronic acid are discussed below.

Chondroprotective properties Zoledronic acid has been reported as having chondroprotective effects, in that the degradation of cartilaginous material has been arrested in osteoarthritic articular joint cartilage (Section 1.1.4.1). Of interest, is what this chondroprotective property of zoledronic acid could potentially mean for cartilage and bone cells involved in endochondral ossification. The question remains, whether chondroclasts are indeed different enough from their osteoclast relatives such that they perform resorption under separate constraints and regulatory processes than osteoclasts do. Also unclear, is whether chondroclasts communicate with osteoblasts in the same way that osteoclasts do. Further, there is a possibility that osteoblasts might perform bone formation on the cartilage-bone scaffold in a fashion that is not in concert with the cartilage-resorbing chondroclasts. μCT imaging can only resolve mineralised structures, thus without histological testing, there is no way to know for certain whether that the cancellous bone in the experimental data used has a cartilaginous core.

Cartilaginous core Suppose the cartilaginous core persists in the primary spongiosa, as has been observed in some studies (Section 1.1.4.1). Perhaps this effect alone could account for abnormally high BV/TV in the bone emerging into the secondary spongiosa, such that increased BV/TV observations arise solely due to the BMU remodelling machinery acting on a more dense, insufficiently sculpted cartilage template. Zoledronic acid has been shown to suppress expression of PTHrP. Perhaps PTHrP suppression at the growth plate could down regulate the function of chondroclasts to inhibit cartilage resorption.

BMU uncoupling In some studies, the cartilage matrix scaffold in zoledronic acid treated animals was not different to that observed in the control group, however the abnormally high BV/TV of cancellous bone were still observed in the secondary spongiosa (Section 1.1.4). Suppose then, that zoledronic acid impairs the ability of osteoclasts to resorb bone but does not impair the ability of osteoclasts/chondroclasts to resorb cartilaginous material. Then, suppose that the high BV/TV observed in this study and others, are not due to an unsculpted cartilage scaffold, but instead due to some other effect. For example, osteoblasts could become uncoupled from osteoclasts in the primary spongiosa. If this were to be the case, the question arises as to why the very tightly controlled coupling between these cells might malfunction at this location and seemingly not elsewhere in the metaphysis. Possibly, the uncoupling is related to the lower incident of osteocytes in this region. Perhaps there are biological regulatory systems in place to ensure that the osteoblasts continue to deposit bone, despite prior resorption of a) hypertrophic cartilage and/or b) cancellous bone. Perhaps the system allows for abnormally high BV/TV but does not allow for the absence of bone deposition. If uncoupling between osteoblasts and osteoclasts/chondroclasts occurs, further work is required to investigate which regulatory influences could be responsible, and whether these influences are local to the growth plate, or are systemic.

Perhaps the observed abnormal increase in BV/TV could be due to a combination of both chondroprotective processes next to the growth plate, and BMU uncoupling in the primary spongiosa.

6.2 Clinical implications

Technically, results for this study are only valid for rats that were 8 weeks old, as studied over a period of 12 weeks, and were sham operated, or ovariectomised, or first ovariectomised then administered weekly treatments of zoledronic acid, and were housed under specific conditions that include no change to loading conditions, diet or circadian rhythm. Nevertheless, any carry over of the modelling results to more general settings would have significant consequences and are worth considering.

6.2.1 BV/TV studies in growing animals

This study gives reason to believe that the endochondral ossification and coupled BMU remodelling systems may be affected differently under certain experimental conditions. One of most important outcomes in this study is that there is a need for BV/TV to be reported according to distance from the growth plate in growing animals. Reporting a single value for BV/TV over a large volume could misrepresent the effects of treatments on growing bone. More care is to be taken when studying the metaphysis in growing cohorts so as to be able to make observations for changes to the remodelling system separate to changes due to perturbation of endochondral ossification. Observations should be reported separately for the region of bone observed prior to experimentation and for the emerging region of bone after experimentation commences. Results for this study also indicate that certain types of measurements may not suffice for quantifying results in growing animals, including the use of biomarkers other structural or metabolic quantifiers that assume that changes to bone are the same everywhere.

6.2.2 sham conditions

As the model for BV/TV predicts no change to BV/TV over time in sham rats, one of the important implications from this is that juvenile sham rats may be appropriate animal models for studies that test the effects of mechanical loading/diet/pharma agents on bone structure in mature rats. Younger rats are less expensive to prepare for experi-

mentation, and are likely to have less time-related introduced variability that is seen in older rats. However, for experimentation with any growing animals, the observations in cancellous bone should always be viewed as functions of distance from the growth plate in the event that the experimental conditions under investigation affect bone emerging via endochondral ossification differently to older bone.

6.2.3 ovx conditions

Results for changes to BV/TV in ovariectomised growing rats suggest that there were no local disruptions at the growth plate in a way that was different to the effects on BV/TV observed elsewhere. As with sham rats, these results indicate that the juvenile ovariectomised rat also may be an appropriate animal model for testing osteoporosis in mature animals. The drastic changes to BV/TV throughout the entire metaphyseal region also indicate that oestrogen therapy may not be appropriate as a treatment for bone loss, and that localised oestrogen treatment could potentially still have systemic effects elsewhere.

6.2.4 Zoledronic acid treatment

Model results for ovx+zol rats have implications in relation to the increasingly common use of zoledronic acid and bisphosphonates in children with low bone mineral density and bone fragility, and bisphosphonate treatments could be hindering normal skeletal growth. Bisphosphonates are currently prescribed to children and juveniles with osteoporosis caused by various genetic skeletal disorders (Section 1.1.4).

Model predictions for ovx+zol rats are such that the BV/TV of the emerging bone prior to treatment have average BV/TV equal to $D_1 = 0.69$ at $x = 0$, and begin to increase almost immediately, within a day or two after commencement of treatment ($K = 16.9$ days) until reaching average BV/TV equal to $D_2 = 0.95$ at $x = 0$. Further, the model predicts that the BV/TV of the bone emerging from the growth plate remain elevated as endochondral ossification continues, and the high BV/TV persist as the bone travels

away from the growth plate. Should a similar dosing scheme to that which was used for this study be implemented in growing children, exactly whether this would even be structurally detrimental, is not well understood.

6.2.4.1 Dosing schemes and mechanical testing

Other studies that include less frequent and higher doses of bisphosphonate treatments in children have reported the appearance of zebra lines (Section 1.1.4) with intermittent increases in BV/TV according to the time of bisphosphonate administration. Zebra lines were not seen in the rat experimental data used for this work. The increase in the bone emerging from the growth plate in this study, rather steadily increased according to $D(t)$. Possibly, the zebra lines were present in the experimental data but could not be resolved due to lack of spatial/temporal resolution. The growth rate on average was recorded as $v = 0.03$, the injections were roughly weekly, and the µCT data slices are separated by a distance of 0.0087mm. Thus the zebra lines would in the experimental data occur every 20-30 slices.

Perhaps the disturbance at the the growth plate during endochondral ossification could be minimised or addressed by changing the bisphosphonate dosing regimen in children. Zebra lines pose a fracture risk due to sharp changes to BV/TV of the cancellous bone, and work in this area would be served well to include mechanical testing in addition to the usual histomorphometric and histological testing. There may be an optimal dose to prevent zebra lines or to prevent the accumulative and persisting high BV/TV that were observed in this study.

Most certainly, long term effects of zoledronic treatment in growing cohorts deserves further investigation, and they have been detected in children up to eight years after treatment cessation (Section 1.1.4).The rat model may not be appropriate for investigation of long term effects of zoledronic acid treatment, due to the persisting growth plate that never fuses.

.

6.3 Limitations of the model

All models have limited validity, but by prescribing systems mathematically, properties can be observed and predicted that may not be obvious to the experimenter. Some of the issues that this study was limited by are challenges that span across all areas of mathematical modelling, including spatial/temporal complexity, parameter estimation, treatment of uncertainty and statistical analysis. The inclusion of spatial shifts for each rat at each time point served well to address some of the uncertainty that arises from the factors listed below, with normally distributed values across the groups and no difference in the distributions between groups, indicating that there was no one group or time point that requires shifts more than other, and the degree of variability was the same across groups.

6.3.1 Growth rate v

For simplification, the growth rate model parameter v was modelled as a constant, and determined during the fixed resolution optimisation scheme, along with the other twelve parameters. The range of optimised values for v were comparable to experimental values reported in the literature (Modi *et al.* , 2011; Leppanen *et al.* , 2010; Roach *et al.* , 2003). However, are many factors that influence growth rate over shorter and longer time periods (Section 1.1.2.1). Within any given day, the rate of growth is related to the delicate balance and modulation of chondrocyte proliferative kinetics, matrix synthesis/degradation and the enlargement processes of chondrocytes in the hypertrophic zone.

6.3.2 Initial conditions

Results for setting the initial conditions, or the effective point of bone formation, for $x = 0$ at $s = 0.8$ gave the best visual fits across all rats. A single value was determined for all 26 rats, where this is a parameter that could be different between groups, or between rats, or even between time points for a given rat.

The chondro-osseous junction is not a flat line perpendicular to the medial axis, but rather has curvature that deviates along the perpendicular direction up to 0.5mm (Kimmel & Jee, 1980). Setting $x = 0.8$mm from the bottom of the growth plate puts the effective point of bone deposition somewhere in the vicinity of the chondro-osseous junction and where the primary spongiosa transitions to secondary spongiosa. Prescribing the effective point of bone deposition was necessary for initial conditions for the model, however this is not a straight forward concept. $x = 0$ could be the location where the calcified cartilage template emerges from the hypertrophic zone and is replaced by bone due to coupled remodelling. $x = 0$ could be at a location where the material is still calcified cartilage, waiting to be remodelled by differentiating osteoblasts and osteoclasts. These distances are also affected by the height of the growth plate which changes due to chondrocyte behaviour. The height does reach short periods of steady state, but can change even within a 24 hour period (Wilsman *et al.* , 1996).

6.4 Further work for this study

This work presents a simplified model which provides opportunity for future improvements in both mathematical modelling strategies and experimental data collection.

6.4.1 Modelling parameters

A more sophisticated version of the model could include cyclical behaviour for v, or at least allow v to be modelled as a function of time and/or distance relative to the growth plate according to some or all of the factors mentioned above in Section 6.3.1. Further uncertainty for the growth rate arises due to the unknown influences from oestrogen depletion or bisphosphonate treatment (Sections 1.1.2 and 1.1.4).

Future work could allow for added complexity for initial conditions. In addition to the above limitations mentioned in Section 6.3.2 that put $x = 0$ in question, even less understood are under the influences on $x = 0$ due to ovariectomy or ovariectomy combined with zoledronic acid treatments.

$D(t)$ could be improved to include oscillations for zebra lines, where the BV/TV may still continue to increase over time for ovx+zol rats, though with additional cyclical fluctuations according to frequency of dosing.

In addition to the levels of complexity that could be added to initial conditions, s, growth rate v and boundary conditions $D(t)$, further work is required to resolve C_1, C_2, C_3 and R. In prior work carried out by Fazzalari *et al.* (2012), R was resolved by simulating bone remodelling according to the optimised model parameters over a range for biologically reasonable values for R. Here the bone block at $t = 0$ was used to initialise simulations and structural attributes were used in an error function for comparing the simulated bone block at the remaining 4 experimental data points ($t = 14, 28, 56, 84$). An optimised value of R was the value that minimised the error function and thus produced simulated bone that best matched the structure of the experimental data , where R values were determined for each group.

Similarly, an extension for this model in the future could include a second stage involving simulation, in the following way. The bone block extending from the left side of the window ($x = 1.2$mm) to the right side of the window ($x = 4.7$mm) could be broken up into 5 smaller bone blocks, and each of these sub bone blocks could be simulated over time and structurally compared to the experimental data by shifting the bone block domain Ω_i for $i = 1 : 5$ to the right away from the growth according to the growth rate, v. A smaller bone block with domain Ω_i is used as the initial state and individual remodelling events are simulated according model parameters in $B(x, t)$ and continued over time, where the resulting structural attributes are compared to the original unsimulated bone blocks at distance $x = x + tv$ for each t.

6.4.2 Experimental data

Increased spatial and temporal resolution in μCT data also could greatly aid improvements of the mathematical model for BV/TV. The effects of the zoledronic acid treatment were not observable until $t = 28$, leaving only three timepoints of the five in total. Additional scanning between timepoints would be advantageous for the spatial resolution of

the experimental data studied for this project. An extended time frame for observations could also lead to further insights. For ovx+zol rats, the model predicts that the increase in BV/TV will persist under the same conditions with continued weekly zoledronic acid treatment, and that the increased BV/TV will continue to travel away from the growth plate according to v. Of interest, is the potential impact that this phenomenon could have on the emerging structure long term. Should conditions change, for example cessation of zoledronic acid treatment, further investigation would be required to investigate whether the bone remodelling machinery may be able restore the abnormally dense bone to normal density over time. Suppose the abnormal BV/TV is due to a persisting cartilaginous core, perhaps over time, the remodelling machinery may be able to replace the cartilaginous material with bone material. The possibility remains that the high BV/TV observed in ovx+zol rat experimental data may not even be overall disadvantageous to the organism longterm. In fact, there may be scenarios where perhaps the high BV/TV may be advantagous, say for instance, in the case of secondary osteoporosis caused by implantation.

Chapter 7

Summary and concluding remarks

A summary is provided of results, recommendations and future perspectives.

7.1 Key findings

A model was developed to provide a simplified description of BV/TV that relates remodelling processes to observed BV/TV in longitudinal experimental µCT data in growing juvenile rats. The results demonstrate that the approach is sufficient at the tissue scale to draw some important conclusions about the effects of ovariectomy, and ovariectomy combined with zoledronic acid treatment.

In summary, the results indicate the following:

- for sham rats, the BV/TV did not change over time during growth;
- for ovx rats, BV/TV decreased throughout the metaphysis;
- the dominant effect of ovx was elevation of values of model parameters that are associated with the rate of bone remodelling;
- for ovx+zol rats, BV/TV was higher throughout the metaphysis than the BV/TV in ovx rats after zoledronic acid treatments begin, though results are inconclusive

as to whether the effect of zoledronic acid was to restore BV/TV in ovariectomised animals, or to prevent further bone loss;

- for the ovx+zol rats there was a dramatic local increase in BV/TV of the bone that had emerged from during growth after zoledronic acid treatments began;
- the dominant effect for ovx+zol was to decrease values of model parameters that are associated with the rate of bone remodelling;
- bone remodelling alone sufficed to model the observed values of BV/TV at all time points for the sham and ovx rats; and
- for ovx+zol rats, in the region of bone that had emerged during growth after commencement of zoledronic acid treatment, changes to BV/TV were modelled as being a combination of changes to bone remodelling parameters and changes to unknown processes that occurred outside the window of experimental data.

The fact that the model results are in agreement with current understanding of the effects of ovx and ovx+zol on bone remodelling for mature rats indicates that viewing bone remodelling at this very course scale provides confirmation of what is known for adult rats and gives reason to believe that this knowledge can be extended to growing rats.

7.2 Future research

As discussed in Chapter 6, there are several opportunities for further work in this spatio-temporal modelling study, including improvements to both modelling methods and collection of experimental data. There are a few parameters of the model that have potential for further levels of complexity, including the growth rate, v, the initial conditions, and the boundary conditions $D(t)$. An additional simulation step could be implemented to resolve model parameter values for resorption volume, R, and for the proportionality constants in the cycle rate term, $C(t)$. Sample sizes of experimental data could be made larger for the purpose of statistical analysis. Larger sample sizes are expensive, and thus

collection of more data could be combined with additional experimental methods including increased spatial and temporal resolution, reporting of size measurements of the rats over time, studying the bone histologically, and carrying out mechanical testing.

More generally, model results indicate that BV/TV and other structural properties of bone in growing cohorts should be viewed as functions of the growth plate. Older bone that emerges during growth prior to experimentation should be reported on separately to newly emerged bone. Until this becomes the standard, there is no way to determine any differential effects that agents or experimental conditions may have during endochondral ossification in growing bone, compared to older bone.

For experimental studies investigating zoledronic acid treatment in growing animals, model results also demonstrated the need for:

- resolution of cartilaginous material at and near the growth plate, in addition to potential cartilaginous core that may persist in cancellous bone;
- testing of mechanical properties of cancellous bone; and
- further work to potentially identify desirable zoledronic acid dosing schemes.

7.3 Outlook

The model for BV/TV presented in this study provides a significant step forward towards understanding the changes to the remodelling machinery in growing juvenile rats over time for ovariectomised rats and ovariectomised rats treated with zoledronic acid. The results of the modelling experiments are clear. The results provide an explanation for changes in terms of mechanics, and predict changes to BV/TV under the experimental conditions. The trends are in agreement with those evidenced by both modelling and experiential studies across various spatial and temporal scales.

The current body of knowledge includes contributions from mathematical modelling of both growth plate dynamics during prenatal and postnatal growth, and for the many

models of bone remodelling in cancellous and cortical bone. However, there is a gap in what is known about the system in between. The system in between lies in the region where cartilage meets bone in the chondro-osseous junction. Here, local growth plate regulatory signalling activity meets the endocrine and systemic signalling activity at the vascular front, and very little is known about exactly how these two types of signalling molecules interact with each other. This system is nested between the current boundary of knowledge for the growth plate dynamics and the current boundary of knowledge for bone remodelling dynamics. There is a need to capture the mechanics, and will require careful experimental design in combination with building mathematical models for testing the dynamics of experimental findings.

The interesting feature of the model results is where the model is unable to describe all of the BV/TV changes in terms of mechanics for the ovx+zol rats. As is common for modelling, boundary conditions were prescribed to address the issue of unknown mechanics which operate outside the domain of the experimental data used, located in the region that cannot be fully captured with current μCT technology. Now that the increased BV/TV of the emerging bone in the ovx+zol rats has been observed and modelled qualitatively, an effort is required to deepen the current understanding of the mechanics at play.

This modelling study provides a starting point towards the development of a full multiscale model that includes the intricacies of the development of endochondral ossification in growing animals and changes to this system due to pathologies like ovariectomy and zoledronic acid treatment. A multidisciplinary effort is required now, for experts across the sciences to give priority towards a better understanding of this system. Scientists from the fields of image analysis, biochemistry, biophysics, engineering, biology, medicine and mathematics need to share findings, as has been done extensively thus far for the two systems either side of the chondro-osseous junction.

Bibliography

Adam, J A. 1999. A simplified model of wound healing with particular reference to the critical size defect. *Mathematical Computational Modeling*, **20**, 23–32.

Adam, J A. 2002. THe effect of surface curvature on wound healing in bone : II. The critical size defect. *Mathematical Computational Modeling*, **35**, 1085–1094.

Alias, Mohd Almie, & Buenzli, Pascal R. 2018. Osteoblasts infill irregular pores under curvature and porosity controls: a hypothesis-testing analysis of cel behaviours. *Biomechanics and Modeling in Mechanobiology*, **17**(5), 1357–1371.

Allen, Matthew R. 2018. Recent Advances in Understanding Bisphosphonate Effects on Bone Mechanical Properties. *CURRENT OSTEOPOROSIS REPORTS*, **16**(2), 198–204.

Alliston, Tamara, & Derynck, Rik. 2002. Medicine: Interfering with bone remodeling. *Nature*, **416**(6882), 686–687.

Ambard, D, & Swider, P. 2006. A predictive mechano–biological model of the bone-implant healing. *European Journal of Mechanics A/Solids*, **25**, 927–937.

Ament, C, & Hofer, E P. 2000. A fuzzy logic model of fracture healing. *Journal of Biomechanics*, **33**, 961–968.

Bailon-Plaza, A, & Meulen, M C H van der. 2003. Beneficial effects of moderate, early loading and adverse effects of delayed or excessive loading on bone healing. *Journal of Biomechanics*, **36**, 1069–1077.

Biggin, Andrew, Briody, Julie, Ormshaw, Elizabeth, Wong, Karen K Y, Bennetts, Bruce H, & Munns, Craig F. 2014. Fracture during Intravenous Bisphosphonate Treatment in a Child with Osteogenesis Imperfecta: An Argument for a More Frequent, Low–Dose Treatment Regimen. *HORMONE RESEARCH IN PÆDIATRICS*, **81**, 204–210.

Bilezikian, John P, Matsumoto, Toshio, Bellido, Teresita, Khosla, Sundeep, Martin, Jack, Recker, Robert R, Heaney, Robert, Seeman, Ego, Papapoulos, Socrates, & Goldring, Steven R. 2009. Targeting Bone Remodeling for the Treatment of Osteoporosis: Summary of the Proceedings of an ASBMR Workshop. *JOURNAL OF BONE AND MINERAL RESEARCH*, **24**, 373–385.

Börjesson, A E, Lagerquist, M K, Windahl, S H, & Ohlsson, C. 2013. The role of estrogen receptor α in the regulation of bone and growth plate cartilage. *Cellular and Molecular Life Sciences*, **70**, 4023–4037.

Boyce, Alison MD, Tosi, Laura L, & Paul, Scott M. 2014. Bisphosphonate Treatment for Chidlren With Disabling Conditions. *PM AND R*, **6**, 427–436.

Boyd, Steven K, Davison, Peter, Muller, Ralph, & Gasser, Jurg. 2006. Monitoring individual morphological changes over time in ovariectomized rats by in vivo micro-computed tomography. *Bone*, 854–862.

Brouwers, J E M, van Donkelaar, C C, Sengers, B G, & Huiskes, R. Can the growth factors PTHrP, Ihh and VEGF, together regulate the development of a long bone?

Brouwers, J E M, Lambers, F M, Gasser, L A, van Rietbergen, B, & Huiskes, R. 2008. Bone Degeneration and Recovery after Early and Late Bisphosphonate Treatment of Ovariectomized Wistar Rats Assessed by In Vivo Micro–Computed Tomography. *Calcified Tissue International*, **82**, 202–211.

Browers, J E M, van Donkelaar, C C, Sengers, B G, & Huiskes, R. 2006. Can the growth factors PTHrP, Ihh and VEGF, together regulate the development of a long bone? *Journal of Biomechanics*, **39**, 2774–2782.

Brown, Jacques P, ALbert, Caroline, Nassar, Bassam A, Adachi, Jonathan D, Cole, David, adn Kent Dooley, K Shawn Davison, Don-Wauchope, Andrew, Douville, Pierre, Hanley, David A, jamal, Sophie A, Josse, Robert, Kaise, Stephanie, Krahn, John, Krause, Richard, Kremer, Richerd, Lepage, Rayomd, Letendre, Elaine, Morin, Suzanne, Ooi, Daylily S, Papaioaonnou, Alexamdra, & Ste-Marie, Louis-Georges. 2009. Bone turnover markers in the management of postmenopausal osteoporosis. *Clinical Biochemistry*, **42**, 929–942.

Buenzli, P R, Pivonka, P, & Smith, D W. 2011. Spatio–temporal structure of cell distribution in cortical Bone Multicellular Units: A Mathematical model. *Bone*, **48**, 918–926.

Buenzli, Pascal, Pivonka, Peter, Gardiner, Bruce S, & Smith, David W. 2013. Modelling the anabolic response of bone using a cell population model. *Journal of Theoretical Biology*, **307**, 42–52.

Buenzli, Pascal R. 2015. Osteocytes as a record of bone formation dynamics: A mathematical model of osteocyte generation in bone matrix. *Journal of Theoretical Biology*, **264**, 418–427.

Buenzli, Pascal R, & Sims, Natalie A. 2015. Quantifying the osteocyte network in the human skeleton. *BONE*, **75**, 144–150.

Bukowski, Jack F, Dascher, Christopher C, & Das, Hiranmoy. 2005. Alternative bisphosphonate targets and mechanisms of action. *Biochemical and Biophysical Research Communications*, **328**, 746–750.

Burger, Elisabeth H, & Klein-Nulend, Jenneke. 1999. Mechanotransduction in bone – role of the lacuno-canalicular network. *The FASEB Journal*, **13**, S101–S112.

Burr, David B, Martin, R Bruce, Schaffler, Mitchel B, & Radin, Eric L. 1985. BONE REMODELING IN RESPONSE TO IN VIVO FATIGUE MICRODAMAGE. *Journral of Biomechanics*, **18**(3), 189–200.

Cappariello, Alfredo, Maurizi, Antonio, Veeriah, Vimal, & Teti, Anna. 2014. The great beauty of the osteoclast. *Archives of Biochemistry and Biophysics*, **558**, 70–78.

Carter, D R. 1987. Mechanical loading history and skeletal biology. *Journal of biomechanics*, **20**, 1095–1109.

Carter, D R, Baupre, G S, Giori, N J, & Helms, J A. 1998. Mechanobiology of skeltal regeneration. *Clinical Orthapaedic Related Research*, **355S**, S41–S55.

Carvas, J S, Pereira, R M R, Caparbo, V F, Fuller, P, Silveira, C A, Lima, L A P, Bonfa, E, & Mello, S B V. 2010. A single dose of zoledronic acid reverses the deleterious effects of glucocorticoids on titanium implant osseointegration. *Osteoporosis International*, **21**, 1723–1729.

Chow, J W M, Wilson, A J, Chambers, T J, & Fox, S W. 1998. Mechanical Loading Stimulates Bone Formation by Reactivation of Bone Lining Cells in 13–Week–Old–Rats. *Journal of Bone and Mineral Research*, **13**, 1760–1767.

Claes, L E, & Heigele, C A. 1999. Magnitudes of local stress and strain along bony surfaces predict the course and type of fracture healing. *Journal of Biomechanics*, **32**, 255–266.

Clowes, J A, Hannon, R A, Yap, T S, Hoyle, N R, Blumsohn, A, & Eastell, R. 2002. Effect of Feeding on Bone Turnover Markers and Its Impact on Biological Variability of Measurements. *Bone*, **30**(6), 886–890.

Coelho, P G, Fernandes, P R, Rodrigues, H C, Cardoso, J B, & Guedes, J M. 2009. Numerical modeling of bone tissue adaptation – A hierarchical approach for bone apparent density and trabecular structure. *Journal of Biomechanics*, **42**, 830–837.

Coleman, Robert. 2010. The use of bisphosphonates in cancer treatment. *ANNALS OF THE NEW YORK ACADEMY OF SCIENCES*, **1218**, 3–14.

Cornea, Nicu D, Silver, Deborah, Yuan, Xiaosong, & Balasubramanian, Raman. 2005. Computing Hierarchical Curve–Skeletons of 3D Objects. *The Visual Computer*, **21**(11), 945–955.

Corsi, Alessandro, Ippolito, Ernesto, Robey, Pamela G, Riminucci, Mara, & Boyde, Alan. 2017. Bisphosphonate-induced zebra lines in fibrous dysplasia of bone: histo-radiographic correlation in a case of McCune-Albright syndrome. *Skeletal Radiology*, **46**, 1435–1439.

Courteix, D, Lespessailles, E, Peres, S Louseau, Obert, P, Germain, P, & Benhamou, C L. 1998. Effect of Physical Training on Bone Mineral Density in Prepubertal Girls: A Comparative Study Between Impact-Loading and Non-Impact-Loading Sports. *Osteoporosis International*, **8**, 152–158.

Cowin, S, & Wienbaum, S. 1998. Strain amplification in the bone mechanosensory system. *American Journal of Medical Sciences*, **316**, 184–188.

Cowin, S C, Moss-Salentijn, L, & Moss, M L. 1991. Candidates for the Mechanosensory System in Bone. *Journal of Biomechanical Engineering*, **113**, 191–197.

Cowin, Stephen C. 2005. Tensile and compressive stress yield criteria for cancellous bone. *Journal of Biomechanics*, **38**, 14–144.

Cowin, Stephen C. 2007. The significance of bone microstructure in mechanotransduction. *Journal of Biomechanics*, **40**, S105–109.

Cremers, S, Drake, M T, Ebetino, F H, Bilezikian, J P, & Russel, R G G. 2019. Pharmacology of bisphosphonates. *BRITISH JOURNAL OF CLINICAL PHARMACOLOGY*, **85**(6), 1052–1062.

Cremers, Serge, & Garnero, Patrick. 2006. Biochemical Markers of Bone Turnover in the Clinical Development of Drugs for Osteoporosis and Metastatic Bone Disease. *Drugs*, **66**(15), 2031–2058.

D'Amelio, P, Grimaldi, A, Cristofaro, M A, Ravazzoli, M, Molinatti, P A, Pescarmona, G P, & Isaia, G C. 2010. Alendronate reduces osteoclast precursors in osteoporosis. *Osteoporosis International*, **21**, 1741–1750.

Dickson, G R, Geddis, C, Fazzalari, N, Marsh, D, & Parkinson, I. 2007. Microcomputed Tomography Imaging in a Rat Model of Delayed Union/N on–Union Fracture. *JOURNAL OF ORTHAPAEDIC RESEARCH*, **26**, 729–736.

Elefteriou, Florent, Ahn, Jong Deok, Takeda, Shu, Starbuck, Michael, Yang, Xiangli, Liu, Xuiyun, Kondo, Hisataka, Richards, William G., Bannon, Tony W., Noda, Masaki, Clement, Karine, Vaisse, Christian, & Karsenty, Gerard. 2004. Leptin regulation of bone resorption by the sympathetic nervous system. *Nature*, **1038**.

Erben, R G, Kohn, B, Rambeck, W A, & Zucker, H. 1990. HISTOMORPHOMETRIC ANALYSIS OF THE RAT PROXIMAL TIBIAL METAPHYSIS BY "LINEAR SCANNING". *Scanning Microscopy*, **4**(3), 625–640.

Erben, Riehnhold. 1995. Trabecular and Endocortical Bone Surfaces in the Rat: Modeling or Remodeling? *The Anatomical Record*, **246**, 39–46.

Erdogan, M, Bereket, C, Ozkan, N, Alici, O, Sener, I, Desteli, E E, & Ilkaya, F. 2019. The effect of zoledronic acid on growth plates and high turnover. *BRATISLAVA MEDICAL JOURNAL*, **115**(3), 131–135.

Evans, K D, Lau, S T, Oberauer, A M, & Martin, R B. 2003. Alendronate affects long bone length and growth plate morphology in the *oim* mouse model for Osteogenesis Imperfecta. *Bone*, **32**, 268–274.

Fazzalari, Nicola L, Martin, Brianna L, Reynolds, Karen J, Cleek, Tammy M, Badiei, Arash, & Bottema, Murk J. 2012. A model for the change of cancellous bone volume and structure over time. *Mathematical Biosciences*, **240**, 132–140.

Fleisch, Herbert. 1998. Bisphosphonates: Mechanisms of Action. *Endocrine Reviews*, **19**(1), 80–100.

Fyhrie, D P, & Schaffler, M B. 1995. THE ADAPTATION OF BONE APPARENT DENSITY TO APPLIED LOAD. *Journal of Biomechanics*, **28**(2), 135–146.

Fyhrie, D P, Fazzalari, N L, Goulet, R, & Goldstein, S A. 1993. DIRECT CALCULATION OF THE SURFACE–TO–VOLUME RATIO FOR HUMAN CANCELLOUS BONE. *Journal of Biomechanics*, **26**(8), 955–967.

Fyhrie, D P, Lange, S M, Hoshaw, S J, Schaffler, M B, & Kuo, R F. 1995. Human Vertebral Cancellous Bone Surface Distribution. *Bone*, **17**(3), 287–291.

Gabet, Yankel, Kohavi, David, Kohler, Thomas, Baras, Mario, Múller, Ralph, & Bab, Itai. 2008. Trabecular Bone Gradient in Rat Long Bone Metaphyses: Mathematical Modeling and Application to Morphometric Measurements and Correction of Implant Positioning. *JOURNAL OF BONE AND MINERAL RESEARCH*, **23**, 48–57.

Garimella, Rama, Tague, Sarah E, Zhang, Jianghong, Belibi, Frank, Jahar, Niru, Sun, B H, Insogna, Karl, Wang, Jinxi, & Anderson, H Clarke. 2008. Expression and Synthesis of Bone Morphogenetic Proteins by Osteoclasts – A Possible Path to Anabolic Bone Remodeling. *Journal of the Histochemical Society*, **1369**(10).

Garzón-Alvarado, D A, García-Aznar, J M, & Doblaré, M. 2009. A reaction–diffusion model for long bones growth. *Biomechanics and Modeling in Mechanobiology*, **8**, 381–395.

Garzón-Alvarado, D A, Narváez-Tovar, Carlos A, & Silva, Octavio. 2011. A MATHEMATICAL MODEL OF THE GROWTH PLATE. *Journal of Mechanics in Medicine and Biology*, **11**, 1213–1240.

Geris, L, Oosterwyck, H Van, Sloten, J Vander, Keulen, F van, Duyck, J, & Naert, I. 2008. Angiogenesis in bone fracture healing: a bioregulatory model. *Journal of Theoretical Biology*, **251**, 137–158.

Geris, L, Sloten, J Vander, & Oosterwyck, H Van. 2009. In Silico biology of bone remodelling and remodelling: regeneration. *PHILOSOPHICAL TRANSACTIONS OF THE ROYAL SOCIETY A*, **367**, 2031–2053.

Girotra, Monica, Rubin, Mishaela R, & Bilezikian, John P. 2006. Anabolic Skeletal Therapy for Osteoporosis. *Arq Bras Endocrinal Metab*, **50**(4), 745–754.

Gontar, Amelia, Tronnolone, Hayden, Binder, Benjamin J, & Bottema, Murk J. 2018. Characterising shape patterns using features derived from best-fittig ellipsoids. *Pattern Recognition*, **83**, 365–374.

Guo, X E, & Kim, C H. 2002. Mechanical consequence of trabecular bone loss and its treatment: a three–dimensional model simulation. *Bone*, **30**, 404–411.

Henderson, J H, & Carter, D R. 2002. Mechanical induction in limb morphogenesis: the role of growth-generated strains and pressures. *Bone*, **31**, 645–653.

Holstein, Sarah A. 2019. A patent review of bisphosphonates in treating bone disease. *EXPERT OPINION ON THERAPEUTIC PATENTS*, **29**(5), 315–325.

Hornby, S B, Evans, G P, Hornby, S L, Pataki, A, Glatt, M, & Green, J R. 2003. Long-term zoledronic acid treatment increases bone structures and mechanical strength of long bones of ovariectomized adult rats. *Calcified Tissue International*, **72**, 519–527.

Huiskes, R, Driel, W D Van, Prendergast, P J, & Soballe, K. 1997. A biomechanical regulatory model for periprosthetic fibrous–tissue differentiation. *Journal of Material Science and Medicine*, **8**, 785–788.

Huiskes, Rik, Ruimerman, Ronald, Lenthe, G, & Janssen, Jan D. 2000. Effects of mechanical forces on maintenance and adaptation of form in trabecular bone. *Nature*, **405**, 704–706.

Hunziker, E B, Kapfinger, E, & Geiss, J. 2007. The structural architecture of adult mammalian articular cartilage evolves by a synchronized process of tissue resorption

and neoformation during postnatal development. *Osteoarthritis and Cartilage*, **15**(4), 403–413.

ichi Nakahama, Ken. 2010. Cellular communications in bone homeostasis and repair. *Cellular and Molecular Life Sciences*, **76**, 4001–4009.

Ishizuka, Mariko, Tsuji, Shoji, Hrabayashi, Masato, & Kaneko, Kazunari. 2017. Characteristic Bands Manifesting as Zebra Lines on Radiographs in Osteogenesis Imperfecta. *Indian Journal of Pediatrics*, **84**(4), 336.

Jilka, Robert L, Weinstein, Robert S, Parfitt, A M, & Manolagas, Stavros C. 2007. Perspective. Quantifying Osteoblast and Osteocyte Apoptosis: Challenges and Rewards. *JOURNAL OF BONE AND MINERAL RESEARCH*, **22**(10), 1492–1501.

Jorgensen, Niklas Rye, Teilmann, Stefan Cuoni, Henriksen, Zanne, Meier, Eddi, Hansen, Susanne Syberg, Jensen, Jens-Erik Beck, Sorensen, Ole Helmer, & Petersen, Jorgen Soberg. 2004. The Antiarrhythmic Peptide Analog Rotigaptide ZP123 Stimulates Gap Junction Intercellular Communication in Human Osteoblasts and Prevents Decrease in Femoral Trabecular Bone Strength in Ovariectomised Rats. *Endocrinology*, **146**(11), 4745–4754.

Khosla, Sundeep, & Hopbauer, Lorenz C. 2017. Osteoporosis treatment: recent developments and ongoing challenges. *LANCET DIABETES AND ENDICRINOLOGY*, **5**(11), 898–907.

Kimmel, Donald B, & Jee, Webster S S. 1980. A Quantitative Histologic Analysis of the Growing Long Bone Metaphysis. *Calcified Tissue International*, **32**, 113–122.

Komarova, Svetlana. 2006. Bone Remodeling in Health and Disease: Lessons From Mathematical Modeling. *New York Academy of Sciences*, **1068**, 557–559.

Komarova, Svetlana V. 2004. Mathematical Model of Paracrine Interactions Between Osteoclasts and Osteoblasts Predicts Anabolic Action of Parathyroid Hormone on Bone. *Endocrinology*, **1038**(8), 3689–3595.

Komarova, Svetlana V, Smith, Robert J, Dixon, S Jeffrey, Sims, Stephen M, & Wahl, Lindi M. 2003. Mathematical model predicts a critical role for osteoclast autocrine regulation in the control of bone remodeling. *Bone*, **33**, 206–215.

Kumar, Chanchal, Panigrahi, Inusha, Aradhya, Abhishek Somasekhara, Meena, Babu Lal, & Khandelwal, Niranjan. 2016. Zoledronic for Osteogenesis imperfecta: evaluation of safety profile in children. *JOURNAL OF PEDIATRIC ENDOCRINOLOGY AND METABOLISM*, **29**(8), 947–952.

Lane, Nancy E, Yao, Wei, Kinney, John H, Modin, Gunnard, Balooch, Mehdi, & Wronski, Thomas J. 2003. Both hPTH 1-34 and bFGF Increase Trabecular Bone Mass in Osteopenic Rats but They Have Different Effects on Trabecular Bone Architecture. *Journal of Bone and Mineral Research*, **18**(12), 2105–2115.

Lanyon, L E. 1993. Osteocytes, strain detection, bone modeling and remodeling. *Calcified Tissue International*, **53**, S102–S107.

Lemaire, Vincent, Tobin, Frank L, Grellar, Larry D, Cho, Carolyn R, & Suva, Larry. 2004. Modeling the interaction between osteoblast and osteoclast activities in bone remodeling. *Journal of Theoretical Biology*, **229**, 293–392.

Leppanen, Olli V, Sievanen, Harri, Jokihaara, Jarkko, Pajamaki, Ilari, Kannus, Pekka, Cooper, David M, & Jarvinen, Teppo L N. 2010. The effects of loading and estrogen on rat bone growth. *Journal of Applied Physiology*, **108**, 1737–1744.

Levenston, Marc E. 1997. TEMPORAL STABILITY OF NODE–BASED INTERNAL BONE ADAPTATION SIMULATIONS. *Journal of Biomechanics*, **30**(4), 403–407.

Li, M, & Wronski, T J. 1995. Response of Femoral Neck to Estrogen Depletion and Parathyroid Hormone in Aged Rats. *Bone*, **16**(5), 551–557.

Liu, X Sherry, Bevill, Grant, Keaveny, Tony M, Sajda, Paul, & Guo, X Edward. 2009. Micromechanical analyses of vertebral trabecular bone based on individual trabeculae segmentation of plates and rods. *Journal of Biomechanics*, **42**, 249–256.

loana Pastrama, Maria, Scheiner, Stefan, Pivonka, Peter, & Hellmich, Christian. 2018. A mathematical multiscale model of bone remodeling, accounting for pore space-specific mechanosensation. *BONE*, **107**, 208–221.

Lotinum, Sutada, Westerlind, Kim C, Kennedy, Angela M, & Turner, Russell T. 2003. Comparative effects of long-term continuous release of 16α-hydroxyestrone and 17β-estradiol on bone, uterus and serum cholesterol in ovariectomized adult rats. *Bone*, **33**, 124–131.

Lui, Julian C, Nilsson, Ola, & Baron, Jeffrey. 2014. Recent insights into the regulation of the growth plate. *Journal of Molecular Endocrinology*, **53**, T1–T9.

Lupion, Patricia M, Brun, Lucas R, & Loreto, Veronica E Di. 2018. ZOLEDRONIC ACID EFFECT ON BONE OF GROWING RATS. *ACTUALIZACIONES EN OSTEOLOGIA*, **14**(3), 168–177.

Malone, Amanda M D, Anderson, Charles T, Tummala, Padmaja, Kwon, Ronald Y, Johnston, Tyler R, Stearns, Time, & Jacobs, Christopher R. 2007. PrImary cilia mediate mechanosensing in bone cells by a calcium-independent mechanism. *Proceedings of the National Academy of Sciences in the United States of America*, **104**(33), 13325–13330.

Martin, Brianna L, & Bottema, Murk J. 2015. Textons for 3D Binary Data with Applications to Classifying Cancellous Bone. International Conference on Digital Image Computing: Techniques and Applications (DICTA).

Martin, M J, & Buckland-Wright, J C. 2004. Sensitivity analysis of a novel mathematical model identifies factors determining bone resorption rates. *Bone*, **35**, 918–928.

Martin, R B. 1985. The Usefulness of Mathematical Models for Bone Remodeling. *YEARBOOK OF PHYSICAL ANTRHOPOLOGY*, **28**, 227–236.

Martin, T John. 2008. Bone remodelling: its local regulation and the emergence of bone fragility. *Best Practice and Research Clinical Endocrinology and Metabolism*, **22**(5), 701–722.

Mastrogiacombo, M, Papadimitropolous, A, Cedola, A, Peyrin, F, Giannoni, P, Pearce, S G, Lini, M, Giannini, C, Guagliardi, A, & Cancedda, R. 2007. Engineering of bone using bone marrow stromal cells and a silicon–stabilized tricalcium phosphate bioceramic: Evidence for a coupling between bone formation and scaffold resorption. *Biomaterials*, **28**, 1376–1384.

Matsuo, Koichi, & Irie, Naoko. 2008. Osteoclast-osteoblast communication. *Archives of Biochemistry and Biophysics*.

Mi, L, Fritton, S, Basu, M, & Cowin, S. 2005. Analysis of avian bone response to mechanical loading - Part One: Distribution of bone fluid shear stress induced by bending and axial loading. *Biomechanics and Modeling in Mechanobiology*, **4**, 118–131.

Mizuhashi, K, Ono, W, Matsushita, Y, Sakagami, N, Takahashi, A, Saunders, T L, Nagasawa, T, Kronenberg, H M, & Ono, N. 2018. Resting zone of the growth plate houses a unique class of skeletal stem cells. *NATURE*, **563**(7730), 254–258.

Modi, Hitesh N, Suh, Seung Woo, Prjvc, Boopalan, Hong, Jae-Young, Yang, Jae-Hyuk, Park, Young-Hwan, Lee, Jae-Moon, & Kwon, Yong-Hyon. 2011. Bone quality and growth characteristics of growth plates following limb transplantation between animals of different ages - Results of experimental study in male syngeneic rats. *Journal of Orthopaedic Surery and Research*, **6**(53), 2–7.

Muderis, M Al, Azzopardi, T, & Cundy, P. 2007. Zebra Lines of Pamidronate Therapy in Children. *THE JOURNAL OF BONE AND JOINT SURGERY*, **89**, 1511–1516.

Mullender, M G, & Huiskes, R. 1997. Osteocytes and bone lining cells: which are the best candidates for mechano–sensors in cancellous bone? *Bone*, **20**, 527–532.

Mullender, M G, Huiskes, R, & Weinans, H. 1994. A physiological approach to the simulation of bone remodeling as a self–organizational control process. *Journal of Biomechanics*, **27**, 1389–1394.

Muller, R. 2005. Long–term prediction of three–dimensional bone architecture in simulations of pre–, peri– and post–menopausal microstructural bone remodeling. *Osteosis International*, **16**, S25–S35.

Nancollas, G H, Tang, R, Phipps, R J, Henneman, Z, Gulde, S, Wu, Mangood, A, Russell, R G G, & Ebetino, F H. 2005. Novel insights into actions of bisphosphonates on bone: Differences in interactions with hydroxyapatite. *Bone*, **5**, 617–627.

Narváez-Tovar, Carlos A, & garzon Alvarado, Diego A. 2012. Computational modeling of the mechanical modulation of the growth plate by sustained loading. *Theoretical Biology and Medical Modelling*, **9**(41).

Nishimori, S, Lai, F, Shiraishi, M, Kobayashi, T, Kozhemyakina, E, Yao, T P, Lassar, A B, & Kronenberg, H M. 2019. PTHrP targets HDAC4 and HDAC5 to repress chondrocyte hypertrophy. *JCI Insight*, **33**, 344–344.

Nyman, Jeffrey S, Yeh, Oscar C, Hazelwood, Scott J, & Martin, R Bruce. 2004. A theoretical analysis of long-term bishphosphonate effects on trabecular bone volume and microdamage. *Bone*, **35**, 296–305.

Odgren, Paul R, Witwicka, Hanna, & Gutierrez, Pablo Reyes. 2016. The cast of clasts: catabolism and vascular invasion during bone growth, repair and disease by osteoclasts, chondroclasts and septoclasts. *CONNECTIVE TISSUE RESEARCH*, **57**(3), 161–174.

Otsu, N. 1978. A threshold selection method from gray-scale histogram. *IEEE Trans Sys Man Cybern*, **8**, 62–66.

Parfit, A M. 2002. Targeted and Nontargeted Bone Remodeling: Relationship to Basic Multicellular Unit Origination and Progression. *Bone*, **30**(1), 5–7.

Parfitt, A M. 2002. Perspective. Misconceptions 2: Turnover Is Always Higher in Cancellous Than in Cortical Bone. *Bone*, **30**(6), 807–809.

Parfitt, A M, Mathews, C H E, Villanueva, A R, Kleerekoper, M, Frame, B, & Rao, D S. 1983. Relationships between Surface, Volume, and Thickness of Iliac Trabecular Bone in Aging and in Osteoporosis. *Journal for Clinical Investigation*, **72**, 1396–1409.

Parfitt, A Michael, Drezner, Marc K, Glorieux, Francis H, Kanis, John A, Malluche, Hartmut, Meunier, Pierre J, Ott, Susan M, & Recker, Robert R. 1987. Bone Histomorphometry: Standardisation of Nomenclature, Symbols, and Units. *Journal of Bone and Mineral Research*, **2**(6), 595–610.

Pataki, A, Muller, K, Green, J R, Ma, Y F, Li, Q N, & Jee, W S S. 1997. Effects of short-term treatment with the bisphosphonates zoledronate and pamidronate on rat bone: a comparative histomorphometric study on cancellous bone formed before and after treatment. *The Anatomical Record*, **249**, 458–468.

Perilli, Egon, Le, V, Ma, B, Salmon, P, Reynolds, K, & Fazzalari, N L. 2009. Detecting early bone changes using in vivo micro–CT in ovariectomized, zoledronic acid–treated, and sham–operated rats. *International Osteoporosis*, **21**, 1371–1382.

Perren, S M. 1979. Physical and biological aspects of fracture healing with special reference to internal fixation. *Clinical Orthopaedic Related Research*, **138**, 175–195.

Perry, Mark J, McDougall, Kathleen E, chen Hou, Shu, & Tobias, JOnathan H. 2008. Impaired growth plate funtion in bmp-6 null mice. *BONE*, **42**, 216–225.

Piekarski, K, & Munro, M. 1977. Transport mechanism operating between blood supply and osteocytes in long bones. *Nature*, **269**, 80–82.

Pivonka, Peter, & Komarova, Svetlana V. 2010. Mathematical modeling in bone biology: From intracellular signaling to tissue mechanics. *Bone*, **47**, 181–189.

Pivonka, Peter, Buenzli, Pascal, Scheiner, Stefan, Hellmich, Christian, & Dunstan, Colin R. 2013. The influence of bone surface availability in bone remodelling–A mathematical model including coupled geometrical and biomechanical regulations of bone cells. *Engineering Structures*, **47**, 134–147.

Prendergast, P J, Huiskes, R, & Soballe, K. 1997. Biophysical stimuli on cells during tissue differentiation at implant interfaces. *Journal of Biomechanics*, **30**, 539–648.

Ralte, Sarah, Khatri, Kamlesh, & Nagar, Mahindra. 2011. Short-term effects of zoledronic acid on the histomorphology of osteoclast in young albino rats. *Annals of Anatomy*, **193**, 509–515.

Rao, S H, Evans, K D, Oberbauer, A M, & Martin, R B. 2008. Bisphosphonate treatment in the *oim* mouse model alters bone modeling during growth. *Journal of Biomechanics*, **41**, 3371–3376.

Reed, A, Joyner, C J, Brownlow, H, & Simpson, A H R W. 2002. Human atrophic fracture non–unions are not avascular. *Journal of Orthopaedic Research*, **20**, 593–599.

Reginster, Jean-Yves, Collette, Julien, Neruprex, Audrew, Zegels, Brigitte, Deroisy, Rita, & Bruyere, Oliver. 2007. Role of biochemical markers of bone turnover as prognostic indicator of successful osteoporosis therapy. *Bone*, **42**, 832–836.

Reitsma, P H, Bijvoet, O L M, Verlinden-Ooms, H, & van der Wee-Pals, L J A. 1980. Kinetic studies of bone and mineral metabolism during treatment with (3-amino-1-hydroxylpropylidene)-1, 1-bisphosphonate (APD) in rats. *Cacified Tissue International*, **32**, 145–157.

Rezende, Eloiza, Bradaschia-Correa, Vivian, Siviero, Fabio, Ambrosio, Lucas M B, & Arana-Chavez, Victor E. 2017. Effects of bisphosphonates on osteogenesis and osteoclastogenesis signaling during the endochondrol ossification of growing rats. *Cell and Tissue Research*, **368**(2), 287–300.

Riggs, B Lawrence, & Parfitt, A Michael. 2005. Perspective. Drugs Used to Treat Osteoporosis: The Critical Need for a Uniform Nomenclature Based on Their Action on Bone Remodeling. *JOURNAL OF BONE AND MINERAL RESEARCH*, **20**(16), 177–184.

Roach, Helmtrud I, Mehta, Gautam, Oreffo, Richard O C, Clarke, Nicholas M P, & Cooper, Cyrus. 2003. Temporal anaylisis of rat growth plates: cessation of growth with age despite presence of physis. *The Journal of Histochemistry and Cytochemistry*, **51**(3), 373–383.

Ruimerman, R, Hilbers, P, van Rietbergen, B, & Huiskes, R. 2005. A theoretical framework for strain–related trabecular bone maintenance and adaptation. *Journal of Biomechanics*, **38**, 931–941.

Russell, R G G, Watts, N B, Ebetino, F H, & Rogers, M J. 2008. Mechanisms of action of bisphosphonates: similarities and differences and their potential influence on clinical efficacy. *Osteoporosis International*, **19**, 733–759.

Ryser, Marc D, Komarova, Svletlana V, & Nigam, Nilma. 2010. THE CELLULAR DYNAMICS OF BONE REMODELLING: A MATHEMATICAL MODEL. *Society for Industrial and Applied Mathematics*, **70**, 1899–1921.

Scheiner, S, Theoval, A, Pivonka, P, Smith, D W, & Bonewald, L F. 2010. Investigation of nutrient transport mechanisms in the lacunae-canaliculi system. *IOP Conf. Series: Materials Science and Engineering*, **10**.

Scheiner, Stefan, Pivonka, Peter, & Hellmich, Christian. 2013. Coupling systems biology with multiscale mechanics, for computer simulations of bone remodeling. *INTERNATIONAL JOURNAL FOR NUMERICAL METHODS IN BIOMEDICAL ENGINEERING*, **29**, 1307–1322.

Schenk, R, Merz, W A, Muhlbauer, R, Russell, R G, & Fleisch, H. 1973. Effext of ethane-1-hydroxy-1, 1-diphosphonate (EHDP) AND DICHLOROMETHYLENE DIPHOSPHONATE (CL_2MDP) on the calcification and resorption of cartilage and bone in the tibial epiphysis and metaphysis of rats. *Cacified Tissue International*, **11**, 196–214.

Schenk, R, Eggli, P, Fleisch, H, & Rosini, S. 1986. Quantitative morphometric evaluation of the inhibitory activity of new aminobisphosphonates on bone resorption in the rat. *Calcified Tissue International*, **38**, 342–349.

Schulte, F A, Zwahlen, A, Lambers, F M, Kuhn, G, Ruffoni, D, Betts, D, Webster, D J, & Mueller, R. 2013. Strain-adaptive in silico modeling of bone adaptation - A computer simulartion validated by in vivo micro-computed tomography data. *BONE*, **52**(1), 475–492.

Seeman, E. 2003. Periosteal bone formation: A neglected determinant of bone strength. *N Eng J Med*, **349**, 320–323.

Seeman, E. 2008. Structural basis of growth-related gain and age-related loss of bone strength. *Rheumatology*, **47**, iv2–iv8.

Seeman, Ego. 2009. To stop or not to stop, that is the question. *Osteoporosis International*, **20**, 187–195.

Seeman, Ego, & Delmas, Pierre D. 2006. Bone Quality - the Material and Structural Basis of Bone Strength and Fragility. *New England Journal of Medicine*, **354**(21), 2250–2261.

Seeman, Ego, & Martin, T J. 2019. Antiresorptive and anabolic agents in the prevention and reversal of bone fragility. *NATURE REVIEWS RHEUMATOLOGY*, **15**(4), 225–236.

Serra, Jean. 1982. *Image Analysis and Mathematical Morphology*. Academic Press.

She, Guorong, Zhou, Ziqi, Zha, Zhengang, Wang, Fei, & Pan, Xiaoting. 2017. Protective effect of zoledronic acid on articular cartilage and subchondral bone of rabbits with experimental knee arthritis. *EXPERIMENTAL AND THERAPEUTIC MEDICIN*, **14**(4), 4901–4909.

Shefelbine, S J, Augat, P, Claes, L, & Simon, U. 2005. Trabecular bone fracture healing simulation with finite element analysis and fuzzy logic. *Journal of Biomechanics*, **38**, 2440–2450.

Shirai, T, Kobayashi, M, Nishitani, K, Satake, T, Kuroki, H, Nakagawa, Y, & Nakamura, T. 2011. Chondroprotective effect of alendronate in a rabbit model of osteoarthritis. *Journal of Orthapaedic Research*, **29**, 1572–1577.

SIFFERT, R S, LUO, G M, COWIN, S C, & KAUFMAN, J J. 1996. Dynamic Relationships of Trabecular Bone Density, Architecutre,and Strength in a Computational Model of Osteopenia. *Bone*, **18**(2), 197–206.

Silverman, Stuart L. 2011. Bisphosphonate use in conditions other than osteoporosis. *ANNALS OF THE NEW YORK ACADEMY OF SCIENCES*, **1218**, 33–37.

Stevens, Sheila S, & Beaupré, Gary S. 1999. Computer Model of Endochondral Growth and Ossification in Long Bones: Biological and Mechanobiological Influences. *Journal of Orthopaedic Research*, **6**, 148–154.

Stevens, Sheila S, Beaupré, Gary S, & Carter, D R. 1999. Mechanical Stresses and Endochondral Ossification in the Chrondoepiphysis. *Journal of Orthopaedic Research*, **17**, 615–653.

Stokes, Ian A F, Aronsson, David D, Dimock, Abigail N, Cortright, Valerie, & Beck, Samantha. 2006. Endochondral Growth in Growth Plates of Three Species at Two Anatomical Locations Modulated by Mechanical Compression and Tension. *Journal of Orthopaedic Research*, **24**, 1327–1334.

Stulpner, M A, Reddy, B D, Starke, G R, & Spirakist, A. 1997. A THREE–DIMENSIONAL FINITE ELEMENT ANALYSIS OF ADAPTIVE REMODELLING IN THE PROXIMAL FEMUR. *Journal of Biomechanics*, **30**(10), 1063–1066.

Szule, P, & Seeman, E. 2009. Thinking inside and outside the envelopes of bone. *Osteoporosis International*, **20**, 1281–1288.

Tayyar, S, Wienhold, P S, Butler, R A, Woodard, J C, Zardiackas, L D, John, K R St, Bedsoe, J M, & Gilbert, J A. 1999. Computer simulation of trabecular remodeling using a simplified structural model. *Bone*, **25**, 733–739.

Teitelbaum, Steven L. 2000. Bone Resorption by Osteoclats. *SCIENCE*, **289**, 1504–1508.

Tenta, Roxane, Sourla, Antigone, Lembessis, Peter, & Koutsilieris, Michael. 2006. Bone-related growth factors and zoledronic acid regulate PTHrp/PTH.1

receptor bioregulation systems in MG-63 human osteosarcoma cells. *ANTICANCER RESEARCH*, **26**, 283–292.

Tkachenko, Evgeniy, Slyfield, Craig R, Tomlinson, Ryan E, Daggett, Justin R, Wilson, David L, & Hernandez, Christopher John. 2009. Voxel size and measures of individual resorption cavities in three–dimensional images of cancellous bone. *Bone*, **45**, 487–492.

Touaitahuata, HeianI, Cres, Gaelle, de Rossi, Sylvain, Vives, Virginie, & Blangy, Anne. 2014. The mineral dissolution function of osteoclasts is dispensible for hypertrophic cartilage degredation during long bone development. *Developmental Biology*, **393**, 57–70.

Trichilo, Silvia, Scheiner, Stefan, Forwood, Mark, Cooper, David M L, & Pivonka, Peter. 2019. Computational model of the dual action of PTH- Application to a rat model of osteoporosis. *Journal of Theoretical Biology*, **473**, 67–79.

Tsang, Kwok Yeung, Chan, Danny, & Cheah, Kathryn S E. 2015. Fate of growth plate hypertrophic chondrocytes: death or lineage extension? *Developmental Growth and Differentiation*, **57**, 179–192.

Tsangari, Helen, Findlay, David M, Zannettino, Andrew C W, Pan, Beiquing, Kuliwaba, Julia S, & Fazzalari, Nicola L. 2006. Evidence for reduced bone formation surface relative to bone resorption surface in female femoral fragility fracture patients. *Bone*, **39**, 1226–1235.

Turner, C H. 1999. Toward a mathematical description of bone biology: The principle of cellular accommodation. *Calcified Tissue International*, **65**, 466–471.

Väänänen, H Kalervo, Zhao, Haibo, Mulari, Mika, & Halleen, Jussi M. 2000. The cell biology of osteoclast function. *Journal of Cell Science*, **113**, 377–381.

van der Meulen, Marjolein C H, Morgan, Timothy G, Yang, Xu, Baldini, Todd H, Myers, Elizabeth R, Wright, Timoth M, & Bostrom, Mathias P G. 2006. Cancellous bone adaptation to in vivo loading in a rabbit model. *Bone*, **38**, 871–877.

van Oers, Rene F M, Ruimerman, Ronald, Tanck, Esther, Hilbers, Peter A J, & Huiskes, Rik. 2007. A unified theory for osteonal and hemi-osteonal remodeling. *Bone*, **42**, 250–259.

Visekruna, M, Wilson, D, McKiernan, F E, & Eoin, F. 2008. Severely suppressed bone turnover and atypical skeletal fragility. *JOURNAL OF CLINICAL ENDOCRINOLOGY AND METABOLISM*, **93**(8), 2948–2952.

Štěpán, J J, Pospíchal, J, Prezl, J, & Pacovský, V. 1987. Bone Loss and Biochemical Indices of Bone Remodeling in Surgically Induced Postmenopausal Women. *Bone*, **8**, 279–284.

Walzer, S M, Cetin, E, Grubl-Brabas, R, Sulzbacher, I, Rueger, B, Girsch, W, Toegal, S, Windhager, R, & Fischer, M B. 2014. Vascularisation of primary and secondary ossification centres in the human growth plate. *BMC DEVELOPMENTAL BIOLOGY*, **14**(36), 14–36.

Wang, Yan, Pivonka, Peter, Buenzli, Pascal R, Smith, David W, & Dunstan, Colin R. 2011. Comutational Modelling of Iinteractions between Mmultiple Myeloma and the Bone Microenvironment. *PLOS one*, **6**.

Weber, M H, Sharp, J C, Hassard, T H, & Orr, F W. 2002. Normal murine bone morphometry: A comparison of magnetic resonance microscopy with micro X–ray and histology. *Skeletal Radiology*, **31**, 282–291.

Weinan, H, & GRootenboer, R Huiskes H. 1992. The behavior of adaptive bone-remodeling simulation models. *Journal of Biomechanics*, **25**, 1424–1441.

Weinbaum, S, Crown, S C, & Zeng, Yu. 1994. A MODEL FOR THE EXCITATION OF OSTEOCYTES BY MECHANICAL LOADING-INDUCED BONE FLUID SHEAR STRESSES. *Journal of Biomechanics*, **27**(3), 339–360.

Wilsman, Norman J, Farnum, Cornelia E, Leiferman, Ellen M, Fri, Michael, & Barreto, C. 1996. Differential Growth by Growth Plates as a Function of Multiple Parameters of Chrondocytic Kinetics. *Journal of Orthapaedic Research*, **14**, 927–936.

Wimpenney, David Ian, & Moroz, Adam. 2006. On allosteric control model of bone turnover cycle containing osteocyte regulation loop. *BioSystems*, **90**, 295–308.

Wronski, T J, & Liang, H. 1999. Effects of Age, Estrogen Depletion, and Parathyroid Hormone Treatment on Vertebral Cancellous Wall Width in Female Rats. *Bone*, **25**(4), 465–468.

Wronski, T J, Dann, L M, & Horner, S L. 1989. Time Course of Vertebral Osteopenia in Ovariectomised Rats. *Bone*, **10**, 296–301.

Xian, Cory. 2014. Regulation, bone growth defects, and potential treatments. *Journal for Molecular Endocrinology*, **53**, E1–E2.

Xu, Xiao-Long, Gou, Wen-Lon, Wang, Ai-Yuan, Wang, Yu, Guo, Quan-Yi, Lu, Qiang, Lu, Shi-Bi, & Peng, Jiang. 2013. Basic resarch and clinical application of bisphosphonates in bone disease: what have we learned over the last 40 years? *Journal of Translational Medicin*, **11**(303).

Yau, Wei, Balooch, Guive, Balooch, Mehdi, Jiang, Yebin, Nalla, Ravi K, Kinney, John, Wronski, Thomas J, & Lane, Nancy E. 2006. Sequential treatment of ovariectomized mice with bFGF and risedronate restored trabecular bone microarchitecture and mineralization. *Bone*, **39**, 460–469.

Young, D R, Niklowitz, W J, Brown, R J, & Jee, W S S. 1986. Immobilization – associated Osteoporosis in Primates. *Bone*, **7**, 109–117.

Appendix A

Data supplementary

A.1 Animal handling of inherited data

The data for this study were inherited in the form of rat tibial reconstructed μCT scans. Originally the rats were purchased from Adelaide University, weighing approximately 200g and housed three to four per cage and exposed to 12 hour light/12 hour dark cycle at constant temperature 23 ± 1^0C. After one week of acclimatisation the animals were anaesthetized with a peritoneal injection of ketamine/xylaxin (1ml/100g) and underwent scanning before assignment into the three experimental groups. All animals were treated according to the Australian code of practice for the care and use of animals for scientific purposes with the approval from the National Health and Research Council of Australia. The animals were provided ad libitum access to tap water and standard rat chow (19% protein, 0.67% phosphorous, 0.78% calcium, and 2000 IU/kg vitamin D).

A.2 μCT procedures

The overectomies and sham ovariectomy were performed after initial scanning at $t = 0$ and the ovx+zol animals started weekly treatment with bisphosphonate Zoledronic acid (Zometa, Novartis, Basel, Switzerland) in the peritoneal cavity (1.6μg/kg) at $t = 14$. At

the time of Zoledronic treatment, sham and ovx animals received the equivalent volume of saline injections. Each rat underwent in vivo μ-CT scanning of the right hind limb (Skyscan model 1076, Skyscan, Kontich, Belgium) at $t = 0, 14, 28, 56, 84$. Due to an adverse reaction to the aesthetic two sham rats died before the final scan at $t = 84$, and one ovx+zol rat died before $t = 84$ from necrotised toes in the right foot.

Acquisition settings, scanning procedures, and reconstruction methods were as reported in (Perilli *et al.* , 2009). In summary, the scan settings were as follows: the X-ray source was 74kVp and 100mA; the rotation step 0.8^o ; the scanning width: 35mm; the pixel size: 8.702μm; the filter was AL 1mm; and the scanning duration was 20 minutes per rat. The raw data were reconstructed using standard software Nrecon (Skyscan, Belgium).

A.2.1 Limitations of the data

The following discrepancies during the experimental procedures may have affected the quality of the data.

- The rats were not weighed. The rats were said to weigh 'roughly 200g' upon arrival. According to The University of Adelaide Laboratory Animal services, the average weight of female Sprague Dawley rats, at week 8 is 196.8 g, with a range 175 - 220 g. The increasing weight of rats was not taken into account for dosages of Zoledronic acid or anaesthetic (Xylazine/Ketimine), nor were there adjustments made for individual rats.
- The rats received 'weekly injections' though not always at the same time or on the same day each week.
- The changing bone lengths over time were not available.
- Histological procedures were never carried out.
- Only 300 μCT slices available for one of the ovx rats at $t = 0$, in the proximal region of the bone block.
- Biomarkers were not measured.

A.3 Preliminary observations supplementaries

P-values should be used as indications only, since sample sizes were too small to obtain values with confidence.

P-values comparing group m values in $B_{r,t}(x) = mx + b$					
	$t = 0$	$t = 14$	$t = 28$	$t = 56$	$t = 84$
(a)	0.097 ($N_1, N_2 = 10, 9$)	0.137 (N = 19)	0.072 (N = 20)	0.1209 (N = 20)	0.062 (N = 18)
(b)	0.104 (N = 20)	0.501 (N = 20)			
(c)	0.068 (N = 19)	0.112 (N = 20)			
(d)	0.101 (N = 30)	0.083 (N = 30)			

Table A.1: P-values for testing the null hypothesis that values of m found for linear fits to $B_{r,t}(x) = mx + b$ are the same for sham and ovx groups for $t \geq 0$ and for ovx+zol for $t = 0, 14$. P-values presented for t-tests between the following groups: (a) group 1 (G1) = sham, group 2 (G2) = ovx; (b) G1 = sham, G2 = ovx+zol; (c) G1 = ovx, G2 = ovx+zol; and (d) G1 = pooled m values of both sham and ovx groups, G1 = ovx+zol.

Figure A.1: Bone blocks at $t = 0, 14, 28, 56, 84$ for a single sham rat (column 1); a single ovx rat (column 2); and a single ovx+zol rat (column 3).

	P-values comparing group averages of additive constants $b_{r,t}$							
	t		14		28		56		84
sham	0	(a)	0.048	(b)	0.066	(c)	0.024	(d)	0.066
	2			(e)	0.986	(f)	0.656	(g)	0.786
	4					(h)	0.689	(i)	0.807
	8							(j)	0.914
ovx	0	(a)	0.001	(b)	<0.001	(c)	<0.001	(d)	<0.001
	2			(e)	0.016	(f)	<0.001	(g)	<0.001
	4					(g)	0.097	(i)	0.016
	8							(j)	0.370

Table A.2: P-values for testing the null hypothesis that group additive constants $b_{r,t}$ for Model 2.2 do not change over time for sham and ovx rats. P-values are presented for group average additive constants between time points t (a) 0 and 14; (b) 0 and 28; (c) 0 and 56; (d) 0 and 84; (e) 14 and 28; (f) 14 and 56; (g) 14 and 84; (h) 28 and 56, (i) 28 and 84; and (j) 56 and 84.

Appendix B

Mathematical modelling supplementary

B.1 Prior work: ODE temporal model

For equation 3.1, 18 models were considered with $c(B)$ and $f(B)$ each being linearly dependent on $B(t)$ or BS/TV, or independent of the amount of bone present; and also for $f(B)$ having independence on the number of remodelling cites per unit time for current B.

Three models for $c(B)$ were considered,

$$c(B) = C, \quad c(B) = CB, \quad c(B) = CKB^{2/3},$$

representing independence of the amount of bone present (dependence on tissue volume only); linear dependence on BV/TV, B; and linear dependence on the specific area $BS/TV = KB^{2/3}$. In each of these three models, C is a proportionality constant, but varies both numerically, and in units between the three models.

Similarly, three models for average formation volume were considered

$$f(B) = F \quad f(B) = FB \quad f(B) = FKB^{2/3}.$$

In these three models, formation volume is modelled as independent of the cycle rate. A further three variants were considered to include possible dependence on the number of

remodelling cites per unit time for current BV/TV, B.

$$f(B) = \frac{F}{c(B)} \quad f(B) = \frac{FB}{c(B)} \quad f(B) = \frac{FKB^{2/3}}{c(B)}.$$

Only three models predict convergence of $B(t)$ to finite positive values,

$$\frac{dB}{dt} = F_t - C_v RB \tag{B.1}$$
$$\frac{dB}{dt} = F_t - C_s RKB^{2/3} \tag{B.2}$$
$$\frac{dB}{dt} = F_s KB^{2/3} - C_v RB \tag{B.3}$$

For this work, $c(B), f(B)$ and R were determined for each group and the results were very similar across the 3 models. The results indicate that the effect of ovx is increased R compared to the sham group and also increased $c(B)$ which is in agreement with the literature. Results for the effect of ovx+zol indicate a slight increase in the ratio of $f(B) : R$ per event compared to the sham group which is in accordance with the literature. However for ovx+zol, both R and $f(B)$ decreased compared to the sham group, and $c(B)$ increased, where these three effects are not in agreement with the current understanding of bisphosphonates.

B.2 Derivation of the model for BV/TV

With the same criterion as in section 3.1, only models that predict $B(x,t)$ to converge to a finite positive value for fixed t were considered further. Again, this criterion reduced the number of possible models to three, each as presented as a PDE, each in the region $\Omega = \{(x,t)|x \geq 1.2mm, t \geq 0\}$.

$$B_t + vB_x = F_t - C_v RB \tag{B.4}$$
$$B_t + vB_x = F_t - C_s RKB^{2/3} \tag{B.5}$$
$$B_t + vB_x = F_s KB^{2/3} - C_v RB \tag{B.6}$$

Here $C_v = \frac{events/tissue\ volume}{bone\ volume\ fraction \times \text{day}}$ in units (events$mm^{-3}day^{-1}$) from $c(B) = C_v B(t)$ where the cycle rate is proportional to the density of bone; $C_s = \frac{events/tissue\ volume}{total\ surface \times day}$ in units (events $mm^{-2}day^{-1}$) from $c(B) = C_s K B^{2/3}(t)$ where the cycle rate is proportional to the bone surface area, $F_t = \frac{average\ formation\ volume}{tissue\ volume}$ in units (day^{-1}) from $f(B) = \frac{F}{c(B)}$ where the average formation is not dependent on either bone density or surface area; and $F_s = \frac{average\ formation\ volume}{total\ surface\ area}$ in units ($mmday^{-1}$) from $f(B) = \frac{F_s K B^{2/3}(t)}{c(B)}$ where $f(B)$ is dependent on the surface area of the bone and the cycle rate.

For work carried out by (Fazzalari *et al.* , 2012), ODE results indicated that of the three models, no particular model stood out as being 'better' than the others. Thus Model B.4 was used for the chosen for further work. The model for BV/TV becomes

$$\begin{aligned} \frac{1}{v}B_t + B_x &= \frac{1}{v}(F - CRB(t)) && \text{(B.7)} \\ B(0,t) &= D(t) && \text{(B.8)} \end{aligned}$$

$$\begin{aligned} C(t) &= \frac{C_1 + C_3}{2} + \frac{C_2 - C_1}{2}\tanh\left(\lambda_1(t - J_1)\right) \\ &\quad + \frac{C_3 - C_2}{2}\tanh\left(\lambda_2(t - J_2)\right) && \text{(B.9)} \\ D(t) &= \frac{D_2 + D_1}{2} + \frac{D_2 - D_1}{2}\tanh\left(\eta(t - K)\right). && \text{(B.10)} \end{aligned}$$

The following constants are introduced to reduce the notation

$$A = \frac{F}{v}, \quad P = \frac{R(C_1 + C_3)}{2v}, \quad Q_1 = \frac{R(C_2 - C_1)}{2v}, \quad Q_2 = \frac{R(C_3 - C_2)}{2v}.$$

The PDE becomes

$$\begin{aligned} \frac{1}{v}B_t + B_x &= A - PB + \left(Q_1\tanh\left(\lambda_1(t - J_1)\right)\right)B \\ &\quad \left(Q_2\tanh\left(\lambda_2(t - J_2)\right)\right)B, && \text{(B.11)} \\ B(0,t) &= D(t) && \text{(B.12)} \end{aligned}$$

The solution curve in R^3 denoted by $(x(s), t(s), B(x(s), t(s)))$. Setting $z(s) = B(x(s), t(s))$, and choosing the parameter s such that $z(0) = D(r)$ and taking the derivatives with respect to s,

$$\frac{dz}{ds} = \frac{dz}{dt}\frac{dt}{ds} + \frac{dz}{dx}\frac{dx}{ds}$$

so (B.11) is resolved into three ODE initial value problems

$$\frac{dt}{ds}(s) = \frac{1}{v}, \quad t(0) = r \tag{B.13}$$

$$\frac{dx}{ds}(s) = 0, \quad x(0) = 0 \tag{B.14}$$

$$\frac{dz}{ds}(s) = A - (P + Q_1 \tanh(\lambda_1(t - J_1)) + Q_2 \tanh(\lambda_2(t - J_2)))\, z, \tag{B.15}$$

$$z(0) = D(r) \tag{B.16}$$

Solutions to (B.13), (B.14) are

$$x = s, \quad t = \frac{s}{v} + r. \tag{B.17}$$

Substituting (B.17) in (B.15) to get

$$\frac{dz}{ds}(s) = A - (P + Q_1 \tanh(\lambda_1(s/v + r - J_1)) + Q_2 \tanh(\lambda_2(s/v + r - J_2)))\, z,$$
$$z(0) = D(r) \tag{B.18}$$

To solve (B.18), set

$$g(s, r) = P + Q_1 \tanh(\lambda_1(s/v + r - J_1)) + Q_2 \tanh(\lambda_2(s/v + r - J_2)) \tag{B.19}$$

(B.18) becomes

$$\frac{dz}{ds} + g(s, r)z = A, \quad z(0) = D(r), \tag{B.20}$$

a linear first order IVP. Set

$$G(s, r) = Ps + \frac{Q_1 v}{\lambda_1} \ln\left(e^{\lambda_1(s/v + r - J_1)} + e^{-\lambda_1(s/v + r - J_1)}\right)$$
$$+ \frac{Q_2 v}{\lambda_2} \ln\left(e^{\lambda_2(s/v + r - J_2)} + e^{-\lambda_2(s/v + r - J_2)}\right), \tag{B.21}$$

where$G'(s, r) = g(s, r)$. Thus

$$\begin{aligned} \frac{d}{ds} z e^{G(s,r)} &= \frac{dz}{ds} \cdot e^{G(s,r)} + z \cdot g(s, r) e^{G(s,r)}. \\ &= e^{G(s,r)} \left(\frac{dz}{ds} + g(s, r)z\right) \\ &= A e^{G(s,r)} \end{aligned}$$

Hence

$$ze^{G(s,r)} = H + A\int_0^s e^{G(w)}dw$$

and by initial conditions at $s = 0$ where $z(0) = D(r)$, $H = D(r)e^{G(0,r)}$. Thus

$$z(s) = D(r)e^{G(0,r)-G(s,r)} + e^{-G(s,r)}A\int_0^s e^{G(w)}dw. \tag{B.22}$$

From (B.22)

$$e^{G(s,r)} = e^{Ps}\left(e^{\lambda_1(s/v+r-J_1)} + e^{-\lambda_1(s/v+r-J_1)}\right)^{Q_1v/\lambda_1}\left(e^{\lambda_2(s/v+r-J_2)} + e^{-\lambda_2(s/v+r-J_2)}\right)^{Q_{2v}/\lambda_2}.$$

Substituting $y = {}^{w}/_{v} + r$, the integral in (B.22), $\int_0^s e^{G(w,s)}dw$, becomes

$$\begin{aligned}
&\int_0^s e^{Pw}\left(e^{\lambda_1(w/v+r-J_1)} + e^{-\lambda_1(w/v+r-J_1)}\right)^{Q_1v/\lambda_1}\left(e^{\lambda_2(w/v+r-J_2)} + e^{-\lambda_2(w/v+r-J_2)}\right)^{Q_{2v}/\lambda_2}dw\\
=\ &\int_0^s e^{P(vy-vr)}\left(e^{\lambda_1(y-J_1)} + e^{-\lambda_1(y-J_1)}\right)^{Q_1v/\lambda_1}\left(e^{\lambda_2(y-J_2)} + e^{-\lambda_2(y-J_2)}\right)^{Q_{2v}/\lambda_2}dy\\
=\ &v\int_r^{s/v+r} e^{P(vy-vr)}\left(e^{\lambda_1(y-J_1)} + e^{-\lambda_1(y-J_1)}\right)^{Q_1v/\lambda_1}\left(e^{\lambda_2(y-J_2)} + e^{-\lambda_2(y-J_2)}\right)^{Q_{2v}/\lambda_2}dy\\
=\ &ve^{-Pvr}\int_r^{s/v+r} e^{Pvy}\left(e^{\lambda_1(y-J_1)} + e^{-\lambda_1(y-J_1)}\right)^{Q_1v/\lambda_1}\left(e^{\lambda_2(y-J_2)} + e^{-\lambda_2(y-J_2)}\right)^{Q_{2v}/\lambda_2}dy
\end{aligned}$$

From (B.22), $e^{-G(s,r)}A\int_0^s e^{G(w,s)}dw$ becomes

$$\begin{aligned}
&e^{-G(s,r)}Ave^{-Pvr}\int_r^{s/v+r} e^{Pvy}\left(e^{\lambda_1(y-J_1)} + e^{-\lambda_1(y-J_1)}\right)^{Q_1v/\lambda_1}\left(e^{\lambda_2(y-J_2)} + e^{-\lambda_2(y-J_2)}\right)^{Q_{2v}/\lambda_2}dy\\
&= \mathrm{Ave}^{-(Ps+Pvr)}\int_r^{s/v+r} e^{Pvy}\left(e^{\lambda_1(y-J_1)} + e^{-\lambda_1(y-J_1)}\right)^{Q_1v/\lambda_1}\left(e^{\lambda_2(y-J_2)} + e^{-\lambda_2(y-J_2)}\right)^{Q_{2v}/\lambda_2}\mathrm{dy}\\
&= \frac{Ave^{-Pv(s/v+r)}\int_r^{s/v+r} e^{Pvy}\left(e^{\lambda_1(y-J_1)} + e^{-\lambda_1(y-J_1)}\right)^{Q_1v/\lambda_1}\left(e^{\lambda_2(y-J_2)} + e^{-\lambda_2(y-J_2)}\right)^{Q_{2v}/\lambda_2}dy}{\left(e^{\lambda_1(t-J_1)} + e^{-\lambda_1(t-J_1)}\right)^{Q_1v/\lambda_1}\left(e^{\lambda_2(t-J_2)} + e^{-\lambda_2(t-J_2)}\right)^{Q_{2v}/\lambda_2}}
\end{aligned}$$

The complete solution is presented in Chapter 3.

Appendix C

Results supplementary

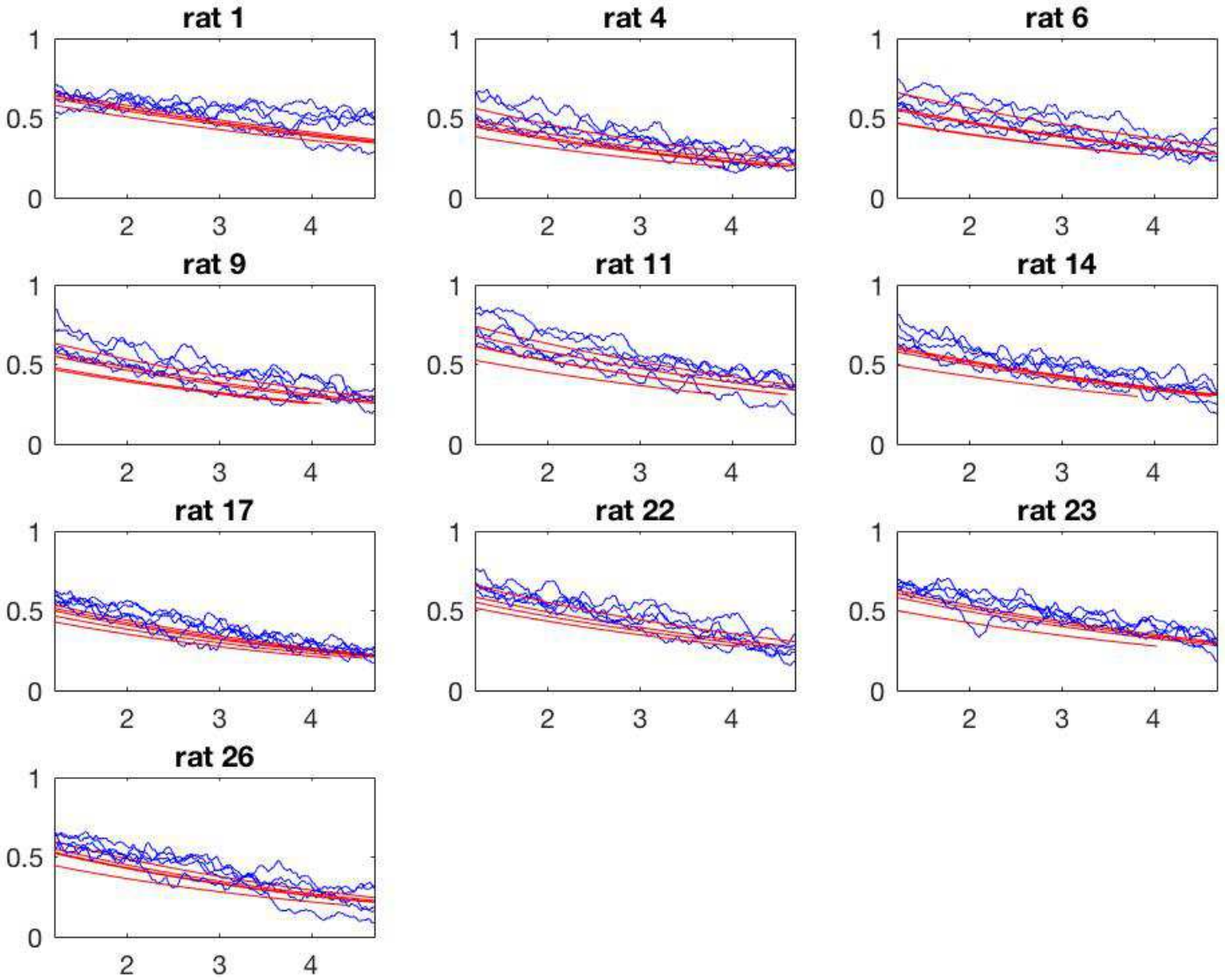

Figure C.1: Model for $B(x,t)$ for sham rats with initial conditions $s = 0.1$. Each figure shows the BV/TV values against distance from the growth plate for each $t = 0, 14, 28, 56, 84$ for an individual rat from the sham group (blue) plus the model for $B(x,t)$ superimposed (red) for each $t = 0, 14, 28, 56, 84$. Parameter values are set to $s = 0.1$, and $J_1 = 0, J_2 = 14, K = 14$.

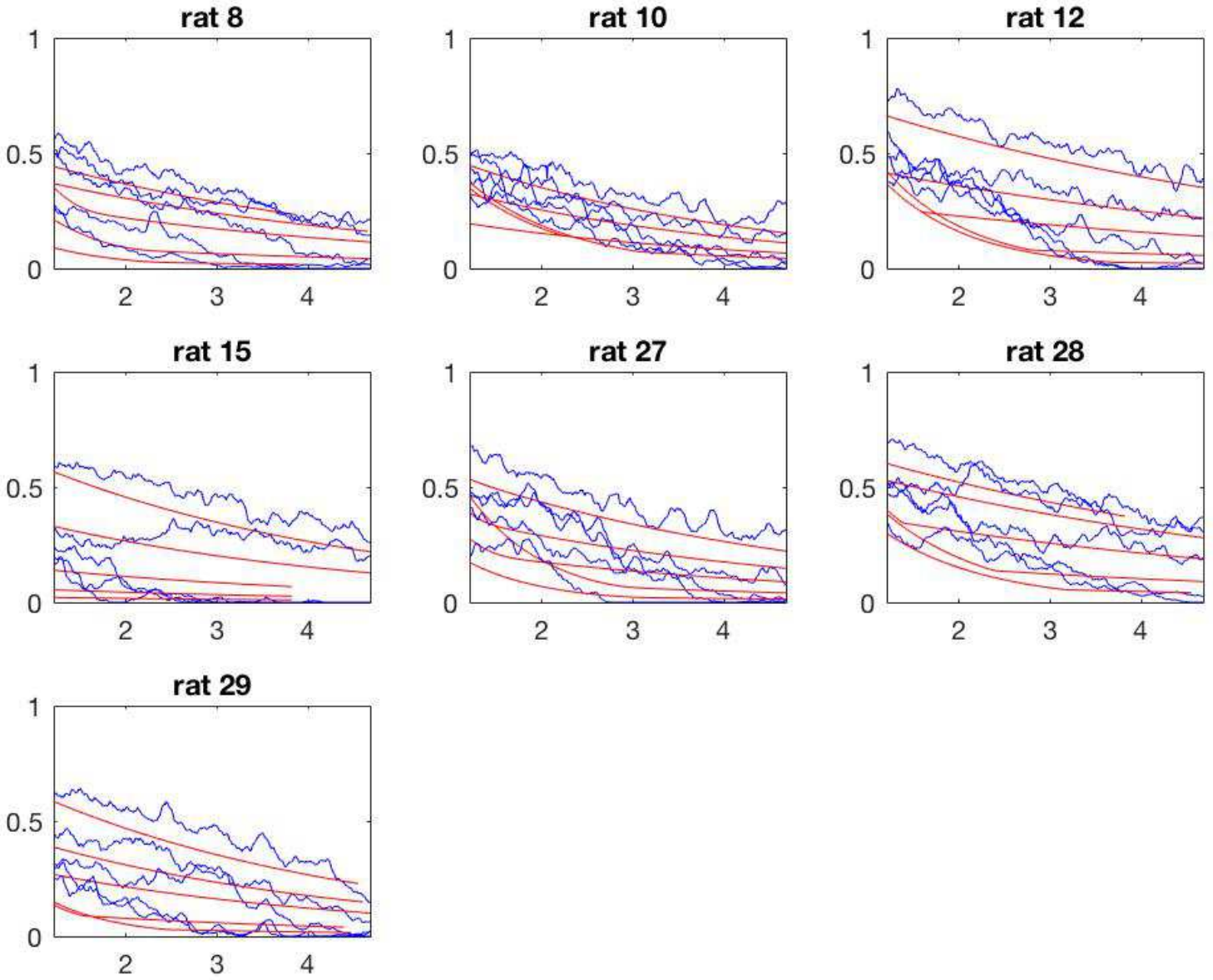

Figure C.2: Model for $B(x,t)$ for ovx rats with initial conditions $s = 0.1$. Each figure shows the BV/TV values against distance from the growth plate for each $t = 0, 14, 28, 56, 84$ for an individual rat from the ovx group (blue) plus the model for $B(x,t)$ superimposed (red) for each $t = 0, 14, 28, 56, 84$. Parameter values are set to $s = 0.1$, and $J_1 = 0, J_2 = 14, K = 14$.

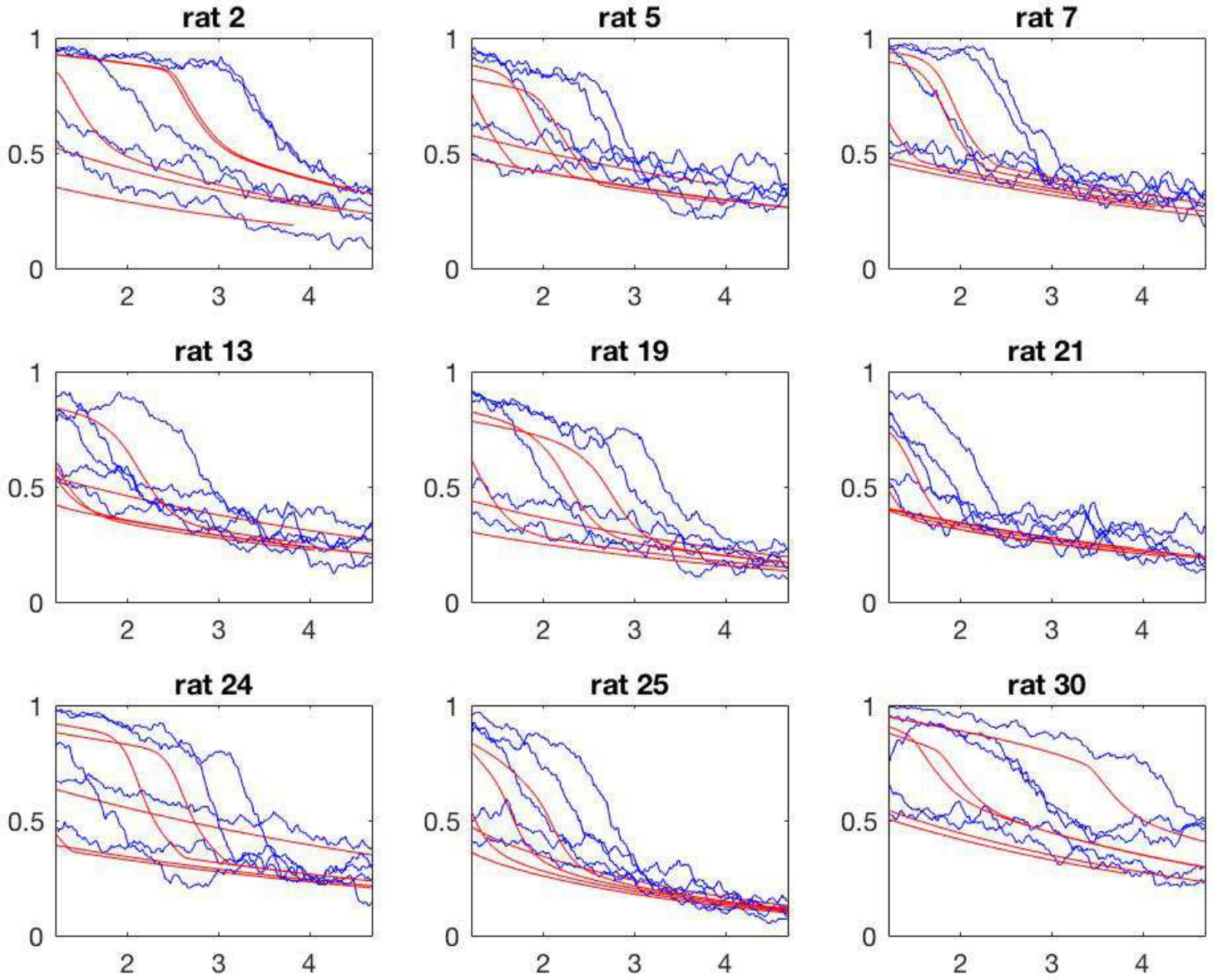

Figure C.3: Model for $B(x,t)$ for ovx+zol rats with initial conditions $s = 0.1$. Each figure shows the BV/TV values against distance from the growth plate for each $t = 0, 14, 28, 56, 84$ for an individual rat from the ovx+zol group (blue) plus the model for $B(x,t)$ superimposed (red) for each $t = 0, 14, 28, 56, 84$. Parameter values are set to $s = 0.1$, and $J_1 = 0, J_2 = 14, K = 14$.

	Rat ID (n = 10)										
Parameter	1	4	6	9	11	14	17	22	23	26	
v	0.0380	0.0260	0.0340	0.0320	0.0340	0.0360	0.0340	0.0380	0.0320	0.0280	
S_1	0.0065	0.0065	0.0067	0.0069	0.0067	0.0069	0.0085	0.0083	0.0067	0.0072	
D_1	0.7278	0.5944	0.6833	0.6833	0.7722	0.6833	0.6833	0.7278	0.7278	0.7278	
F	10	10	0.0100	0.0100	10	0.0100	0.0100	0.0100	10	1.0434	$\times 10^{-11}$
Group error:	0.0362										

Table C.1: Optimal parameter values for each sham rat

Rat ID (n = 7)								
Parameter	8	10	12	15	27	28	29	
v	0.0380	0.0280	0.0380	0.0220	0.0360	0.0380	0.0300	
S_1	0.0085	0.0085	0.0065	0.0065	0.0085	0.0072	0.0085	
S_2	0.0400	0.0244	0.0400	0.0400	0.0400	0.0333	0.0400	
D_1	0.6833	0.5500	0.7278	0.6389	0.5944	0.8611	0.8167	
λ_1	0.2311	0.2311	2	1.3367	0.2311	2	1.7789	
J_1	2	0	0	0	0	1	0	
F	0.0100	0.0100	0.0100	0.0100	0.0100	10	0.0100	$\times 10^{-11}$
Group error:	0.0363							

Table C.2: Optimal parameter values for each ovx rat

Rat ID (n = 9)										
Parameter	2	5	7	13	19	21	24	25	30	
v	0.0360	0.0380	0.0340	0.0380	0.0380	0.0320	0.0360	0.0280	0.0360	
S_1	0.0067	0.0065	0.0069	0.0072	0.0085	0.0065	0.0065	0.0085	0.0085	
S_2	0.0267	0.0378	0.0200	0.0289	0.0356	0.0244	0.0400	0.0333	0.0244	
S_3	0.0044	0.0022	0.0011	0.0022	0.0022	0.0033	0.0022	0.0022	0.0022	
D_1	0.7278	0.7722	0.6389	0.6389	0.5500	0.5944	0.7278	0.5500	0.8167	
D_2	0.8967	0.9456	0.9700	0.9700	0.8722	0.9700	0.9700	0.9456	0.9700	
λ_1	0.0100	2	2	0.2311	0.2311	2	2	0.2311	0.2311	
λ_2	0.3422	0.3422	0.3422	0.3422	0.3422	0.3422	3	0.3422	0.3422	
η	0.0600	0.1000	0.1600	0.0800	0.0600	0.1200	0.0800	0.0600	0.0400	
J_1	0	2	0	0	0	0	0	0	0	
J_2	18	18	16	18	18	18	18	18	14	
K	14	18	18	18	16	18	18	18	14	
F	0.0100	0.0100	0.0100	0.0100	0.0100	10	10	0.0100	0.0100	$\times 10^{-11}$
Group error:	0.0363									

Table C.3: Optimal parameter values for each ovx+zol rat

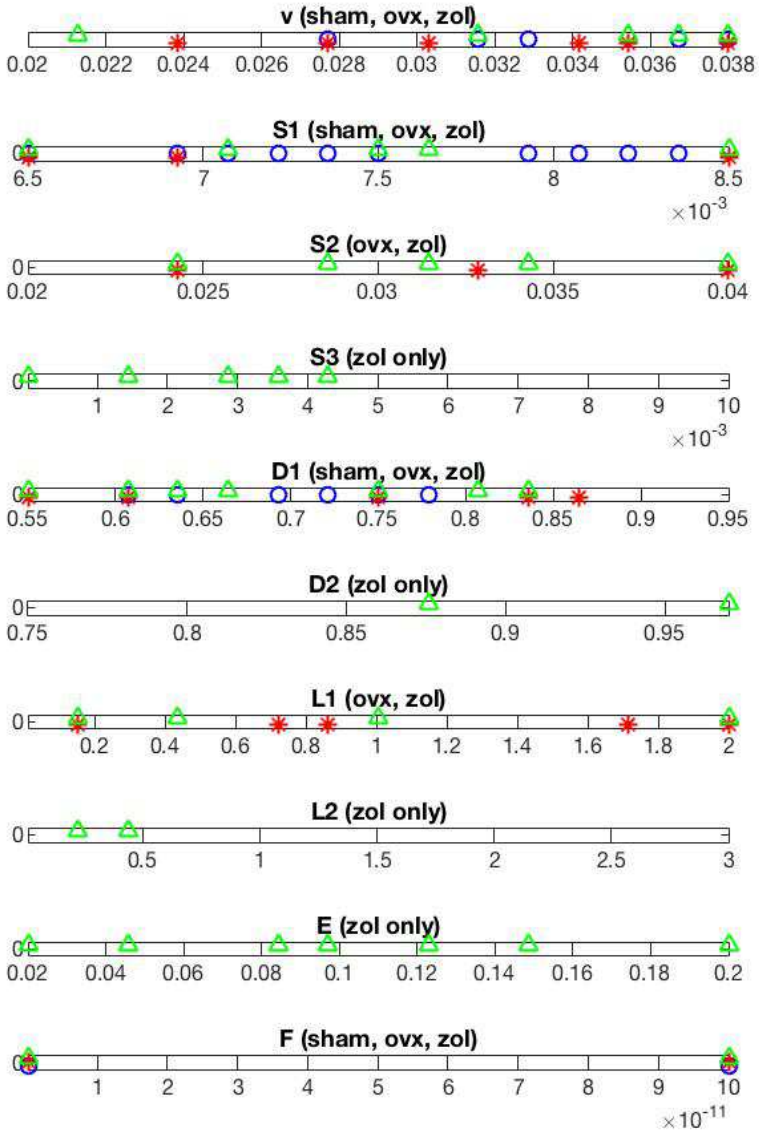

Figure C.4: Distribution of parameter values with initial conditions $s = 0.1$. Parameters are $v, S_1, S_2, S_3, D_1, D_2, \lambda_1, \lambda_2, E, F$ for $s = 0.1$ and $J_1 = 0, J_2 = 14, K = 14$. Colours are according to group. Sham: blue o, ovx: red *, zol: green triangle.